

Silicon Nanoparticle Synthesis and Modeling for Thin Film Solar Cells

by

Zahra Albu

B.Sc., King Faisal University, 2005

A Thesis Submitted in Partial Fulfillment of the
Requirements for the Degree of

MASTER OF APPLIED SCIENCE

in the Department of Electrical and Computer Engineering

© Zahra Albu, 2014

University of Victoria

All rights reserved. This thesis may not be reproduced in whole or in part, by photocopying or other means, without the permission of the author.

Silicon Nanoparticle Synthesis and Modeling for Thin Film Solar Cells

by

Zahra Albu

B.Sc., King Faisal University, 2005

Supervisory Committee

Dr. Chris Papadopoulos, Supervisor
(Department of Electrical and Computer Engineering)

Dr. Tao Lu, Departmental Member
(Department of Electrical and Computer Engineering)

Supervisory Committee

Dr. Chris Papadopoulos, Supervisor
(Department of Electrical and Computer Engineering)

Dr. Tao Lu, Departmental Member
(Department of Electrical and Computer Engineering)

ABSTRACT

Nanometer-scale silicon shows extraordinary electronic and optical properties that are not available for bulk silicon, and many investigations toward applications in optoelectronic devices are being pursued. Silicon nanoparticle films made from solution are a promising candidate for low-cost solar cells. However, controlling the properties of silicon nanoparticles is quite a challenge, in particular shape and size distribution, which effect device performance. At present, none of the solar cells made from silicon nanoparticle films have an efficiency exceeding the efficiency of those based on crystalline silicon. To address the challenge of controlling silicon nanoparticle properties, both theoretical and experimental investigations are needed. In this thesis, we investigate silicon nanoparticle properties via quantum mechanical modeling of silicon nanoparticles and synthesis of silicon nanoparticle films via colloidal grinding.

Silicon nanoparticles with shapes including cubic, rectangular, ellipsoidal and flat disk are modeled using semi-empirical methods and configuration interaction. Their electronic properties with different surface passivation were also studied. The results showed that silicon nanoparticles with hydrogen passivation have higher HOMO-LUMO gaps, and also the HOMO-LUMO gap depends on the size and the shape of the particle. In contrast, silicon nanoparticles with oxygen passivation have a lower HOMO-LUMO gap. Raman spectroscopy calculation of silicon nanoparticles show peak shift and asymmetric broadening similar to what has been observed in experiment.

Silicon nanoparticle synthesis via colloidal grinding was demonstrated as a straightforward and inexpensive approach for thin film solar cells. Data analysis of silicon particles via SEM images demonstrated that colloidal grinding is effective in reducing the Si particle size to sub-micron in a short grinding time. Further increases in grinding time, followed by filtration demonstrated a narrowing of the Si particle size and size-distribution to an average size of 70 nm. Raman spectroscopy and EDS data demonstrated that the Si nanoparticles contain oxygen due to exposure to air during grinding. I - V characterization of the milled Si nanoparticles showed an ohmic behaviour with low current at low biases then Schottky diode behaviour or a symmetric curve at large biases.

Contents

Supervisory Committee	ii
Abstract	iii
Table of Contents	v
List of Abbreviations	vi
List of Tables	viii
List of Figures	ix
Acknowledgements	x
Dedication	xi
1 Introduction	1
1.1 Electronic and Optical Properties of Silicon	2
1.1.1 Recombination Mechanisms	5
1.2 Quantum Confinement	8
1.3 Solar Cells	12
1.3.1 Quantum Efficiency	17
1.3.2 Conversion Efficiency	18
1.4 Solar Cell Technologies	21
1.4.1 Crystalline Solar Cells	21
1.5 Thin Film Technology	22
1.5.1 Crystalline Silicon	23
1.5.2 Amorphous Silicon	23
1.5.3 Copper Indium Diselenide and Related Materials	24
1.5.4 Cadmium Telluride	24

1.6	Third Generation Photovoltaics	25
1.6.1	Tandem Solar Cells	25
1.6.2	Dye Sensitized solar cells	26
1.6.3	Organic Solar Cells	27
1.7	Nanostructured Solar Cells	28
1.7.1	Hot Carriers	29
1.7.2	Intermediate Band Solar Cells	30
1.7.3	Multiexciton Generation	31
1.7.4	Up and Down Conversion	31
1.8	Colloidal Quantum Dot Solar Cells	32
1.9	Thesis Outline and Scope of Research	37
2	Modeling Silicon Nanoparticles	39
2.1	Theory	41
2.2	Semi-empirical Methods	45
2.3	Configuration Interaction Method	45
2.4	Geometry Optimization	47
2.5	Modeling Silicon Quantum Dots	49
2.5.1	Structure Construction	50
2.5.2	Cubic SiNCs	51
2.5.3	Rectangular SiNCs	52
2.5.4	Ellipsoidal SiNCs	54
2.5.5	Flat Disk SiNCs	54
2.5.6	Computational Method	56
2.5.7	VAMP Tests on Benzene	56
2.6	Results and Discussion	59
2.6.1	Geometry Optimization	59
2.6.2	HOMO-LUMO Gap	62
2.6.3	Modeling Different Shapes	63
2.6.4	Raman Spectroscopy	67
2.7	Discussion	67
3	Experimental Results	70
3.1	Introduction	70
3.2	Planetary Ball Milling	71

3.3	Colloidal Grinding	72
3.3.1	Experimental Details	72
3.3.2	Purification	74
3.4	Fabrication of Si Nanoparticle Thin Films	77
3.5	Microscopy	78
3.5.1	Optical Microscopy	79
3.5.2	Scanning Electron Microscopy	79
3.6	Structural Analysis	83
3.6.1	Raman Spectroscopy	83
3.6.2	Energy Dispersive Spectroscopy	87
3.7	Electrical Characterization	89
3.7.1	Short-Time Grinding	90
3.7.2	Long-Time Grinding	91
3.8	Discussion	92
3.9	Conclusion	95
4	Conclusion and Future Work	96
4.1	Summary	96
4.2	Future Work	97
4.2.1	Modeling	98
4.2.2	Experiment	98
	Bibliography	101

List of Abbreviations

Si Silicon

O Oxygen

Au Gold

AM Air Mass

FF Fill Factor

IB Intermediate Band

VB Valence Band

CB Conduction Band

MEG Multiexciton Generation

UC Up-Conversion

DC Down-Conversion

EQE External Quantum Efficiency

IQE External Quantum Efficiency

SD Slater determinant

MO Molecular Orbitals

PSE Potential Energy Surface

LCAO Linear Combination of Atomic Orbitals

HF Hartree Fock

HOMO Highest Occupied Molecular Orbital

LUMO Lowest Unoccupied Molecular Orbital

SCF Self-Consistency Field

AM1 Austin Model 1

PM3 Parameterized Model Number 3

MNDO Modified Neglect of Diatomic Overlap

CI Configuration Interaction

CIS Configuration Interaction Single

CISD Configuration Interaction Single and Double

Gnorm Gradient Norm

NC Nanocrystal

NP Nanoparticle

QC Quantum Confinement

QD Quantum Dot

CQD Colloidal Quantum Dot

SEM Internal Quantum Efficiency

EDS Energy Dispersive Spectroscopy

IPA Isopropyl Alcohol

List of Tables

Table 1.1	Semiconductor material bandgaps at 300K [6].	5
Table 2.1	Cubic SiNCs dimensions.	51
Table 2.2	Difference between rectangular SiNCs in width.	52
Table 2.3	Difference between all ellipsoidal SiNCs in height.	54
Table 2.4	Difference between all flat shapes of SiNCs in diameter.	55
Table 2.5	Experimental and theoretical data of benzene molecule.	57
Table 2.6	Optical absorption bands of benzene from experiment.	58
Table 2.7	Excitation energies of benzene calculated by AM1 and PM3 that correspond to the major absorption bands.	58
Table 2.8	Convergence criteria for $Si_{16}H_{32}$ for various trials.	60
Table 2.9	Convergence criteria for $Si_{32}H_{54}$ for various trial.	60
Table 2.10	Difference between cubic SiNCs and imported structures in bond length.	62
Table 2.11	Electronic properties of SiNCs and imported structures using AM1.	62
Table 2.12	HOMO-LUMO gap of rectangular SiNCs.	63
Table 2.13	HOMO-LUMO gap of ellipsoidal SiNCs.	64
Table 2.14	HOMO-LUMO gap of flat disk SiNCs.	65
Table 2.15	HOMO-LUMO gap of oxidized SiNCs.	65
Table 3.1	Material data and grinding parameters for all prepared trials.	73
Table 3.2	Centrifugation parameters.	75
Table 3.3	Centrifugation results for trial 4 (grinded for 1.5 hours at 500 rpm) and trial 8 (grinded for 1.5 hours at 250 rpm).	76
Table 3.4	Types of substrates used for fabrication of thin films.	78
Table 3.5	Names of the samples and their parameters used for I - V charac- terization	90

List of Figures

Figura 1.1 Silicon diamond lattice unit cell. After [4].	2
Figura 1.2 Semiconductor bandgap. After [7]	3
Figura 1.3 Absorption coefficient of various semiconductor materials versus wavelength. After [6]	5
Figura 1.4 A Simple illustration of the absorption and the major recombination processes in an indirect bandgap material like silicon where the various colored arrows specify the type of transition: the indirect radiative absorption (black arrows) and indirect radiative recombination (red arrows). Both black and red arrows indicate the need of phonon to assist the transition. Auger recombination (green arrow) and free carrier absorption (orange arrow) are also shown. After [9].	6
Figura 1.5 Electron density of states in bulk, 2D film, 1D wire and 0D dot, respectively. After [13].	9
Figura 1.6 The bandgap tuning ability of CdSe by increasing the degree of confinement from quantum well, to quantum wire, and then quantum dot. After[13].	9
Figura 1.7 Shift of the absorption spectra of PbSe QDs by changing the size from 3.3-8.1 nm. (Top right) shows an increase of the confinement effects and the shift in energy level in the first exciton as the size decreases. (Bottom right) shows the size dependent behavior of the lowest energy transition. After [11,22].	11
Figura 1.8 Surface to volume ratio in Ge NPs where 17, 170, 1530, 9955, and 71505 indicate the total number of atoms in every dot. After [19]	11
Figura 1.9 Solar radiation versus wavelength. After[24].	13
Figura 1.10a) p-n junction structure and b) band diagram. a) Adopted from [2] and b) After [27].	14

Figura 1.11	I - V characteristic of an ideal solar cell. After [28].	16
Figura 1.12	PV technology's performance and prices per watt peak according to 2008 market share. After [26].	16
Figura 1.13	Three scenarios of the global PV electricity generation and the relative share of the total worldwide electricity production where: the blue, green, and gray lines represent ETP Blue Map, IEA Roadmap and industry scenarios, respectively. After [26]. . . .	17
Figura 1.14	The upper limits of short circuit current density as a function of the bandgap. After [28].	19
Figura 1.15	The conversion efficiency limit of various solar cell materials as a function of the band gap where the solid lines are for AM0, and AM1.5 and the dash line is for the black body solar cell under AM0. After [28].	20
Figura 1.16	Analysis of the main losses of the solar spectrum in silicon solar cells. After[11].	20
Figura 1.17	Effect of parasitic resistance on I - V characteristic of the illuminated p-n junction. After[23].	21
Figura 1.18	Cross section of a single crystal silicon solar cell. After [31]. . .	22
Figura 1.19	General structure of a thin film solar cell. After [34].	23
Figura 1.20	Structure of a two-junction tandem solar cell. After [39].	26
Figura 1.21	Schematic of a typical configuration of a dye-sensitized solar cell. After[43].	27
Figura 1.22	Schematic diagram of a heterojunction organic solar cell. The arrows show the operation principle. (1) Absorption of the light in the active layer is followed by either (4) decaying the exciton back to HOMO or (2) undergoing separation if it reaches the interface by hopping (3) completing the circuit to produce a current or (5) the exciton recombining back into HOMO after the separation. After [43].	28
Figura 1.23	Maximum conversion efficiency limits for single junction, tandem cells and new concepts based on nanostructures. After [11]. . .	29
Figura 1.24	Band digram of a hot carrier solar cell and how to allow collection of hot carriers before cooling through a selective energy contact. After [48].	30

Figura 1.25	Intermediate band solar cell concept where the red and orange arrows are for electron transition from VB to IB, then from IB to CB, and green and blue arrows are for regular solar cell absorption. After [48].	30
Figura 1.26	Concept of multiexciton generation, when one high-energy photon at least twice E_g , creates two e-h pairs. Adopted from [48].	31
Figura 1.27	Schematic representations of down-conversion and up-conversion. In the down-conversion method a quantum dot layer is placed on top of the solar cell and an up-conversion layer of quantum dots is placed on the bottom. After [50].	32
Figura 1.28	Solution-phase synthesis is a promising route for inexpensive solar cells, where the colloidal quantum dots can be deposited onto a flexible substrate via techniques such as spray painting, reel-to-reel printing and ink-jet printing. After [51].	33
Figura 1.29	(Top) shows scanning electron microscopy (SEM) cross-section of the Schottky solar cell that has the structure of ITO/NC film/metal, and the scale bar is 100nm. (bottom) shows the band diagram of a Schottky cell, where the band bending occurs at the interface between the nanocrystal (NC) film and the electrode. After [56].	34
Figura 1.30	Comparison of I-V characteristics for a heterojunction structure that consists of Au/PbSe QDs/ZnO/ITO/glass with EDT and with EDT and hydrazine treatment. The inset shows an SEM cross-section of the device structure. After [58].	35
Figura 1.31	Schematic diagram of a silicon tandem cell based on two layers of SiQDs with band gaps of 2 and 1.5 eV for the top and second layer, respectively. After [63].	36
Figura 1.32	Motivation and challenges of using Si nanoparticle thin film. . .	37
Figura 2.1	HF as the starting point for other approximations. Adopted from [66].	41
Figura 2.2	Illustration of the procedure in SCF approximation. After [66].	44
Figura 2.3	Possible excited state configurations for generating the final determinant for single, double, triple and quadruple excitation along with HF as reference. After [66].	47

Figura 2.4 Illustration of the potential energy surface for a molecule that has two degrees of freedom. After [67].	48
Figura 2.5 The principle for calculating heat of formation in any SCF semi-empirical program, where the program is encoded with values of heat of formation of atoms and then the atomization energy of the molecule is calculated to obtain the heat of formation of the optimized molecule. After [69].	49
Figura 2.6 Cubic $Si_{216}H_{198}$ a) 3D view of cubic shape, b) top view.	51
Figura 2.7 Illustration of dimensional measurements of cubic SiNCs.	52
Figura 2.8 Rectangular $Si_{120}H_{166}$ a) 3D view of a rectangular shape, b) side view and c) top view.	53
Figura 2.9 Rectangular $Si_{80}(OH)_{120}$ a) 3D view of a rectangular shape, b) side view and c) top view.	53
Figura 2.10 Constructing ellipsoidal SiNCs a) cutting an ellipsoidal by removing the outer Si atoms of the shape b) after hydrogen passivation c) 3D view of $Si_{166}H_{172}$ shape	54
Figura 2.11 Constructing a flat disk a) cutting an ellipsoidal by removing the outer Si atoms of the shape b) after hydrogen passivation c) 3D view of $Si_{186}H_{156}$ shape.	55
Figura 2.12 Benzene molecule, C_6H_6	56
Figura 2.13 Calculated UV-vis spectra of benzene with a) AM1 and b) PM3)	59
Figura 2.14 Cubic $Si_{32}H_{54}$ a) constructed shape and b) optimized.	61
Figura 2.15 Cubic $Si_{64}H_{84}$ a) constructed shape b) after optimization	61
Figura 2.16 $Si_{35}H_{36}$ with average diameter of 1.704 nm a) before and b) after optimization [74].	62
Figura 2.17 Size dependent HOMO-LUMO gaps for all cubic, rectangular, ellipsoidal, and flat disk SiNCs modelled for this work.	66
Figura 2.18 Energy levels of SiNCs of different shapes.	66
Figura 2.19 Modeled Raman spectra of cubic $Si_{64}H_{84}$ with AM1 single energy calculation.	67
Figura 2.20 Modeled Raman spectra of cubic $Si_{216}H_{84}$ with an AM1 single energy calculation.	68
Figura 3.1 a) Planetary ball mill RETSCH PM200 and b) Motion of grinding spheres inside the vial. After [98].	72

Figura 3.2 Milling conditions, reproduced from ref [101].	73
Figura 3.3 Extraction process of colloidal particles	74
Figura 3.4 Silicon colloidal suspensions after centrifugation for (12 minutes at 3000 rpm, 55 minutes at 7000 rpm, 26 minutes at 10000 rpm, 100 minutes at 10000 rpm) left to right for both figures	77
Figura 3.5 Deposition process of Si nanoparticle film by drop-coating and layer by layer deposition using a mechanical pipette a) during deposition, b) after deposition, and type of substrates are: c) deposition on a interdigitated gold electrode array substrate, d) glass substrate and e) Si/Au/Al/Co wafer substrate.	78
Figura 3.6 Optical images of silicon particles films on glass substrate after centrifugation for 3000 rpm at 12 min a) Trial 11: grinded at (500 rpm & 3h) and b) Trial 9 : grinded at (400 rpm & 15h)	79
Figura 3.7 SEM images of silicon particles films on glass substrate after grinding a)milled for 1 hour at 300 rpm and b)milled for 3 hours at 500 rpm.	80
Figura 3.8 SEM images of Si particle films after centrifugation for a) 12 minutes at 3000 rpm (Trial 8) b) 12 minutes at 3000 rpm (Trial 11) and c) 55 minutes at 7000 rpm (Trial 10).	81
Figura 3.9 SEM image of silicon particles (grinded for 15 hours at 400 rpm) centrifuged for 12 minutes at 3000 rpm. The inset indicates the resulting particle size distribution.	81
Figura 3.10 SEM images of silicon particles (grinded for 15 hours at 400 rpm) centrifuged for 99 minutes at 10000 rpm. The inset indicates the resulting particle size distribution.	82
Figura 3.11 Average particle sizes versus grinding time at grinding speed of 1) 250 rpm, 2) 500 rpm and 3) 400 rpm. All centrifuged for 12 minutes at 3000 rpm.	82
Figura 3.12 Energy level diagram showing three types of interaction of light with matter.	83
Figura 3.13 a) Renishaw Raman microscope (InVia) b) A simple digram of the components of a Renishaw Raman system. After [108].	85
Figura 3.14 Raman spectra of Si particle films on a glass slide substrate a) trial 9, b) trial 10, c) trial 11, d) trial 4. All were centrifuged for 12 minutes at 3000 rpm and e) c-Si.	86

Figura 3.15 Raman spectra of Si particle films on a glass slide substrate for a) trial 11, and b) trial 9 centrifuged both centrifuged for 12 minutes at 3000 rpm and c) c-Si.	87
Figura 3.16 EDS spectroscopy mapping images of Si particle film.	88
Figura 3.17 EDS spectrum of Si particle film on glass slide substrate.	89
Figura 3.18 a) Top view schematic of interdigitated electrodes without any particle film and b) a cross-section of the electrodes after deposition.	90
Figura 3.19 <i>I-V</i> characteristic of Au/Si particle film/Au annealed for 90 minutes at 250 °C in argon, samples A. The inset shows a magnified optical image of one electrode in the interdigitated gold substrate.	91
Figura 3.20 <i>I-V</i> characteristic of Si particle films annealed for 1 hour at 70 °C in air (sample D) for two successive measurements. The inset shows an optical image of Si particle film on an interdigitated substrate.	92
Figura 3.21 <i>I-V</i> characteristic of Si particle films annealed for 1 hour at 70 °C in air (sample D) for three successive measurements. The inset shows an optical image of Si particle film on interdigitated substrate.	93
Figura 3.22 <i>I-V</i> characteristic of Au/Si particle film/Au annealed for 1 hour at 70 °C in air (sample D). The inset shows an optical image of Si particle film on an interdigitated substrate.	94
Figura 4.1 Heterojunction solar cell based on colloidal Si particle film. a) quantum dot junction, b) bulk heterojunction, c) heterojunction blend.	100

ACKNOWLEDGEMENTS

I would like to express my gratitude to all the people who have given me support and guidance during my studies in Canada and to those people who have give me motivation and support to finish my degree. First of all, to my supervisor Dr. Chris Papadopoulos for his assistance. Second, I am very thankful to the Saudi Government for funding my studies through the King Abdullah Scholarship. Without this scholarship, coming to Canada would have been impossible. Also, I would like to express my thanks to all my fellow researchers, especially, Xiwen Gong with whom I worked closely, and Dryden Tamura. Additionally, I would like to show my appreciation to my colleagues Kenza, Mostafa, Alireza, Suma, Mahbubeh, and my friend Safa, for their continuous enthusiasm, support, and help. Finally, I would like to thank my brother Qasem and his wife Tuqa, my sister Sarah for their love and caring. All the best to my parents and siblings in Saudi Arabia, and the friends I have made in Canada.

DEDICATION

To all of those, near and far, who have prayed and asked Allah to protect me.

Chapter 1

Introduction

Silicon has a long history of success in both microelectronic and photovoltaic industries [1]. This success is due to the planar processing technology that has been successfully used for making integrated circuits (ICs) based on field effect transistors (FET). Silicon exists in various types depending on growth conditions e.g., temperature [1,2]. These types of silicon are classified as crystalline or amorphous, according to the degree of periodicity [1,2]. Crystalline silicon exists in two forms: monocrystalline and polycrystalline. Monocrystalline silicon has superior electronic and optical properties over polycrystalline. The superiority of monocrystalline is related to the high degree of regularity and the periodicity of silicon atoms in space. On the other hand, polycrystalline silicon has grains that are irregularly bonded at regions called grain boundaries, which reduce its electronic and optical properties. Monocrystalline silicon is more expensive than polycrystalline due to the slow manufacturing process. The other type of silicon is amorphous, which is the lowest quality form of silicon. The low quality is due to the random arrangement of the silicon atoms and the existence of dangling bonds. However, saturating the dangling bonds of amorphous silicon with hydrogen enhances its performance [2]. All three forms of silicon are found in the photovoltaics (PV) industry. However, all crystalline silicon forms dominate the PV market even though the use of these materials is considered costly, in particularly the single crystal.

1.1 Electronic and Optical Properties of Silicon

Silicon is a group IV element in the periodic table that has an electronic configuration of $1s^2 2s^2 2p^6 3s^2 3p^2$. This electronic configuration shows that silicon has four valence electrons, which can be shared with neighboring atoms to form covalent bonds through sp^3 hybridization. Crystalline silicon is based on a diamond lattice structure[3]. The diamond lattice of silicon is formed by combining two face centred cubic (fcc) lattices in which the second cubic is displaced by one-fourth along the direction of (111) the first cubic as shown in Figure 1.1. The lattice constant of the silicon unit cell has the value of 0.543 nm [1].

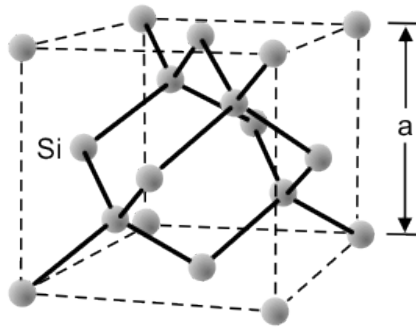


Figure 1.1: Silicon diamond lattice unit cell. After [4].

Crystalline Si is a semiconductor with a bandgap of about 1.12 eV between the valence and conduction bands. For pure silicon, the intrinsic carrier concentration is about $1 \times 10^{10} \text{ cm}^{-3}$ at room temperature. The intrinsic carrier concentration can be changed via doping the semiconductor with impurities [1, 5]. Doping with impurities can be introduced by adding atoms from a different group of the periodic table to increase the electron and hole concentrations. To change the concentration of electrons in pure silicon, an element from group V is often used e.g., phosphorous [1, 5]. Phosphorous has five valence electrons while silicon has four electrons. This means that replacing one silicon atom with a phosphorous atom leaves one electron unbounded, which is easily ionized even at room temperature. To increase the hole concentration, a silicon atom is replaced by an atom from group III of the periodic table e.g., boron[1, 5]. Boron has three valence electrons that bonded to the silicon atom leaving an unbounded electron from the silicon atom which can be easily ionized to the impurity level leaving behind a hole. Dopants which donate an electron to the conduction band are called donors, whereas the dopant atoms are called acceptors

when they accept the electron from the valence band. Semiconductors with an excess of electrons are n-type, and with an excess of holes are called p-type. Apart from doping, absorption of light can also increase the carrier concentration by generating an extra electron-hole (e-h) pair. Absorption of light depends on the band structure of the semiconductor. In particular, absorption depends on the nature of the bandgap of the semiconductor, i.e., whether it is direct or indirect [6]. For direct bandgap material, the maximum of the valence band and the minimum of the conduction band occur at the same value of wave vector k in the reciprocal space. In contrast, in an indirect band gap semiconductor, the maximum of the valence and the minimum of the conduction band are not aligned (Figure 1.2a and Figure 1.2b).

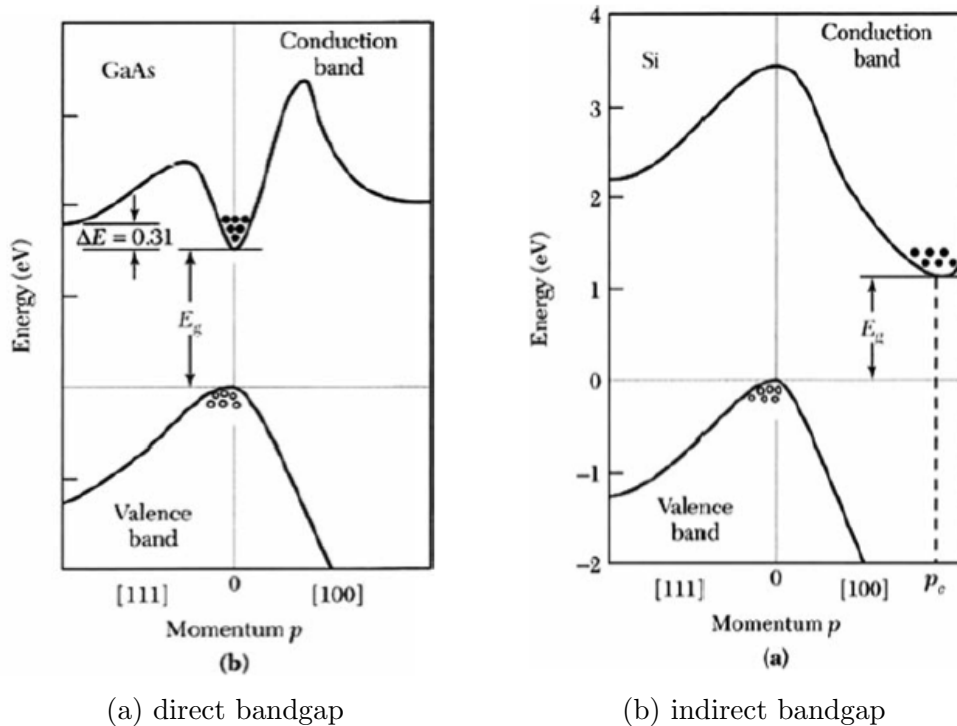


Figure 1.2: Semiconductor bandgap. After [7]

The nature of the band structure is important in determining the probability of radiative transitions. For any transition to occur both energy and momentum conservation must be satisfied, which can be easily met in direct bandgap semiconductors. However, in an indirect bandgap semiconductor, the conservation of momentum cannot be met without a third particle, a phonon, which is needed to assist the transition. Therefore, the absorption of a photon in an indirect band gap semiconductor is rela-

tively weak compared to than that of direct bandgap semiconductor. When a photon is incident on semiconductor, it may or may not be absorbed depending on the λ_c , which is the critical wavelength that determines the wavelength of absorption.

$$\lambda_c = \frac{hc}{E_g} \quad (1.1)$$

Any photon that has a longer wavelength than λ_c , is not strongly absorbed. In contrast, any photon with a shorter wavelength than λ_c is strongly absorbed. The penetration depth of a light incident on a material depends on its absorption coefficient. The absorption coefficient determines the length scale at which the absorption of photons can occur according to Lambert-Beers law (Eq.1.2).

$$I = I_0 \exp(-\alpha x) \quad (1.2)$$

where: I_0 is the intensity of the incident light before penetrating into the semiconductor, I the is intensity of light after the attenuation, α is the absorption coefficient and x is the thickness of the material. Figure 1.3 shows the strong dependence of the absorption on the band structure of the semiconductor and the wavelength of the incident photon, and Table 1.1 shows the corresponding values of the bandgaps and their types[6]. Figure 1.3 shows that the absorption coefficient of silicon has two major absorption bands. The first absorption band is the direct absorption at wavelength below $0.4 \mu\text{m}$ [6]. The second band is the indirect absorption where the absorption occurs at wavelengths between $0.4 \mu\text{m}$ - $1.1 \mu\text{m}$. For long wavelengths below $0.4 \mu\text{m}$, the absorption coefficient is relatively low. Therefore, a thicker material is needed to absorb long wavelengths, which increases the cost of silicon solar cells.

Table 1.1: Semiconductor material bandgaps at 300K [6].

Semiconductor	Bandgap (eV)	Type
Si	1.12	indirect
Ge	0.67	indirect
GaAs	1.42	direct
InP	1.35	direct
6H-SiC	3.03	indirect
$\text{In}_{0.53}\text{Ga}_{0.47}\text{As}$	0.75	direct

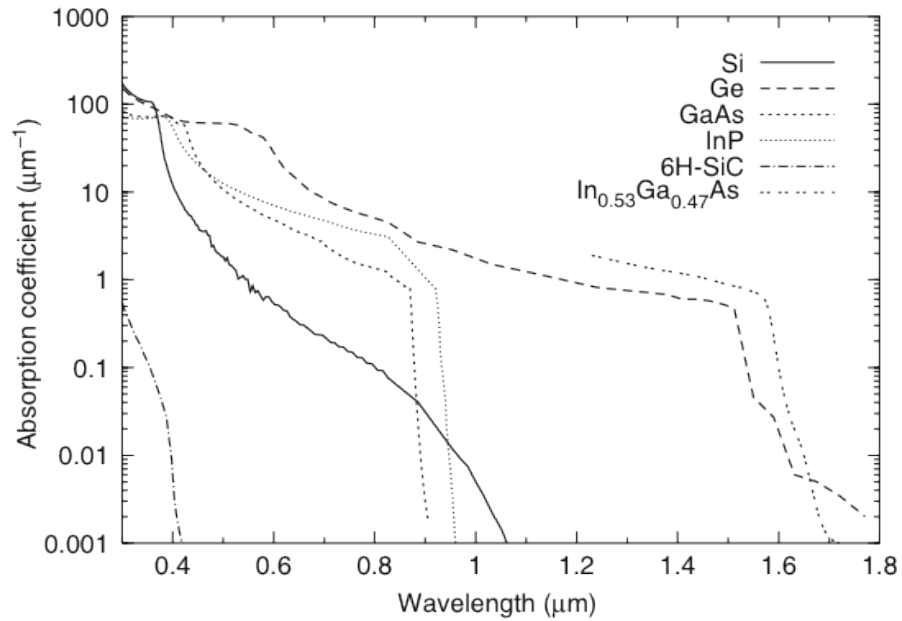


Figure 1.3: Absorption coefficient of various semiconductor materials versus wavelength. After [6]

1.1.1 Recombination Mechanisms

When a semiconductor material is illuminated by light, an e-h pairs are generated as result of absorption. The generated carriers tend back to their equilibrium in a process called recombination. Three types of recombination process are usually possible: radiative recombination, non-radiative recombination through traps, and Auger recombination, (see Figure 1.4)[8,9]. Radiative recombination is the inverse of the absorption process where an excited electron combines with a hole, emitting a

photon. Such a radiative recombination process is much more efficient in direct band gap materials than indirect ones. In contrast, in indirect bandgap materials such as silicon, a third particle is involved in the transition which makes the probability of radiative recombination low. The total radiative recombination rate R_R is given by [8].

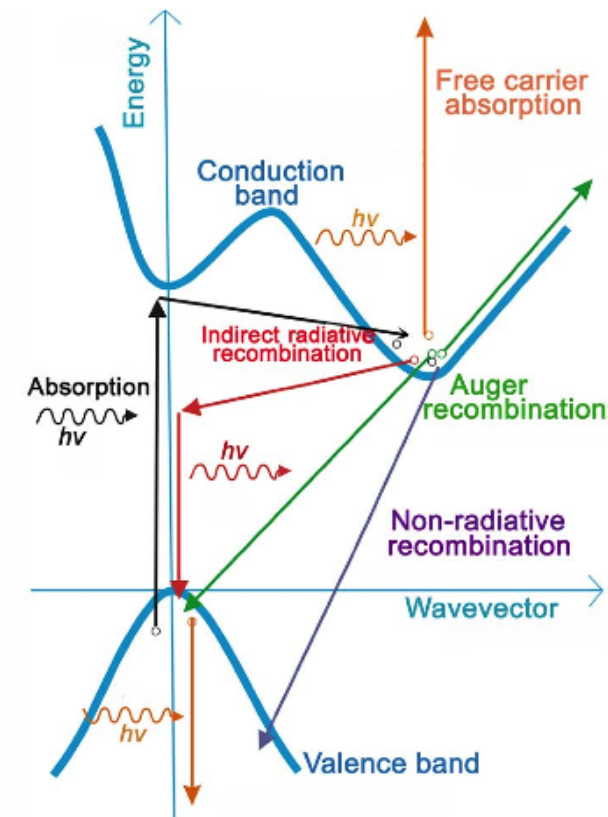


Figure 1.4: A Simple illustration of the absorption and the major recombination processes in an indirect bandgap material like silicon where the various colored arrows specify the type of transition: the indirect radiative absorption (black arrows) and indirect radiative recombination (red arrows). Both black and red arrows indicate the need of phonon to assist the transition. Auger recombination (green arrow) and free carrier absorption (orange arrow) are also shown. After [9].

$$R_R = Bnp \quad (1.3)$$

where B is a constant which can be estimated from the absorption coefficient

for a given semiconductor. n and p are the concentrations of electrons and holes, respectively.

(Eq 1.3) shows that the total recombination rate is restricted by the available number of occupied and empty states in the valence and conduction band of electrons and holes, respectively. The net recombination rate is given by [8],

$$U_R = B(np - n_i^2) \quad (1.4)$$

where n_i is the intrinsic carrier concentration.

For such a radiative recombination process, there is time which determines the rate of recombination called the radiative recombination lifetime. This lifetime can be calculated using the following formula for electrons and holes respectively:

$$\tau = \frac{\Delta n}{U_R} \quad (1.5)$$

$$\tau = \frac{\Delta p}{U_R} \quad (1.6)$$

where: Δn and Δp are the changes in carrier concentrations from the equilibrium values of electrons and holes, respectively.

Another recombination process that involves electrons and holes is the Auger recombination. The Auger recombination is a non-radiative recombination where the energy of the combined electron and hole is given to another electron and hole in either the conduction band or the valence band. Then the second electron releases its excess energy via phonon emission. As in radiative recombination, the Auger process has a lifetime which is determined by the Auger recombination lifetime for electrons and holes [8]:

$$\frac{1}{\tau} = Cnp + Dn^2 \quad (1.7)$$

$$\frac{1}{\tau} = Cnp + Dp^2 \quad (1.8)$$

The Auger recombination is dependent on the dopant concentration. For heavily

doped material, the Auger recombination is more significant than in low or moderate doping.

The other nonradiative recombination is the recombination through defect states. Impurities and defects create allowed energy states, called trap states, within the forbidden bandgap. These trap states serve as effective recombination centres for the carriers. When an electron relaxes back into the valence band, the trap captures the electron and then the electron relaxes from the trap state to the valence band annihilating a hole. This recombination mechanism is the dominant in elemental semiconductors like Silicon and Germanium.

1.2 Quantum Confinement

The electronic and optical properties of a bulk crystal are independent of its dimensions. However, as the dimensions of a material scale down, they start playing a role in determining its properties [10]. The dependence of properties on the dimension is due to the confinement of the motion of the charge carriers in one, two, or three dimensions compared to the counterpart bulk crystal. According to the degree of confinement, these structures are referred to as two-dimensional (2D) quantum well, one dimensional (1D) quantum wire, and zero dimensional (0D) quantum dots, respectively. As illustrated in Figure 1.5, the confinement changes the properties of the confined material, and these changes result from phenomena known as quantum confinement effects (QCEs). The observation of QCEs at room temperature is related to two important lengths [11]. The first is the de Broglie wavelength of electrons and holes of a semiconductor. When the dimension of the confined structure approaches the de Broglie wavelength of the bulk, QCEs can be readily observed. For most semiconductors, the de Broglie wavelength is approximately 10-100 nm. For example, Si and PbSe have wavelengths of about 24 nm and 40 nm, respectively [11]. The second important length is the exciton Bohr radius, which determines the separation between an electron and hole in bulk. The electrostatic interaction between the electron and hole results in an exciton. In the bulk, the attraction between the electron and the hole is weak, and its binding energy is relatively low in the range of kT . Thus, the observation of excitons at room temperature in bulk is difficult. However, when the dimension of a structure is below the bulk exciton Bohr radius, the interaction increases and the observation of excitons in low dimensional systems at room

temperature possible. The exciton Bohr radius can be calculated from the formula [12]:

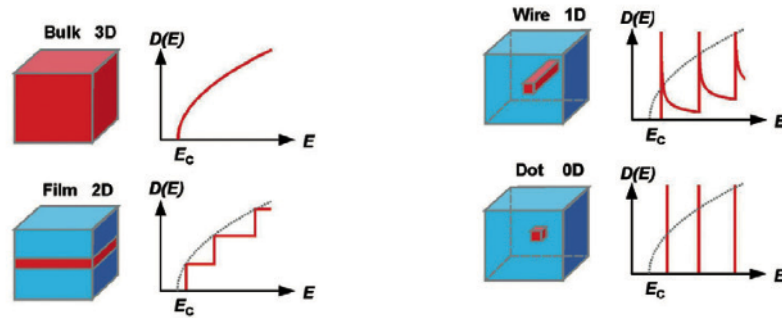


Figure 1.5: Electron density of states in bulk, 2D film, 1D wire and 0D dot, respectively. After [13].

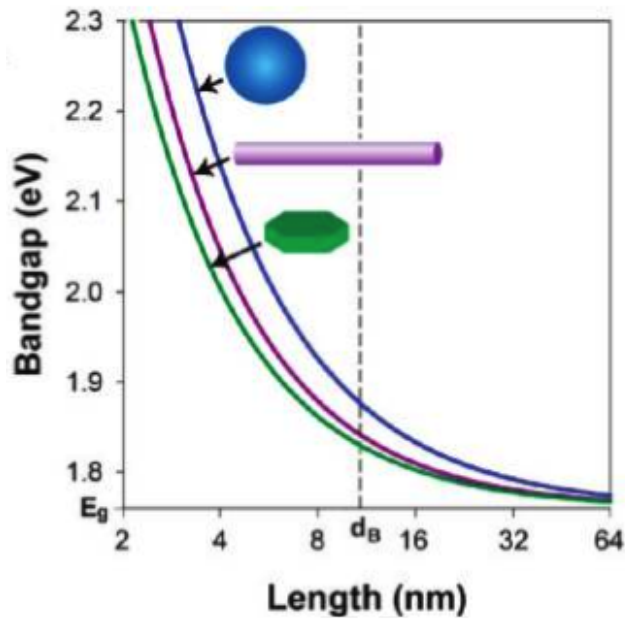


Figure 1.6: The bandgap tuning ability of CdSe by increasing the degree of confinement from quantum well, to quantum wire, and then quantum dot. After[13].

$$a_B = \frac{4\pi\epsilon\hbar^2}{\mu e^2} \quad (1.9)$$

where ϵ is the dielectric constant of a semiconductor, \hbar is Plancks constant, μ is the reduced mass of electron and hole, and e is the charge of electron. Where the

reduced mass is:

$$\mu = \frac{1}{\frac{1}{m_e} + \frac{1}{m_h}} \quad (1.10)$$

For most semiconductors, the Bohr radius ranges from (2-100) nm [11]. For example, Si and PbSe have exciton radius of 4 nm and 47 nm, respectively [11]. One consequence of QCEs is the drastic change of the behaviour of the density of states (DOS) as the size of the material is reduced compare to the bulk. The continuous behaviour of the DOS changes to a discrete energy level (see Figure 1.5). This allows for wide-range tunability of the bandgap by increasing the degree of confinement [25] (Figure 1.6) and, thus, the separation of the top valence band from the conduction band. The phenomena of size dependent bandgap allows researchers to engineer the bandgap and its optical properties to serve various proposes and applications just by changing a material's size and shape. For example, PbSe QDs have shown size-dependent bandgaps for dot sizes of 3.3-8.1 nm, shifting maximum absorption from low energy to high (blue shift) as the size of PbSe QDs decreases (see Figure 1.7)[11].

In bulk, the number of surface atoms is not that significant compared to the overall number of atoms [14]. In contrast, in small size particles that are less than 1 μm , the number of surface atoms is significantly increased. This increase of surface atoms can be estimated from the surface-to-volume ratio [15]. Figure 1.8 illustrates the concept of surface-to-volume ratio for Ge NPs (assuming diamond lattice) [15]. Surface atoms usually terminate to reduce dangling bonds, which enhance the nonradiative recombination [16]. Solution synthesis methods for nanocrystals usually terminate with ligand molecules to stabilize the colloidal quantum dots (CQDs) and prevent aggregation[17, 18]. Epitaxial methods for nanocrystal fabrication is usually embedded on an oxide matrix [19]. A lot of theoretical and experimental investigations have been performed to understand the interplay of QC and surface chemistry [20, 21]. Some spectroscopy measurements show differences in the optical absorption and photoluminescence (PL) peaks even though the size distribution was similar. The differences maybe because of the different ligand treatments [17, 18].

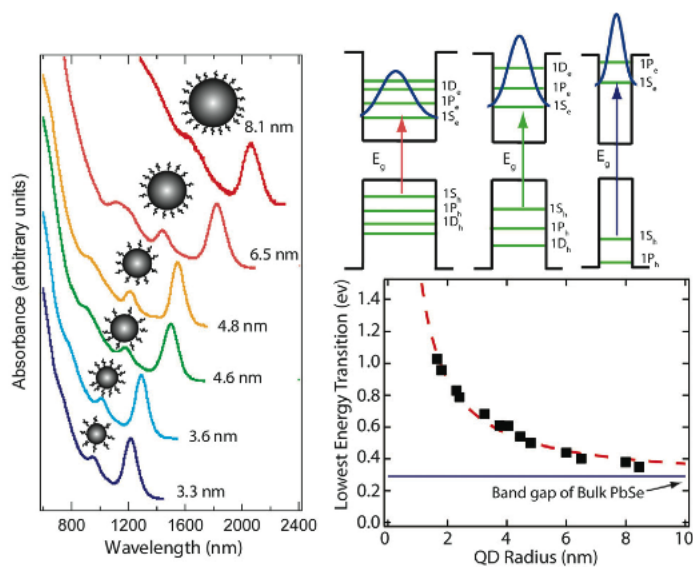


Figure 1.7: Shift of the absorption spectra of PbSe QDs by changing the size from 3.3-8.1 nm. (Top right) shows an increase of the confinement effects and the shift in energy level in the first exciton as the size decreases. (Bottom right) shows the size dependent behavior of the lowest energy transition. After [11, 22].

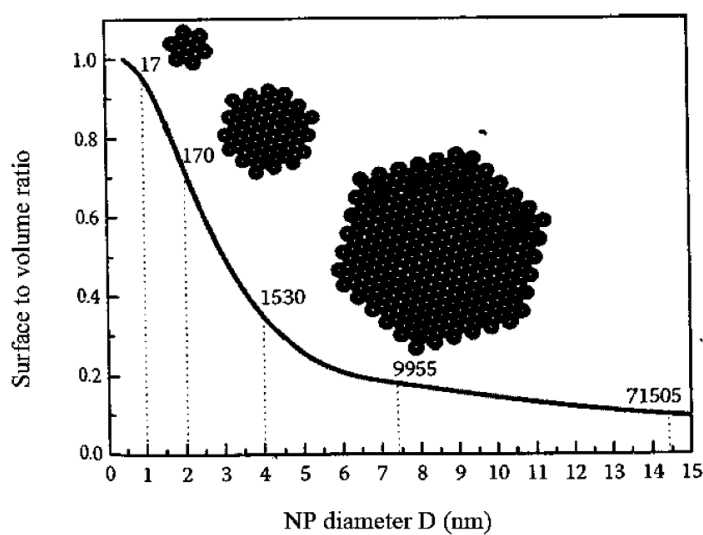


Figure 1.8: Surface to volume ratio in Ge NPs where 17, 170, 1530, 9955, and 71505 indicate the total number of atoms in every dot. After [19]

1.3 Solar Cells

The solar energy emitted by the sun is an immense source of power, which is emitted as electromagnetic radiation of about 1367 W/m^2 reach the earth. However, due to absorption and scattering processes after entering the earth's atmosphere, the power density attenuates. Figure 1.9 shows the areas where the absorption of solar radiation takes place. For example, some ultraviolet wavelengths are absorbed by ozone molecules, while some of the visible and infrared wavelengths are absorbed by water vapour and carbon dioxide. The absorption and scattering effects depend on the optical path length that light travels occurs when entering the earth's atmosphere known as air mass (AM) [23]. The shortest distance the solar radiation travels when the sun position is overhead, is known as AM1. When the sun emits its radiation at an angle relative to the normal, the air mass is found from: $AM = \frac{1}{\cos\theta}$. Even with the attenuation, this power can still be used and converted into other sources of energy, e.g., electricity.

The solar radiation of the sun can be converted into electricity via the photovoltaic effect (PV), which was discovered by Edmond Becquerel in 1839 [24]. In 1954, the first commercial silicon solar cell was made at Bell Laboratories [24]. PV cells are made from semiconductor materials that can absorb sunlight radiation and then conduct electrical current. For large scale production, PV cells are connected together to form a module, and the modules are connected to form PV systems. The produced energy from PV system has many advantages over other renewable energies [25]: PV systems produce very clean energy, since no pollution of the environment occurs during power generation. Also, the power output of a PV system is sustainable because it relies on the sun's power. Additionally, PV systems can provide the energy needed everywhere, even in remote areas where it is impossible to connect to a grid e.g. as standalone PV systems. PV modules also can be integrated into rooftops or building facades. PV systems have already been installed in different locations around the world, e.g., Germany, US, and Japan. The total PV capacity in these countries has reached almost 12GW [26].

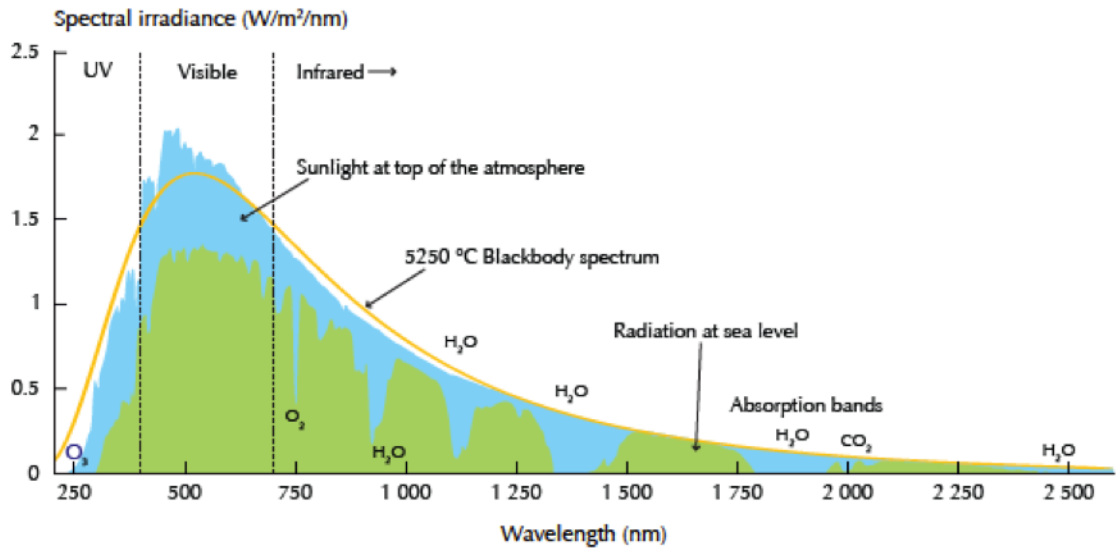


Figure 1.9: Solar radiation versus wavelength. After[24].

Principle of Photovoltaic Solar Cells

A standard PV solar cell is based on a p-n junction. To create a p-n junction from a silicon wafer, usually boron dopants are added to create a p-type region on one side, and phosphorus dopants are added to create an n-type region on the other. A p-n junction is characterized by a built-in electric field due to the diffusion of carriers from one side to the other in order to achieve thermal equilibrium. The built-in field is due to the fixed dopant ions in the space-charge or depletion layers that exist at the interface between n- and p-type regions. When the p-n junction is illuminated, the incident photon can be absorbed or reflected. The absorption and reflection depend on the photon's energy. Figure 1.10 shows the behaviour of incident light entering the solar cell. The absorption can take place in any area inside the cell depending on the energy of the incident photon. When the incident photon is absorbed, e-h pairs are generated. The generated e-h pairs separate due to the built-in field at the junction and finally collect at the contacts. The collected current or I - V characteristic of an ideal solar cell is described by the Shockley equation:

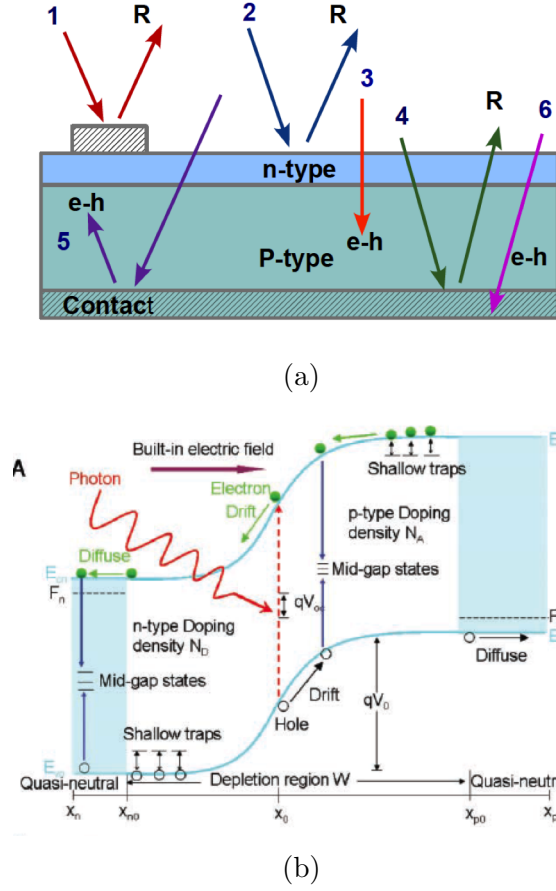


Figure 1.10: a) p-n junction structure and b) band diagram. a) Adopted from [2] and b) After [27].

(also known as the ideal diode equation)

$$I = I_0 \left[\exp \left(\frac{qV}{k_B T} \right) - 1 \right] - I_L \quad (1.11)$$

Where: k_B is the Boltzmann constant, T is the temperature, q is the electron charge, V is the applied voltage, I_0 is the saturation current and I_L is the light-generated current. The saturation current can be calculated from the following formula:

$$I_0 = A \left(\frac{qD_e n_i^2}{L_e N_A} + \frac{qD_h n_i^2}{L_h N_D} \right) \quad (1.12)$$

And the light-generated current can found from the following:

$$I_L = qAG(L_e + W + L_h) \quad (1.13)$$

where A is the cross-sectional area, and D_e and D_h are the diffusion coefficients for electrons and holes, respectively. L_e and L_h are the diffusion length of electrons and holes, respectively. N_A and N_D are the donor and acceptor concentrations, respectively. W is depletion width, and G is generation rate.

The I - V characteristic of such an ideal diode is represented by an offset curve (see Figure 1.11) and three essential parameters are: the short circuit current (I_{sc}), open voltage (V_{oc}), and fill factor (FF). The values of I_{sc} and V_{oc} are determined by:

$$I_{sc} = I_L \quad (1.14)$$

$$V_{oc} = \frac{k_B T}{q} \ln \left(\frac{I_L}{I_0} + 1 \right) \quad (1.15)$$

As shown in (Eq 1.15), the value of V_{oc} depends strongly on I_0 , which means V_{oc} depends on the properties of the semiconductor. Moreover, the FF which is an important parameter in determining the cell performance is the ratio of the maximum power to $V_{oc}I_{sc}$ (Eq 1.16):

$$FF = \frac{V_{mp}I_{mp}}{V_{oc}I_{sc}} \quad (1.16)$$

The power conversion efficiency (PCE) of a solar cell is the ratio of output power to the input power, which is given by the formula:

$$\eta = \frac{V_{oc}I_{sc}FF}{P_{in}} \quad (1.17)$$

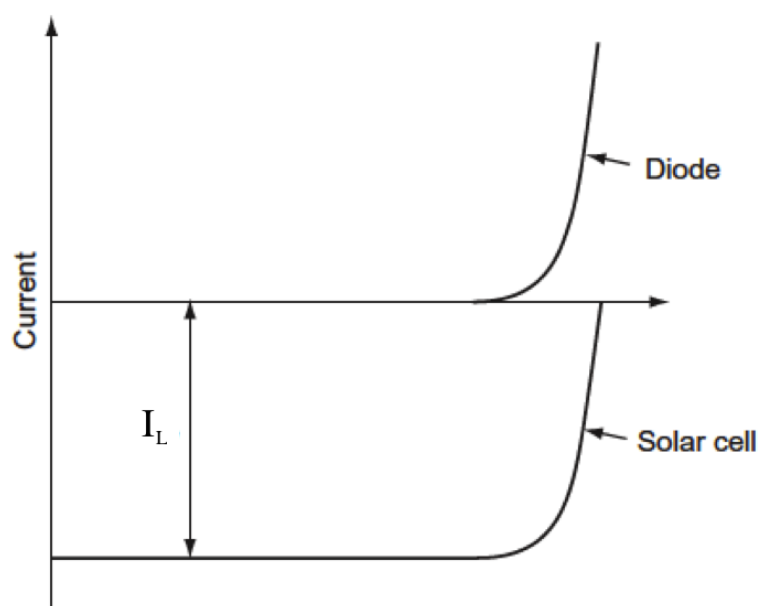


Figure 1.11: I - V characteristic of an ideal solar cell. After [28].

Market Trend and Future Prospective

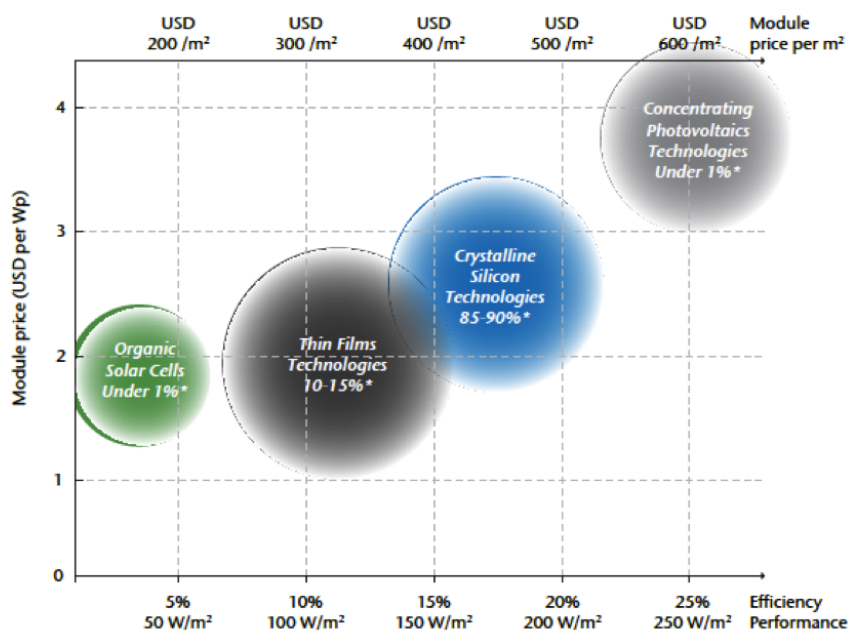


Figure 1.12: PV technology's performance and prices per watt peak according to 2008 market share. After [26].

Low cost PV modules typically have low efficiency while expensive PV modules have high efficiency. Figure 1.12 shows the prices/efficiencies of all PV technologies. Several scenarios have been predicted for climate change by 2050 [26]. Figure 1.13 shows the forecast according to the International Energy Agency (IEA) Roadmap, Energy Technology Perspectives (ETP) Blue Map, and industry scenarios. Each scenario has adopted a different expectation of the total global PV electricity production by 2050. Roadmap expectations have been justified based on two factors. The first one is the increase of PV market growth. The other factor is the drop off of prices by almost 50%. If the market growth, price reduction and global adaption of PV installation continues, then the goal of 11% of the total global electricity market share may be achieved by 2050.

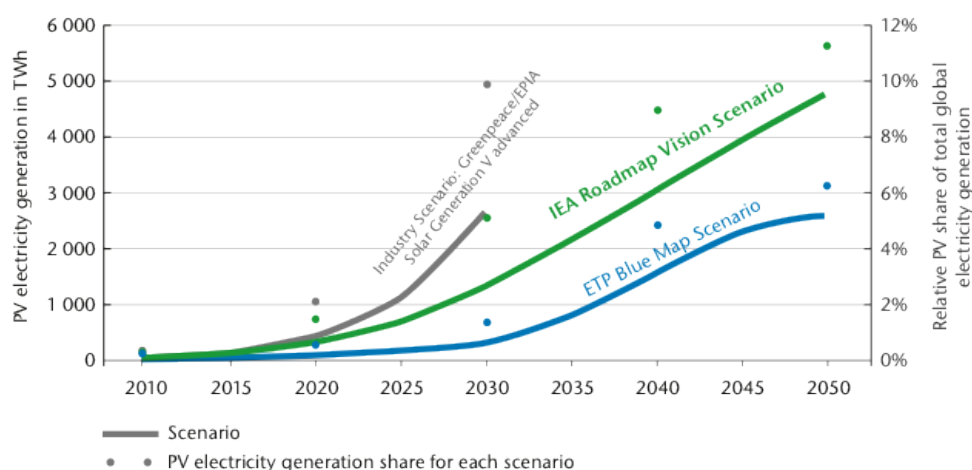


Figure 1.13: Three scenarios of the global PV electricity generation and the relative share of the total worldwide electricity production where: the blue, green, and gray lines represent ETP Blue Map, IEA Roadmap and industry scenarios, respectively. After [26].

Solar cell performance is usually determined by two kinds of efficiencies: quantum efficiency and conversion efficiency.

1.3.1 Quantum Efficiency

Two types of quantum efficiencies are measured to determine the performance of a solar cell: external quantum efficiency (EQE) and internal quantum efficiency (IQE). EQE is the ratio of the collected charge carriers to the number of photons incident on the solar cell:

$$EQE = \frac{\text{Number of collected charge carriers}}{\text{Number of incident photons on the cell}} \quad (1.18)$$

And for IQE, the formula is:

$$IQE = \frac{EQE}{1 - R - A} \quad (1.19)$$

where R and A are the reflection and transmission, respectively.

1.3.2 Conversion Efficiency

For I_{sc} , the upper limit can be calculated if the photon flux is known. Then I_{sc} is found by integrating the photon flux over all the wavelengths absorbed by the material.

$$I_{sc} = qA \int \phi_{ph}(\lambda) d\lambda \quad (1.20)$$

The estimation of the upper limit of I_{sc} is seen in Figure 1.14 to be a function of the bandgap. As the bandgap decreases, the value of I_{sc} increases as well. In contrast, from (Eq 1.15) the maximum value of V_{oc} shows opposite trend to I_{sc} , V_{oc} decreases as the band gap decreases since I_{sc} increases. The limit on the efficiency was calculated theoretically in 1961 by Shockley-Queisser [11]. They calculated the efficiency for an ideal single p-n junction under AM1.5 radiation at 25 °C. The maximum efficiency limit was in the range of 31%- 33% ; see Figure 1.23. Figure 1.23 shows the maximum conversion efficiency occurs for material with a band gap of 1.4-1.6 eV.

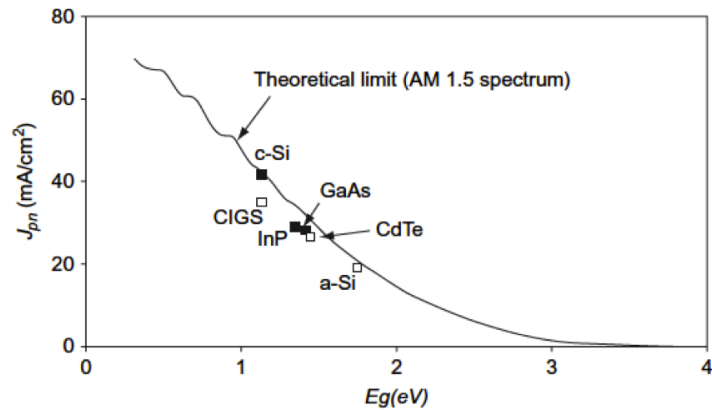


Figure 1.14: The upper limits of short circuit current density as a function of the bandgap. After [28].

For the best laboratory crystalline silicon cell recorded, the measured efficiency was about 25% for silicon, but the efficiency of GaAs was 28.3% slightly higher under AM1.5 at 25 °C [29]. Figure 1.16 shows the analysis of main losses in silicon solar cells along with the available solar spectrum as predicted by Shockley-Queisser [11]. The analysis in Figure 1.16 shows that the thermalization (photon energy greater than E_g) is responsible for losing about 33% of the photon energy. The other loss mechanism is related to unabsorbed photons, and extraction losses reduce the efficiency by 19% and 15%, respectively.

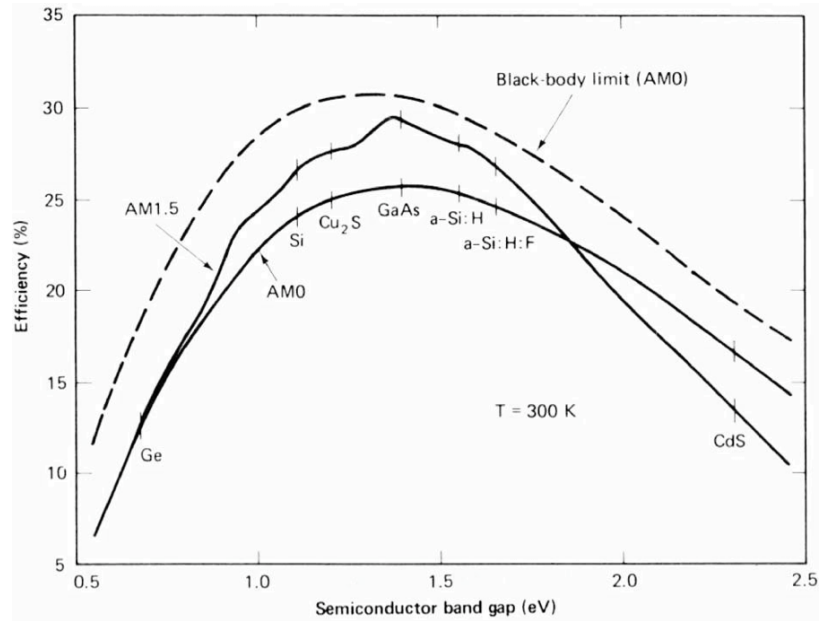


Figure 1.15: The conversion efficiency limit of various solar cell materials as a function of the band gap where the solid lines are for AM0, and AM1.5 and the dash line is for the black body solar cell under AM0. After [28].

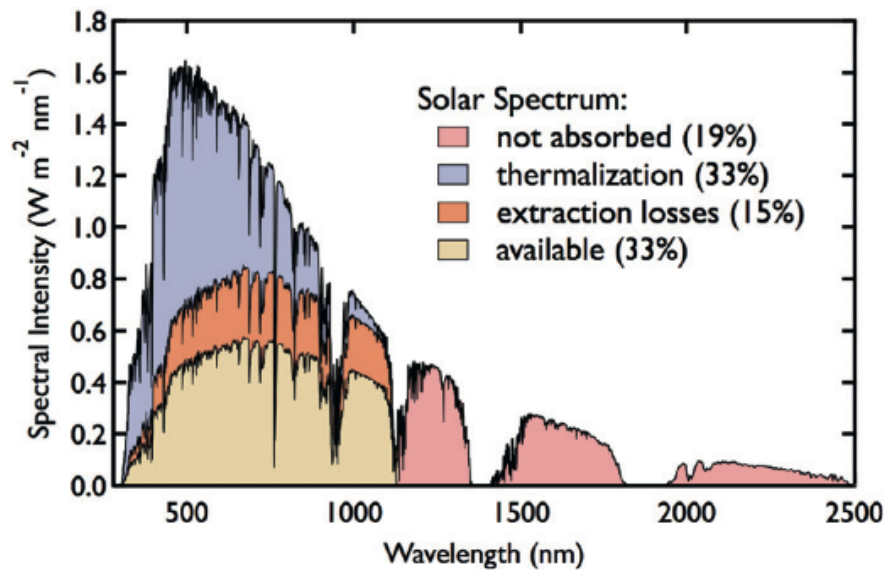


Figure 1.16: Analysis of the main losses of the solar spectrum in silicon solar cells. After[11].

In addition to the theoretical efficiency limit, the components of the solar cell contribute to lowering the performance due various types of losses. These losses can

be categorized as optical, electrical and recombination losses. Conventional solar cells consist of a p-n junction, an antireflective layer, front side electrodes on the top, and metallic back contact on the bottom. Flat silicon reflects about 36% of the incident light, and front electrodes typically shadow about 10% [30]. Recombination losses play a role in lowering the performance of the cell, particularly the open circuit voltage and FF. Not all the generated e-h pairs are collected unless the generation happens near the junction. Recombination also takes place in the depletion region via trap defects. Actual solar cells also have parasitic resistances, which are represented by series and shunt resistance. The series resistance results from various components of the cell: bulk resistance, interconnection, and the resistance between the bulk and interconnection. On other hand, shunt resistance results from leakage current across the junction and the edge of the cell. Both shunt resistance and series resistance tend to decrease the FF. Figure 1.17 shows the effect of various values of shunt and series resistance on the I - V characteristic of the diode. A large value of series resistance and a low shunt resistance will play a role in reducing both the open circuit voltage and the short circuit current.

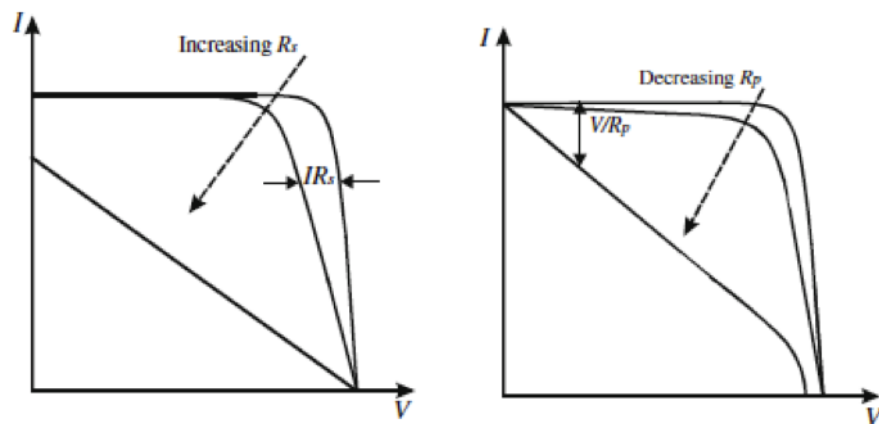


Figure 1.17: Effect of parasitic resistance on I - V characteristic of the illuminated p-n junction. After[23].

1.4 Solar Cell Technologies

1.4.1 Crystalline Solar Cells

To produce wafers, the silicon crystal is sliced into 0.2-0.5 mm thick. To fabricate silicon solar cells, the wafers undergo four basic processing steps. The first step is

oxidation, which is done by exposing the wafers to dry or wet oxygen. The oxide layer of SiO_2 serves as a passivation of the dangling bonds. The second step is doping the impurities by diffusion, which is done by thermal diffusion at $800 - 1200^\circ\text{C}$ in a clean environment. The impurity sources are typically phosphorus and boron for emitter and back surface, respectively. Then the electrical contacts of the cell are fabricated by vacuum evaporation. Lastly, an antireflection coating is deposited on top of the solar cell (see Figure 1.18) [31]. A standard single silicon crystal solar cell has dimensions of about $5 \times 15 \text{ cm}^2$ and produces 3-4.5 watts-peak (W_p). A module usually has 60-72 solar cells, and produces power ranging from 120-300 W_p , according to the size and efficiency of the module. The efficiencies are 14-22% and 12-19% for sc-Si and mc-Si, respectively.

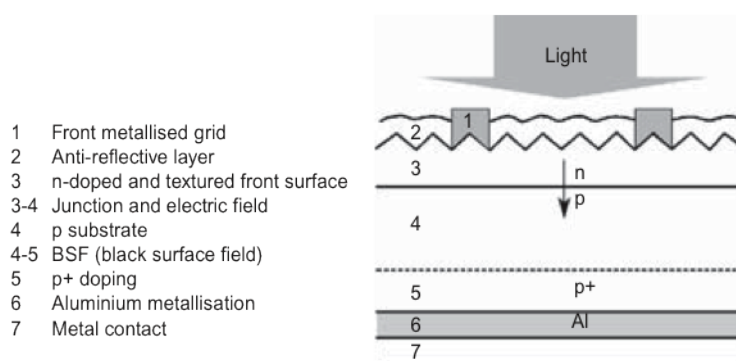


Figure 1.18: Cross section of a single crystal silicon solar cell. After [31].

1.5 Thin Film Technology

Thin film technology, which is also known as second generation PVs, is based on using very thin material, $\sim (5 - 50) \mu\text{m}$. This type of solar cell has several advantages over crystalline ones [32, 33]: one of these advantages is the low consumption of material, which causes a reduction in the cost of the solar cell. Another advantage is that thin films are deposited on a support substrate which allows the use of flexible materials e.g., polymer, glass, or stainless steel. The flexibility of these modules makes connection and integration of them into buildings much easier. Many research efforts have been made toward designing thin film solar cells with high efficiency [32, 33]. Several types of thin film material exist with efficiency which range from 8-20%. These thin film materials can be of crystalline silicon, amorphous silicon, ternary and

binary compound semiconductors.

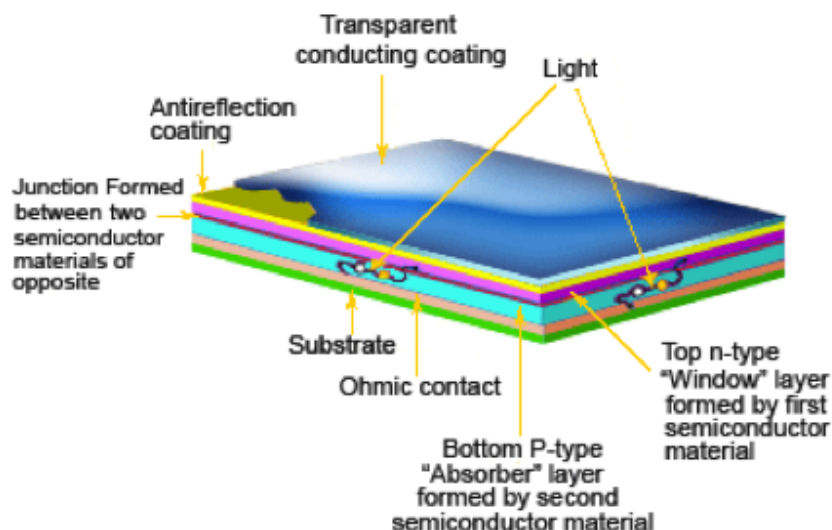


Figure 1.19: General structure of a thin film solar cell. After [34].

1.5.1 Crystalline Silicon

Crystalline silicon is a poorly absorbant material because of its an indirect bandgap and thus needs a thicker material to absorb all the incident photons. However, introducing light trapping designs can highly enhance the absorption of the material and further reduce the thickness [35]. Numerous efforts have been made toward reducing the wafer thickness down to $10\ \mu\text{m}$ [33]. These efforts attempt to fabricate crystalline thin film in the gas phase at a low temperature to reduce the cost of the wafer. For a very thin solar cell of $2.7\ \mu\text{m}$ made of plasma enhanced chemical vapour deposition (PECVD) at $220\ ^\circ\text{C}$, the efficiency was 8.5 % [36]. Higher efficiency solar cells can be obtained by introducing tandem (see Section 1.6) designs with amorphous silicon. The efficiency of this type of cell was 12% [37].

1.5.2 Amorphous Silicon

Amorphous silicon has different properties from crystalline silicon [33]. Amorphous silicon has a wider band gap of 1.7 eV and a higher absorption coefficient than crys-

talline silicon. Amorphous silicon is usually deposited at a low temperature via chemical vapour deposition (CVD) of a gas precursor (silane, SiH_4). The quality and stability of the material is related to the hydrogen content because higher hydrogen content yields higher stability. Amorphous silicon based solar cells are designed with an intrinsic layer (i) between n-type and p-type which enhances the mobility of generated carriers and allows better collection of them due to an increase of the internal electric field inside the junction. In these types of cells, light trapping is often used to yield better efficiency and stability [33]. Introducing a tandem design of a p-i-n junction stacks can further increase the efficiency of a single amorphous junction. The use of such a design is possible because of the low deposition temperature.

1.5.3 Copper Indium Diselenide and Related Materials

Copper indium diselenide (CIS) and copper indium gallium diselenide (CIGD) are ternary compound semiconductors. These compound semiconductors have direct band gaps and high absorption coefficients [32,33]. The band gap of these compounds is between 1.1-1.2 eV. A typical solar cell structure is based on the heterojunction of Cadmium sulfide (CdS) as the n-type and CIS and/or CIGD as the p-type. The highest efficiency achieved for a laboratory cell is 19 % for a 3 μm thickness polycrystalline cell of 0.408 cm^2 [38]. Attempts have been made toward introducing gallium into CuInSe_2 , which would allow an increase of the band gap and the performance of the cell [33].

1.5.4 Cadmium Telluride

Cadmium telluride (CdTe), a binary compound semiconductor, has a direct band gap of 1.45 eV [33]. This band gap is close to the optimum value for good conversion efficiency. CdTe as a direct bandgap semiconductor has an excellent absorption coefficient, and nearly all the visible light absorbs in a 1 μm depth [33]. Typical CdTe solar structure is similar to a CIGD cell, which is a heterojunction [32, 33]. However, the fabrication of binary compounds is easier than ternary compounds. The CdTe heterojunction is based on CdS as the n-type and the CdTe as the p-type. The efficiency of a laboratory cell CdTe reached 16% for a 1 cm^2 area [29].

1.6 Third Generation Photovoltaics

Several types of solar cells are considered as third generation: tandem solar cells, dye-sensitized solar cells, and organic solar cells.

1.6.1 Tandem Solar Cells

A tandem cell consists of stacked layers of a range of band gap junctions, where the layer in the top has the largest band gap, and the layer in the bottom has smallest one (see Figure 1.20) [39]. To get efficient power from each cell, every cell parameters must be optimized, i.e., bandgap, thickness of the cell, junction depth and doping level. Tandem solar cells are fabricated from various classes of materials and technologies, which impact the efficiency and the cost of the cell. Of these materials and technologies are III-V tandem, thin film tandem, and a-Si tandem. Group III-V tandem solar cells are considered as the highest quality and the most efficient tandem cell. This is because of high quality single crystals that are produced by epitaxial processes. For example, three layer tandem cells have efficiency of 34.1% for GaInP/GaInAs/Ga[40]. For an infinite number of layers, the maximum theoretical efficiency is expected to reach to about 68% for 1-sun intensity [39]. Even though this approach seems favorable to maximize the efficiency, the cost of fabrication was high. Other materials and technologies may give good efficiency at low cost, e.g., thin film tandem and a-Si tandem. Thin film and amorphous tandem solar cells have the advantages of lower cost of fabrication processes e.g., chemical vapour deposition (CVD). For a two stack cell of a-Si/ $\mu\text{c-Si}$ laboratory cell, the efficiency was 10.7 made by [41]. For a three stack cell of a-Si/A-SiGe/a-SiGe, the efficiency was 13% [42].

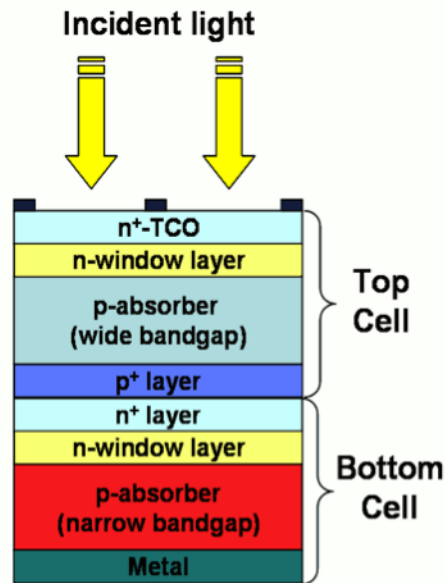


Figure 1.20: Structure of a two-junction tandem solar cell. After [39].

1.6.2 Dye Sensitized solar cells

Dye sensitized solar cells (DSSCs) have a typical configuration of: transparent conductive oxide (TCO), a network of TiO_2 nanoparticles, a monolayer of dye, an organic solvent (electrolyte) and a back electrode; Figure 1.21 [5, 43]. The TCO is deposited on a glass or plastic substrate and on top of the TCO is a layer of TiO_2 called the mesoporous oxide layer. The oxide layer has a thickness of $10\ \mu\text{m}$, and the nanoparticles size can range from $10\text{-}30\ \text{nm}$ [43]. The electrolyte contains iodide-tri-iodide as a redox system. The operation principle of the DSSCs is based on the fast regenerative photoelectrochemical process, where the operation of the cell is different from conventional solar cells [21]. When the light is absorbed by the dye, the excited electron is injected into the semiconductor conduction band by photoinduced injection at the interface between the TiO_2 and the dye leaving the dye in an oxidized state. Then, the electron transfers into a load to conduct the current. Since the dye is dissolved in a redox electrolyte made from organic solvent with iodide/triiodide ($\text{I}^- / \text{I}_3^-$), the dye is restored to its ground state by accepting electrons from iodide. Then I^- oxidizes into I_3^- , which diffuses into the electrode and allows regeneration of I^- again by electron transfer into the electrode. The process of regenerating the dye and the iodide is repeated continually in a very short time. The redox system gives DSSC an advantage over conventional solar cells [5] since charge transport is based on majority carriers,

not minority carriers as in conventional solar cells. This feature prevents bulk and surface recombination to occur, which in turn reduces the need for high quality material. The efficiencies of the best modules are $(11 \pm 0.3)\%$ and $(9.9 \pm 0.4)\%$ for Sharp and Sony companies, respectively [29].

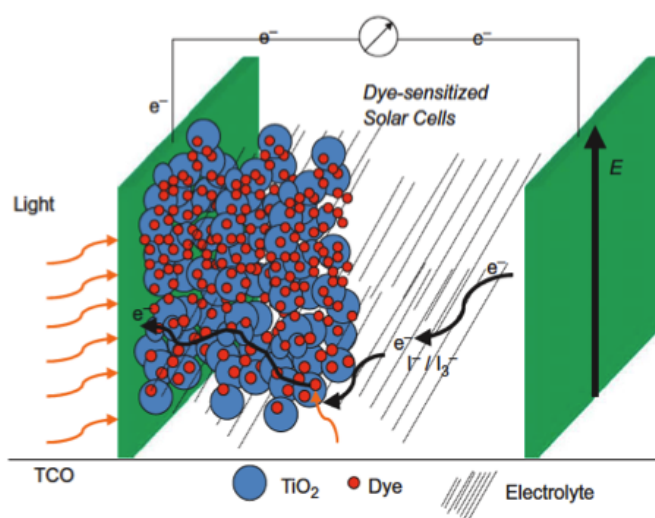


Figure 1.21: Schematic of a typical configuration of a dye-sensitized solar cell. After [43].

1.6.3 Organic Solar Cells

Organic materials offer the possibility of low cost, low-temperature processing and the use of a variety of substrates [5, 43]. Various types of organic materials can be used in solar cell applications, which involve molecules e.g., functionalized fullerene, perylene derivative and pentacene, and, conjugate polymer, e.g., polythiophenes and poly-perylene [43]. Organic materials can show p-type or n-type behaviour and have high absorption coefficients, which allow reduction of the material thickness down to $1 \mu\text{m}$. Organic materials differ from inorganic materials by their low mobility, high binding energy of the exciton, and charge transport occurs by a hopping mechanism [43]. These differences impose a restriction on the type of device for making solar cells, which is solved by making a heterojunction of acceptor and donor molecules. This design allows separation of the charge carriers. The working principle is also different from inorganic solar cells [43]. Figure 1.22 shows a schematic of a heterojunction between donor and acceptor molecules. In organic solar cells the open circuit voltage can be controlled by offsetting the high occupied molecular orbital (HOMO) energy

between the donor and the acceptor. Additionally, choosing a different work function of the electrodes can assist in the charge sweeping. Organic solar cells can be formed in a variety of designs e.g., bilayer, bulk heterojunction blend and tandem. The best efficiency of an organic solar cell was 5%, where C_{60} worked as acceptor and phthalocyanine CuPc as donor [43]. Good efficiency of 2.7 ± 0.4 % was also obtained for C_{60} and the pentacene heterojunction [44].

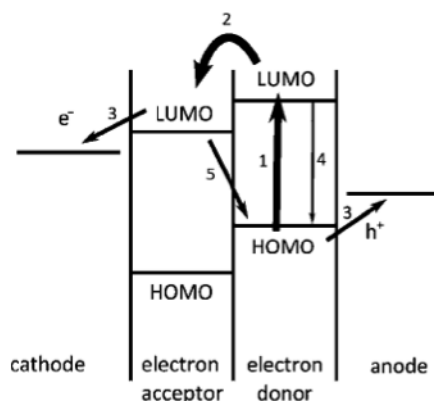


Figure 1.22: Schematic diagram of a heterojunction organic solar cell. The arrows show the operation principle. (1) Absorption of the light in the active layer is followed by either (4) decaying the exciton back to HOMO or (2) undergoing separation if it reaches the interface by hopping (3) completing the circuit to produce a current or (5) the exciton recombining back into HOMO after the separation. After [43].

1.7 Nanostructured Solar Cells

Solar cells based on nanostructures offer the possibility of band gap tunability via quantum confinement and enhancement of photoluminescent properties compared to the counter part bulk semiconductors[17,45,46]. Novel concepts involving nano structures in solar cells have been proposed that could lead to high efficiency solar cells. These include hot carriers, multiple exciton generation, intermediate band, down-conversion, and up-conversion [45,47]. The goal of these approaches is to boost the conversion efficiency beyond the Shockley-Queisser limit of a single junction (Figure 1.23).

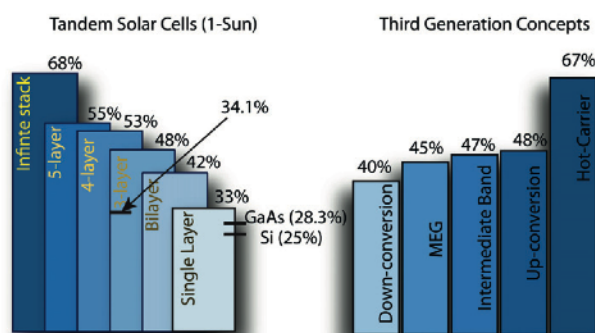


Figure 1.23: Maximum conversion efficiency limits for single junction, tandem cells and new concepts based on nanostructures. After [11].

1.7.1 Hot Carriers

The hot carrier concept is based on the extraction of e-h pairs before they relax through phonon scattering [50]. When a photon with energy greater than the band gap is absorbed, the generated e-h pair has high energy, which is often lost via thermalization. The e-h pair with high energy is referred as a hot carrier. This hot electron and hole can boost the efficiency if they are collected before they lose their energy. Hot carrier solar cells can increase the photovoltage of the cell by using a selective energy contact; see Figure 1.24. The efficiency is expected to reach a maximum value of 86% under a one-sun concentration. As stated previously, those thermalization losses account for 33% of the energy of the absorbed photon. Experimental research on hot carriers is still under investigation. From these investigations, the use of a selective energy contact via a double-barrier resonant tunneling structure with a layer of Si quantum dots (QDs) has been explored [48].

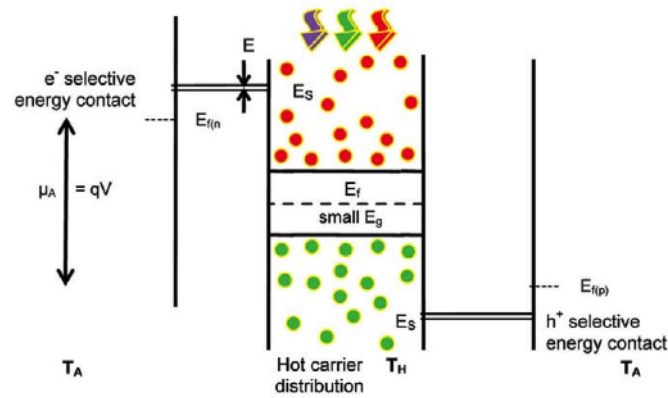


Figure 1.24: Band diagram of a hot carrier solar cell and how to allow collection of hot carriers before cooling through a selective energy contact. After [48].

1.7.2 Intermediate Band Solar Cells

Intermediate band (IB) solar cells are based on forming an intermediate band within the semiconductor band gap. This concept is expected to enhance the photocurrent of a solar cell by absorbing sub-band gap energy photons. When a photon is absorbed, the excited electron can be promoted from the valence band (VB) into IB. Then a second photon excites the electron from the IB into the conduction band (CB). A way to form IB is via quantum dots, where a multilayered stack of QDs is often used in conventional solar cells e.g., p-i-n junction where the (i) layer is a stack of QDs. An example of such a design is a p-i-n junction where the (i) layer consists of multi-stacked InGaAs/GaAs QDs on a GaAs solar cell [49].

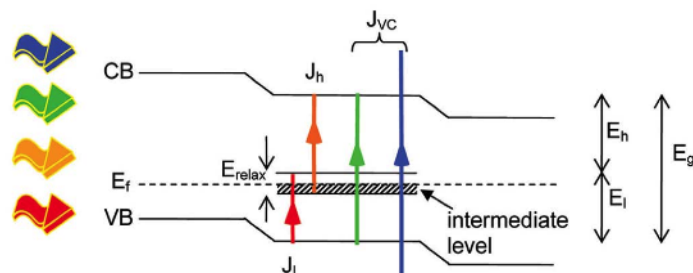


Figure 1.25: Intermediate band solar cell concept where the red and orange arrows are for electron transition from VB to IB, then from IB to CB, and green and blue arrows are for regular solar cell absorption. After [48].

1.7.3 Multiexciton Generation

Enhancement of photocurrent can also be achieved via multiexciton generation (MEG) [24]. MEG occurs when one high-energy photon of at least twice the band gap is able to create more than one e-h pair from one photon (Figure 1.26). This would result in an increase of solar cell efficiency by avoiding thermal losses due to higher photon energies.

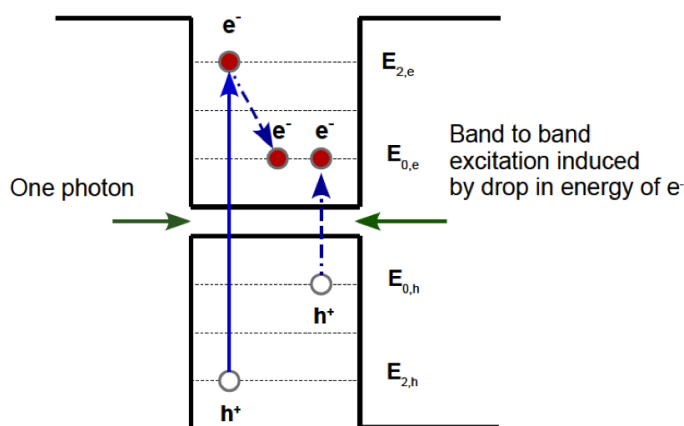


Figure 1.26: Concept of multiexciton generation, when one high-energy photon at least twice E_g , creates two e-h pairs. Adopted from [48].

1.7.4 Up and Down Conversion

Up-conversion (UC) and down-conversion (DC) is a simple concept based on modulating the incident photon energy into lower or higher energy than the band gap energy. This concept can further enhance the performance of a single junction solar cell [48]. For a DC cell, the down conversion layer is placed on the top of the cell (Figure 1.27). The DC layer functions as a converter of high-energy photons into two photons with lower energy e.g., an ultraviolet photon into two visible photons. In contrast, the UC is placed on the bottom of the cell, in which the UC layer serves as a converter of the sub-band photon into a photon with energy higher than the bandgap (Figure 1.27). In both types, the converter layer is separated from the cell, and the absorbed photon is reemitted into the cell.

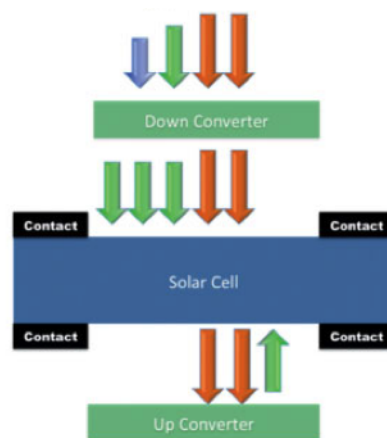


Figure 1.27: Schematic representations of down-conversion and up-conversion. In the down-conversion method a quantum dot layer is placed on top of the solar cell and an up-conversion layer of quantum dots is placed on the bottom. After [50].

1.8 Colloidal Quantum Dot Solar Cells

Solution-processed solar cells are a promising route for convenient and low-cost fabrication that can be employed in large scale production of solar cells via techniques such as spray, ink-jet, and reel-to reel printing (see Figure 1.28) [51]. Organic solar cells have been examples of such a route for low-cost solar cell production; however, organic materials suffer from a limited absorption spectrum as well as low carrier mobility [58]. On the other hand, colloidal nanoparticles have been an interesting route for synthesizing solar cells. In fact, colloidal nanoparticles own the same advantage of organic solar cells, but with extra features. Colloidal nanoparticle properties can be tuned via quantum confinement effects and surface functionalization. By controlling the size, the band gap can be engineered to absorb a wide-range of the solar spectrum. In addition, the surface of these colloidal nanoparticles can be manipulated to change their electrical properties. A variety of materials have been investigated for colloidal solar cells, e.g., PbS, PbSe, Si, and CdS[52–54]. However, lead selenide and lead sulfide NCs are the most investigated materials for colloidal solar cells because they are promising materials for harvesting the infrared spectrum [52]. All these materials have been investigated in a variety of solar cells designs such as (metal-semiconductor junction) Schottky, heterojunction and tandem cells.

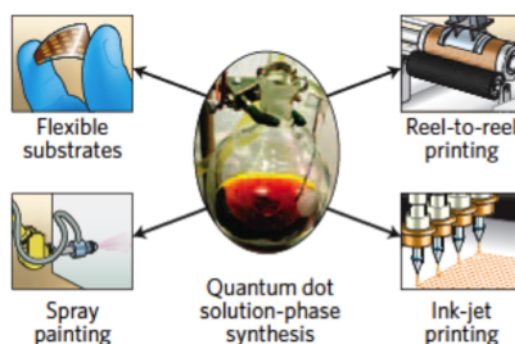


Figure 1.28: Solution-phase synthesis is a promising route for inexpensive solar cells, where the colloidal quantum dots can be deposited onto a flexible substrate via techniques such as spray painting, reel-to-reel printing and ink-jet printing. After [51].

The Schottky solar cell is one of the simplest colloidal devices, which consists of a transparent conductive oxide (TCO), layer of colloidal quantum dots as p-type (CQDs) and metal contact at the back of the cell. The first reported Schottky cells had very low efficiency of $\approx 1\%$ for ITO/PbSNC film/Mg [55]. Similar device architectures have been reported with improved efficiency of 2.1% and 3.6%, respectively [56, 57]. Figure 1.29 shows the device structure of a Schottky solar cell in ref. [56]. Good infrared conversion efficiency of 4.2% has been achieved for Schottky colloidal solar cell made from PbS NC film [64]. This efficiency has been achieved via replacing the passivation ligand molecules with shorter ones and also modifying the device parameters.

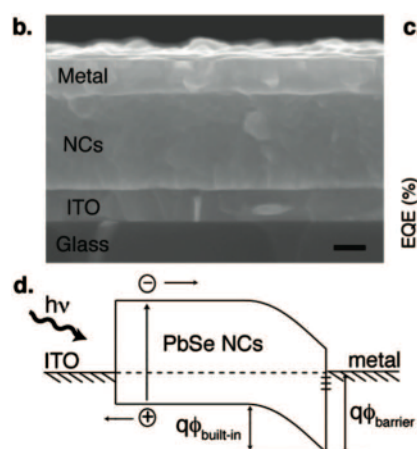


Figure 1.29: (Top) shows scanning electron microscopy (SEM) cross-section of the Schottky solar cell that has the structure of ITO/NC film/metal, and the scale bar is 100nm. (bottom) shows the band diagram of a Schottky cell, where the band bending occurs at the interface between the nanocrystal (NC) film and the electrode. After [56].

A depleted heterojunction solar cell is another type of colloidal solar cell that has been of great interest. The design of the depleted heterojunction is more complicated than a Schottky cell: instead of forming a junction between a metal and NC film, the junction forms between the semiconductor oxide and semiconductor NC film. Heterojunction solar cells benefit from the depletion region on both sides of the NC film and the semiconductor oxide. In contrast, in Schottky solar cells, the depletion region on the metal side is neglected because the electron density is very high. Another advantage of the heterojunction is that the absorption of light happens close to the junction which facilitates carrier extraction. On the other hand, in Schottky junctions, the absorption takes place away from the junction, which means the carrier will have a high probability of recombination due to the distance they travel. Similar to Schottky solar cells, the most studied materials for heterojunction are PbS and PbSe[20, 58, 59]. For a PbS CQDs heterojunction, the devices consist of layers of FTO/TiO₂/PbS CQDs/ Au/Ag. One device has an efficiency and current density of 5.1% and 16.2 mA/cm², respectively. On the other hand, another device passivated with monovalent halide anion had an efficiency and current density of 5.54% and 18 mA/cm², respectively. An enhancement of the photocurrent of PbSe QD heterojunctions has also been reached via controlled passivation [58]. Here, the PbSe QDs is passivated with 1,2-ethanedithiol EDT and hydriized. The enhancement of

the photocurrent is confirmed by both the external and internal quantum efficiencies.

Other types of heterojunctions were also investigated such as quantum junctions made of quantum dots and organic/nanocrystal composites in a heterojunction blend architecture [60,61]. In the quantum junction, a p-n junction forms between quantum dot solids instead of a semiconductor heterojunction with colloidal quantum dots. The success of improving such a device relies on controlling the doping of both layers. The best record of conversion efficiency of a quantum junction of n-PbS/p-PbS is 6.1 % [62].

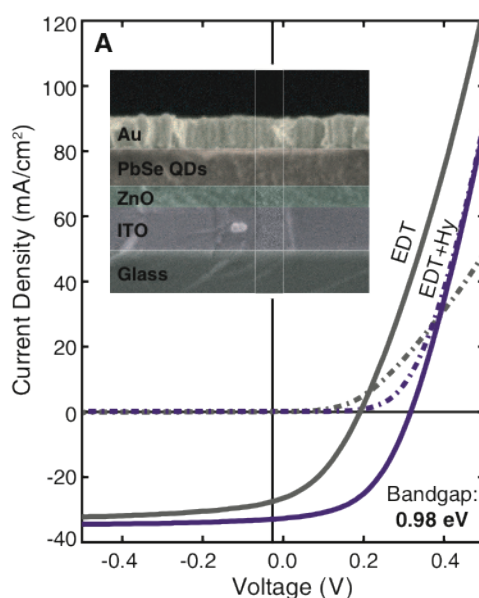


Figure 1.30: Comparison of I-V characteristics for a heterojunction structure that consists of Au/PbSe QDs/ZnO/ITO/glass with EDT and with EDT and hydrazine treatment. The inset shows an SEM cross-section of the device structure. After [58].

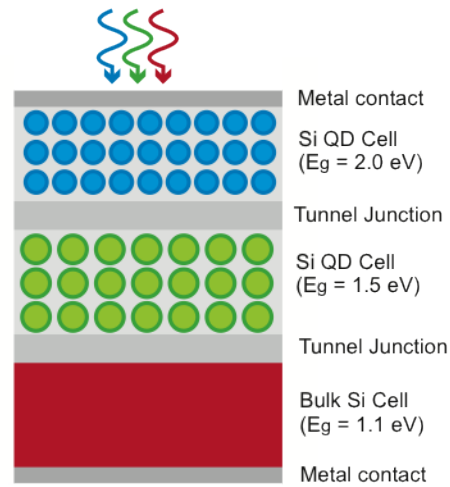


Figure 1.31: Schematic diagram of a silicon tandem cell based on two layers of SiQDs with band gaps of 2 and 1.5 eV for the top and second layer, respectively. After [63].

The other QD solar cell that can be utilized to reduce thermalization losses is the tandem cells [64]. In this configuration, QDs can be placed on top of a single junction solar cell, in which the top layer absorbs high-energy photons, while the second layer absorb the low energy photons. Wang et al have reported a PbS QD tandem cell with an efficiency and current density of 4.2% and 8.3 mA/cm² [65].

1.9 Thesis Outline and Scope of Research

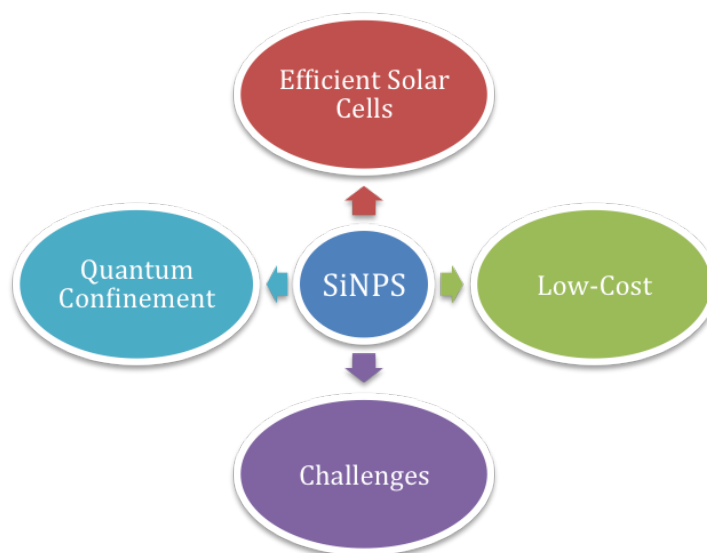


Figure 1.32: Motivation and challenges of using Si nanoparticle thin film.

Solution processed inorganic nanoparticle thin films are becoming attractive as a route for low-cost and easy processing of optoelectronic devices. These advantages arise because Si nanoparticles in solution allow low temperature deposition and using flexible substrates, similar to amorphous silicon deposition. Additionally, thin films made of nanoparticles offer the possibility of band gap tuning through quantum confinement, and, thus, enlargement of the band gap for enhancing the device response to particular wavelengths is possible. To control the properties of the particle film, it is necessary to control the size-distribution, shape, and surface properties. Figure 1.32 summarize the motivation and challenges of using Si nano particles. This thesis investigates the possibility of controlling the properties of Si nanoparticles via a low-cost colloidal grinding approach. The research investigated is organized as follows:

Chapter 2 A semi-empirical modeling method is employed to study the electronic properties of silicon particles depending on the size/shape of the silicon particles and surface passivation.

Chapter 3 A simple and straightforward approach for silicon nanoparticles synthesis via colloidal grinding in solution is presented. Control of particle size-distribution and morphology via centrifugation has been demonstrated. Val-

idation of the approach is confirmed using analysis tools such as scanning electron microscopy, Raman spectroscopy, energy-dispersive X-ray spectroscopy and current-voltage characterization.

Chapter 4 A summary of the research project and possible future work is presented and discussed.

Chapter 2

Modeling Silicon Nanoparticles

Semi-empirical approaches are computational methods that aim to solve the Schrodinger equation for many electron systems. In many electron systems, the electron-electron correlation becomes more important, and include methods such correlations makes the calculation more complex and difficult to manipulate. To solve the Schrodinger equation for many electron systems, approximation methods must be used. Approximation methods are an essential part of computational chemistry including methods such as variation principal, perturbation, or fitting parameters to reproduce experimental data. When fitting parameters are used to solve Schrodinger equation, the method is known as semi-empirical. To correct the results from approximating or neglecting some integrals, the semi-empirical method is parameterized. The parameterization is introduced by curve fitting of the parameter or number from the experimental data. In this way, the result can give good agreement to the experimental result. In semi-empirical theory there are three major approximation schemes that have been introduced [66, 67]:

1. Eliminating the core electrons from the calculation.
2. Using a minimum basis set.
3. Reducing the number of two electron integrals.

Eliminating the core electrons means replacing the entire core (the nucleus and core electrons) by parameterized functions instead of involving them in the calculation directly because these core electrons do not contribute to the physical/chemical properties to the same extent as valence electrons. For this reason, in semi-empirical

methods only the valence electrons can be treated, which allows the use of a minimum basis set. The last approximation that reduces the cost and complexity of the calculation is based on the reduction of two electron integrals from the calculation. Even though this kind of parameterization makes the calculation faster, the result may not be as accurate as ab-initio methods (see below) if the molecule under investigation has an element not included in the parameterization[66].

Ab-initio calculations involve various methods based on different types of approximation e.g., Hartree Fock (HF), density functional theory (DFT) etc. Hartree Fock is considered to be the main branch of all other calculations because the other approximated calculations start with HF and then further correction or modification is involved (Figure 2.1). One type of approximation takes the Columbic electron-electron repulsion as a net effect known as the central field approximation; calculated energies are equal or greater than the exact energy variational calculation. The core electrons/nucleus are represented by approximate or pseudopotentials in these approaches. In addition, HF calculations and all ab-initio involve approximating the wave function into functional form, where the total wave function or the molecular orbitals (MO) are expressed as a Linear Combination of Atomic Orbitals (LCAO) or basis set. Other ab-initio calculations that explicitly include electron-electron repulsion are known to have correlated calculations e.g., Mller-Plesset perturbation theory (MP_n, where n is the order of correction), Multi-Configuration Self Consistent Field (MCSCF), Configuration Interaction (CI), etc. The ab-initio method based on DFT has an alternative calculation based on dealing with total electron density instead of wave function. Ab-initio methods are able to give a high quality result, especially for very small systems, with few atoms. However, these calculations are expensive owing to CPU time, memory and disk space. For example, the HF method scales as N^4 , where N is the number of basis sets [66].

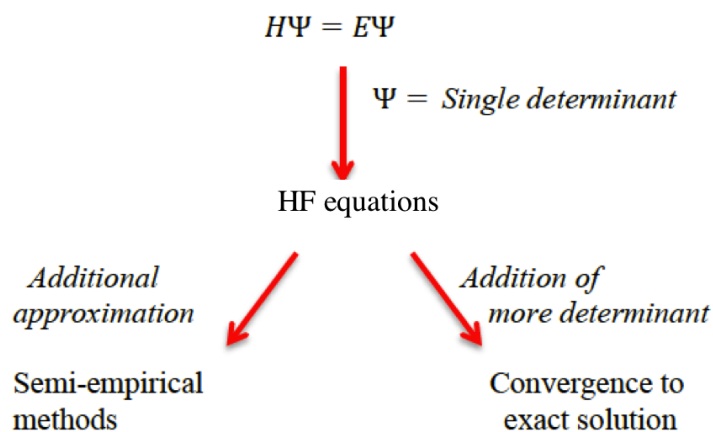


Figure 2.1: HF as the starting point for other approximations. Adopted from [66].

2.1 Theory

To find the energies and MO for any system, one needs to solve the time-independent Schrodinger equation (Eq 2.1) where H is the Hamiltonian operator that can be written as a summation of all kinetic energies and potentials of the nucleus and electrons [66].

$$H_{tot}\Psi = E\Psi \quad (2.1)$$

$$H_{tot} = T_n + T_e + V_{ee} + V_{ne} + V_{nn} \quad (2.2)$$

Where T_n is the kinetic energy of the nucleus, T_e is the kinetic energy of the electrons, V_{ee} is the electron-electron repulsion always referred as the two-electron centre, V_{ne} is the nucleus-electron attraction referred as the one-electron centre, and V_{nn} is the nucleus-nucleus repulsion. Because electrons are light particles and their movement is faster than the nucleus, the movement of the nucleus is often neglected. This assumption is known as the Born-Oppenheimer approximation, which allows the total Hamiltonian to be written as (Eq 2.3)[66]:

$$H_{tot} = H_{elec} + H_{nuc} \quad (2.3)$$

$$H_{elec} = - \sum_{i=1}^{N_{elec}} \frac{1}{2} \nabla_i^2 + \sum_{i=1}^{N_{nuc}} \sum_{i=1}^{N_{elec}} \frac{Z_a}{|R_a - r_i|} + \sum_{i=1}^{N_{elec}} \sum_{j>i}^{N_{elec}} \frac{1}{|r_i - r_j|} \quad (2.4)$$

$$V_{nn} = \sum_{i=1}^{N_{nuc}} \sum_{b>a}^{N_{nuc}} \frac{Z_a Z_b}{|R_a - R_b|} \quad (2.5)$$

The Schrodinger equation can now be solved for the electronic part only since the potential energies of the nucleus is assumed constant. For fixed nuclear coordinates, the Schrodinger equation becomes as (Eq 2.6):

$$H_{elec} \Psi_{elec} = E_{elec} \Psi_{elec} \quad (2.6)$$

Where Ψ_{elec} is the electronic wave function which represents the spatial orbitals and spin function. Approximation methods are necessary to simplify the problem of electron correlations; instead of exact electron correlation, the interaction between electrons is treated in average fashion[66].

In the Hartree Fock approximation scheme[66]:

$$H_{HF} \Psi_{HF} = E_{HF} \Psi_{HF} \quad (2.7)$$

The HF wave function must be antisymmetric and obey Pauli's principle because electrons are fermions with spin ($\pm\frac{1}{2}$). Thus, no two electrons can have all the quantum numbers the same, and any exchange between two electrons should change its sign. These conditions can be achieved by building the wave function from Slater determinants (SD) (Eq 2.8):

$$\Phi_{SD} = \frac{1}{\sqrt{N!}} \begin{vmatrix} \phi_1(1) & \phi_2(1) & \cdots & \phi_N(1) \\ \phi_1(2) & \phi_2(2) & \cdots & \phi_N(2) \\ \vdots & \vdots & \ddots & \vdots \\ \phi_1(N) & \phi_2(N) & \cdots & \phi_N(N) \end{vmatrix} \quad (2.8)$$

The one-electron wave functions (ϕ) are referred to as molecular orbitals that are expressed as a linear combination of spatial and spin functions (α and β), where α is for spin up and β is for spin down. The MO is usually expanded in term of basis functions χ or atomic orbitals.

$$\phi_i = \sum_{i=a}^{Mbasis} C_{\alpha i} \chi_{\alpha} \quad (2.9)$$

$$F_i = h_i + \sum_{i=j}^{Nelec} (J_j + K_j) \quad (2.10)$$

Now, in the HF approximation, the Hamiltonian is the summation of one-electron operators, where h_i describes the kinetic energy of the electron and the attraction to all nucleus and J and K terms describe the repulsion and exchange between two-electrons, respectively. Because h_i depends on one electron coordinates, it is referred to as a one-electron operator. On the other hand, J and K depend on two electron coordinates; they are referred to as two-electron operators for Columbic and exchange interaction, respectively. After applying the variation principle to the find the set of MOs that make the energy of the system a minimum, the HF equation can be written in a matrix form as follows [66].

$$FC = SC\varepsilon \quad (2.11)$$

(Eq.2.11) is known as the Roothaan-Hall equation for a closed shell system, where F and S are matrices composed of Fock elements and overlap elements between basis functions, respectively, ε , a matrix of orbital energies and C is a matrix of the coefficient.

$$F_{\alpha\beta} = \langle \chi_{\alpha} | F | \chi_{\beta} \rangle \quad (2.12)$$

$$S_{\alpha\beta} = \langle \chi_{\alpha} | \chi_{\beta} \rangle \quad (2.13)$$

$$(2.14)$$

The total energy of the system is:

$$E = \sum_{i=1}^{Nelec} \varepsilon_i - \frac{1}{2} \sum_{ij}^{nNelec} (J_{ij} - K_{ij}) + V_{nn} \quad (2.15)$$

$$\varepsilon_i = \langle \phi_i | F_i | \phi_i \rangle = h_i + \sum_j^{Nelec} (J_{ij} - K_{ij}) \quad (2.16)$$

To find the MOs that make the energy minimum, iterative methods must be applied to solve the Roothaan-Hall equations. The solution is obtained via self-consistent field (SCF) orbitals. To find the best MO, the iterative procedure starts with an initial guess of the MO coefficients [66], followed by calculating the Fock matrix and the overlap or density matrix. Figure 2.2 illustrates the procedure of SCF approximation in which the process is repeated until the density matrix becomes close to the previous input in order to achieve consistency [66]. If the procedure fails to converge, another convergence scheme can be employed to assist the convergence e.g., extrapolation, damping, level shifting and direct inversion in the iterative subspace (DIIS) [66]. Any of these convergence schemes could be used to make the convergence faster, reduce the total energy of the structure, and reduce the number of the iterations required.

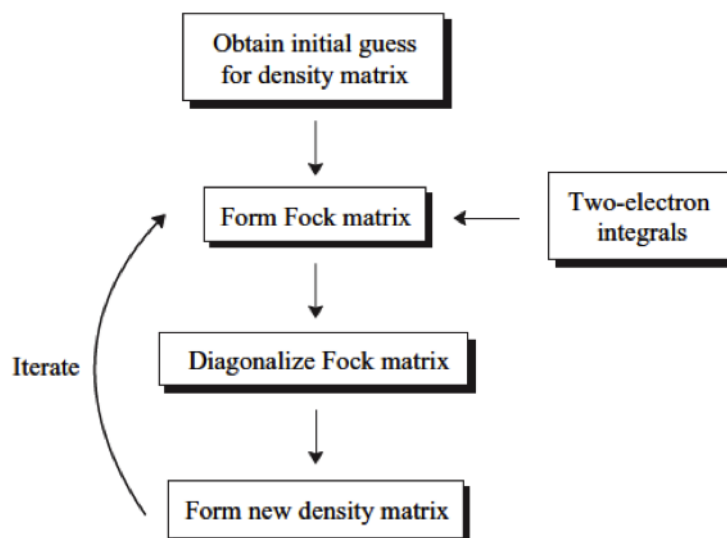


Figure 2.2: Illustration of the procedure in SCF approximation. After [66].

2.2 Semi-empirical Methods

Semi-empirical methods vary according to the approximation and parameterization that have been used [66, 67]. These approximations and parameterizations aim to reduce the cost of computation, in particular two-electron integrals (Coulomb and exchange) that is considered the most expensive part of the calculation in ab-initio methods. These methods are modified neglect diatomic overlap (MNDO), Austin Model 1 (AM1), and Parameterized Model number 3 (PM3). MNDO was developed by Dewar and Thiel in 1977 and parameterized based on different atomic types. The parameterization was created via curve fitting to reproduce certain experimental values, e.g., heat of formation, geometrical variables, dipole moment, and ionization energies. The MNDO method suffers from some deficiencies that make the calculation unreliable for predicting certain properties e.g., poor descriptions of hydrogen bonds and heat of formation. Another semi-empirical method that is based on similar approach is AM1 developed by Dewar and co-worker'. AM1 undergoes some modification in order to recover the deficiencies in MNDO. Dewar and his group added a new expression for nuclear-nuclear repulsion that minimizes the van der Waal interactions. Also, AM1 has new parameterizations that are based on some properties such as dipole moments, ionization potential, and geometry of molecules. AM1 also has some deficiencies, such as incorrectly predicting the lowest energy of water dimer. PM3, developed by James Stewart, has a similar Hamiltonian to AM1, but it is based on different parameterization. In general, PM3 and AM1 perform similarly for most calculation.

2.3 Configuration Interaction Method

Configuration interaction is a correlation method used to calculate the excited state of a system starting from the ground state Hartree Fock determinant. For constructing the excited state of a molecule, one can promote single, double, triple ... etc. electrons to virtual orbitals see (Figure 2.3). The constructed wave function is a linear combination of HF determinant and other possible determinants [68]. The exact electronic wave function for the system of n-electrons can be written in the form:

$$\Phi = c_0\phi_0 + \sum_{i,a} c_i^a \phi_i^a + \sum_{i<j,a<b} c_{ij}^{ab} \phi_{ij}^{ab} + \sum_{i<j<k,a<b<c} c_{ijk}^{abc} \phi_{ijk}^{abc} + \dots \quad (2.17)$$

$$\text{Possible number combinations} = \frac{2N!}{[n!(2N-n)!]} \quad (2.18)$$

where ϕ_0 is the HF determinant, ϕ_i^a , ϕ_{ij}^{ab} , and ϕ_{ijk}^{abc} are the possible determinants that result from promoting one, two, or three electrons in virtual orbitals, respectively, and c's are the expansion coefficients for all determinants.

Configuration interaction (CI) involves two methods for calculating the excited state. One is a complete method to find the wave function, and it is called a full configuration interaction (FCI). The other method is truncated CI, and it has several truncated methods such as configuration interaction single (CIS), configuration interaction single double (CISD). For FCI wave function, the sum is over other possible substitutions (Eq 2.17) and that gives a complete description of the system; as N grows FCI will approach the exact solution of the nonrelativistic Schrodinger equation. However, in practice the FCI is limited in the number of basis sets and to a very small system because of the large possible number of combinations. The total number of combinations is found from (Eq 2.18). For example, if we have 10 electrons and 20 basis set functions, then the number of combinations will be 8.477×10^8 [66]. In order to make CI calculations feasible for different sized systems, a truncated method is needed to reduce the number of excited state determinants, and examples of the truncated method are CIS and CISD. CIS does not give any improvement over Hartree Fock, and it gives the energy equal to the ground state energy for HF. The CISD involves promotion of single and double electrons from their orbitals to virtual orbitals. CISD method can be used for different size molecules, and improves over CIS method because it takes into account the correlation energy, and that make it feasible for calculation of small and medium-sized molecules. For medium size molecules, it covers 80-90% of the correlation energy and the coverage becomes higher for small molecules.

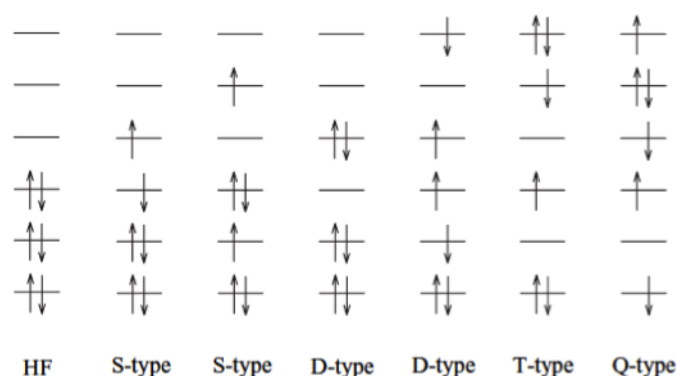


Figure 2.3: Possible excited state configurations for generating the final determinant for single, double, triple and quadruple excitation along with HF as reference. After [66].

2.4 Geometry Optimization

Geometry optimization is an essential step to find the equilibrium structure of a molecule under investigation where its energy is at minimum [67]. Geometry optimization is necessary to calculate physical and chemical properties since any slight change in the structure will change its energy and subsequently all other physical and chemical properties. As we go from a simple diatomic molecule to a large molecule systems, the parameters that affect the structure become complex. This means the potential energy surface (PES) that links the structure to its energy become multi-dimensional and difficult to plot [67]. For a simple diatomic molecule, the PES is a two-dimensional curve where the x-axis is the distance between the atoms and the y-axis represents the energy of the structure at any distance between the atoms i.e., the PES is a simple curve. On the other hand, for a large system, many parameters play a role in determining the minimum energy of the structure under investigation e.g., bond lengths and angles. Figure 2.4 illustrates the concept of PES for a molecule that has two degrees of freedom [67]. The PES is a surface plot in which every point on the PES represents a particular structure. Thus, finding an equilibrium structure means locating its minimum energy on the PES. It is possible to locate a local minimum, global minimum or transition state (see Figure 2.4) [67].

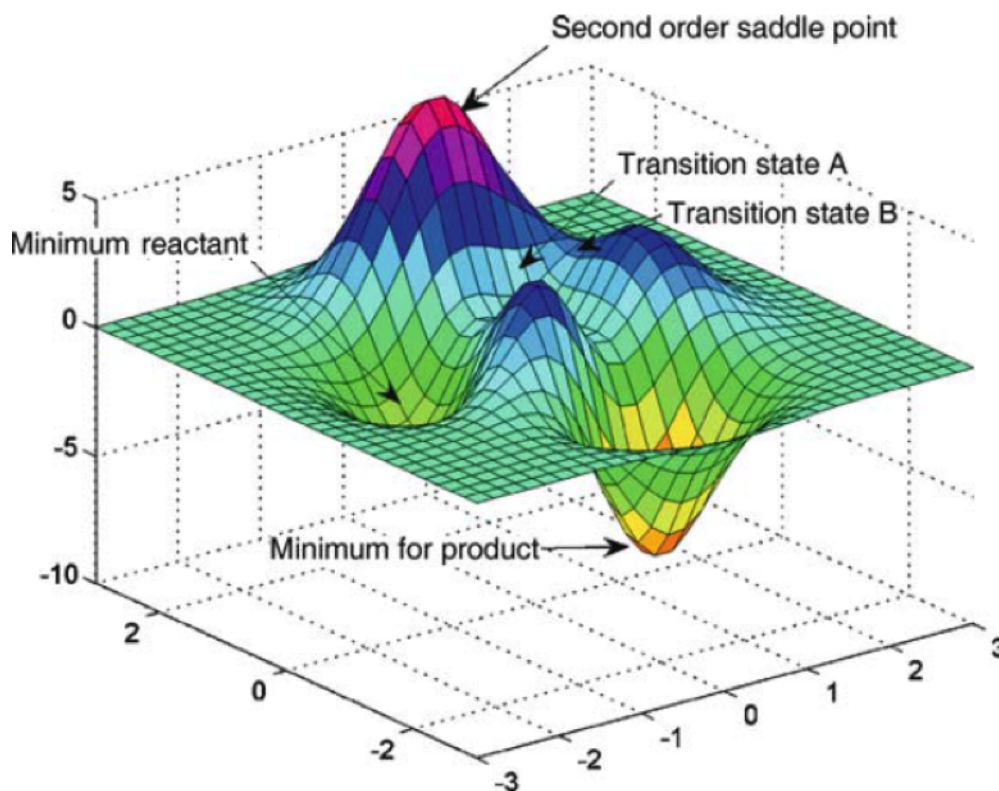


Figure 2.4: Illustration of the potential energy surface for a molecule that has two degrees of freedom. After [67].

It is clearly seen from the figure that the local and global minimum are the lowest energy in the PES. On the other hand, the maximum energy indicates a transition state. To identify the minimum energy from the transition state, the gradient is used because the gradient is zero when the energy at minimum and the forces as well [67]. When the force is zero, then we may locate a stationary point. In most computational programs, an initial cut-off is set up and then if the value is obtained after geometry optimization below that cut-off, the structure is considered to converge to its stationary point [67]. Examples of these cut off values are forces, root mean square, displacement and root mean square of the displacement [67].

Based on the minimum energy obtained for the structure under investigation from geometry optimization, some chemical and physical properties are calculated e.g., heat of formation. In semi-empirical methods, the heat of formation is calculated during geometry optimization and is represented by a curve that changes with iteration until the optimization is finished. The heat of formation of a molecule, is the energy

needed to form the molecule from its components (atoms) [69]. To calculate the heat of formation in any SCF semi-empirical program, the following procedure is conducted see (Figure 2.5): the program is encoded with the experimental values of the heat of formation and semi-empirical energies of individual atoms. Then by using the total energy of the optimized molecule, we can get the heat of formation (Eq.2.19) [69].

$$\Delta H_{f298}^{\ominus}(M) = \sum \Delta H_{f298}^{\ominus}(A_i) - F \sum E_{SE}(A_i) + F E_{SE}^{total} \quad (2.19)$$

where: $\Delta H_{f298}^{\ominus}(M)$ is the heat of formation of the molecule in Kcal/mol, $\Delta H_{f298}^{\ominus}(A_i)$ is the experimental value of the heat of formation for an individual atom, $\sum E_{SE}(A_i)$ is the calculated energies of individual atom, E_{SE}^{total} is the total energy of the optimized molecule, and F is a conversion factor to convert the energy from Hartree to Kcal/mol.

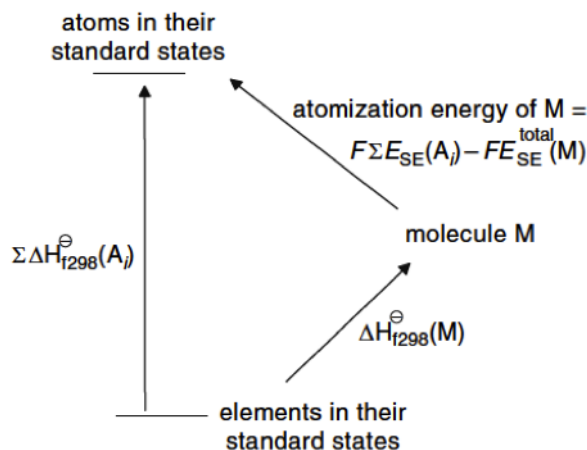


Figure 2.5: The principle for calculating heat of formation in any SCF semi-empirical program, where the program is encoded with values of heat of formation of atoms and then the atomization energy of the molecule is calculated to obtain the heat of formation of the optimized molecule. After [69].

2.5 Modeling Silicon Quantum Dots

Silicon nanocrystals (SiNCs) became an important research topic after the observation of high photoluminescence in porous silicon [70] and the great interest toward low cost and high efficiency solar cells. Bulk silicon is an indirect bandgap material with an E_g of about 1.12 eV; however, as the size of silicon becomes smaller than

the Bohr radius size-dependent bandgap becomes important in addition to surface effects. The size-dependent bandgap of SiNCs has been reported in many experimental and theoretical research [21, 71]. The bandgap is affected by surface effects such as passivation, strain, and interface effects. Some experimental data has shown that hydrogenated-SiNCs (H-SiNCs) shows up to 60% photoluminescent quantum yield [71]. However, after being exposed to air, the quantum yield reduces to a lower value due to the formation of amorphous silicon oxide. Moreover, the formation of dangling bonds in H-SiNCs has been investigated theoretically using TD-DFT for $Si_{66}H_{63}$ [21]. It was found that the formation of one dangling bond caused the formation of a defect state inside the HOMO-LUMO gap, which serves as a trap and nonradiative centre. Passivation of surface states is necessary to obtain a high quantum yield. In addition, to investigate the photoluminescence, many researchers also study the effect of oxidation on the HOMO-LUMO since silicon can be easily oxidized under ambient conditions. Theoretical research shows formation of an oxide shell reduces the HOMO-LUMO gap.

2.5.1 Structure Construction

All SiNC structures were constructed from the bulk silicon lattice imported from the Materials Studio Library [72]. The unit cell of silicon is expanded in all three dimensions by using different numbers of unit cells in X, Y and Z directions. The number of unit cells chosen in any direction depends on the shape of the structure. For cubic shaped SiNCs, the number of unit cells in all directions is the same. In contrast, for a rectangular shape, the number of unit cells is different. For other shapes like flat disk and ellipsoidal, the shape is defined by drawing the shape on the [100] plane and then removing all the silicon atoms that exist outside the shape (see Figure 2.10 and Figure 2.11). Additionally, for flat disk and ellipsoidal, any silicon atom that has three dangling bonds is removed following the procedure in the literature [73]. Finally, all structures are passivated with hydrogen as reported previously in the literature [21, 74, 75]. In the end, the constructed SiNCs are divided into two groups: one with two or three hydrogen atoms bonded at the surface and the other group has one or two hydrogen atoms [74, 75].

1. Group one: cubic and rectangular SiNCs
2. Group two: flat disk and ellipsoidal SiNCs.

SiNCs of different sizes and shapes are constructed following the above procedure. For specifically defining the size for every shape group, the bigger sized SiNC is built and gradually its size decreased to obtain three additional sizes except for cubic SiNCs. All the shapes are built in a way that two lengths are constant and the third is variable. In this manner, observation of the change in the HOMO-LUMO gap and optical properties according to their shape and size is possible.

2.5.2 Cubic SiNCs

Every cubic SiNC has two lengths which have the same value while the third is different (see Table 2.1) and Figure 2.6 shows an image of the largest model of cubic SiNC. The dimensions of every shape is illustrated in Figure 2.7 .

Table 2.1: Cubic SiNCs dimensions.

Structure	a Å	b Å	c Å	total number of atoms
$Si_{16}H_{32}$	8.643	3.790	3.790	48
$Si_{32}H_{54}$	8.562	8.562	8.564	86
$Si_{64}H_{84}$	8.480	8.480	11.393	248
$Si_{216}H_{198}$	13.690	13.690	19	414

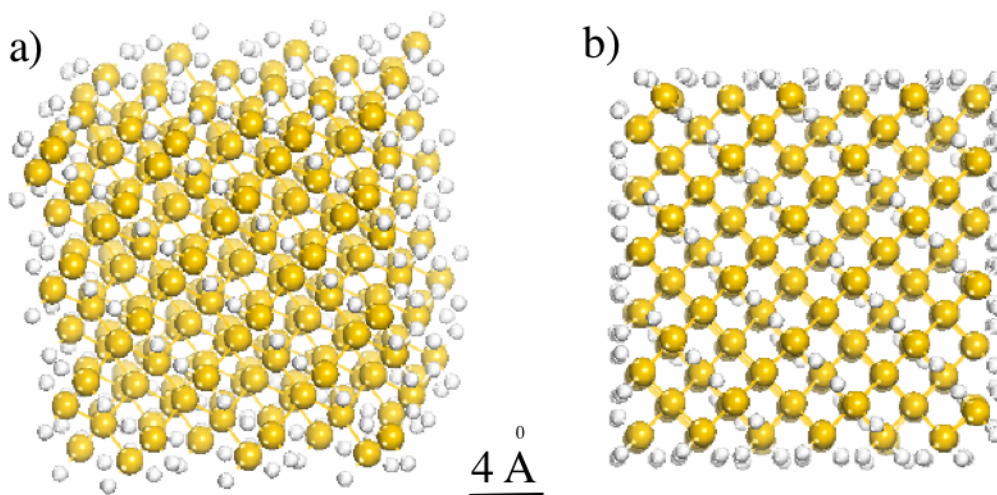


Figure 2.6: Cubic $Si_{216}H_{198}$ a) 3D view of cubic shape, b) top view.

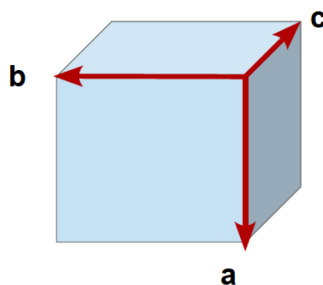


Figure 2.7: Illustration of dimensional measurements of cubic SiNCs.

2.5.3 Rectangular SiNCs

The biggest rectangular SiNC (see Figure 2.11) is built in the following dimensions (number of unit cell in all direction): $A = (5,0,0)$ $B = (0,1,0)$ $C = (0,0,4)$. Then for building the other smallest sized rectangular shapes, the number of unit cells in the Z-direction only is changed to $(0,0,3)$, $(0,0,2)$, or $(0,0,1)$. In this way, one length is changed and the other dimensions are constant. In addition to using hydrogen passivation, four other rectangular SiNCs are built by replacing every hydrogen atom by a hydroxyl group following the same procedure as in the literature to form an oxide shell (see Figure 2.9)[21].

Table 2.2: Difference between rectangular SiNCs in width.

Structure	Width Å	total number of atoms
$Si_{40}H_{74}$	5.917	114
$Si_{80}H_{120}$	8.586	200
$Si_{120}H_{166}$	13.844	286
$Si_{160}H_{212}$	19.198	372

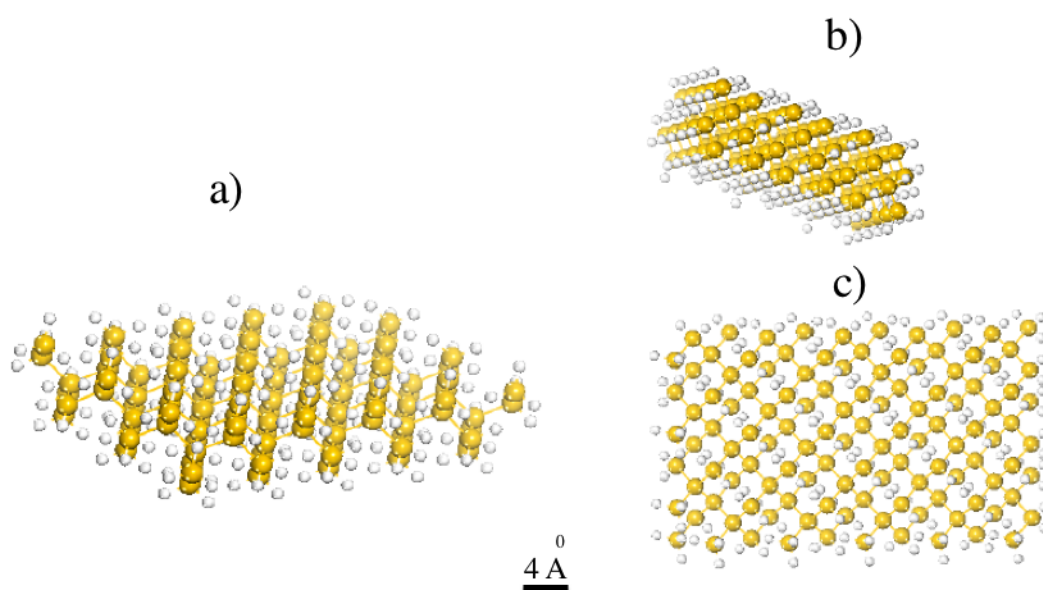


Figure 2.8: Rectangular $Si_{120}H_{166}$ a) 3D view of a rectangular shape, b) side view and c) top view.

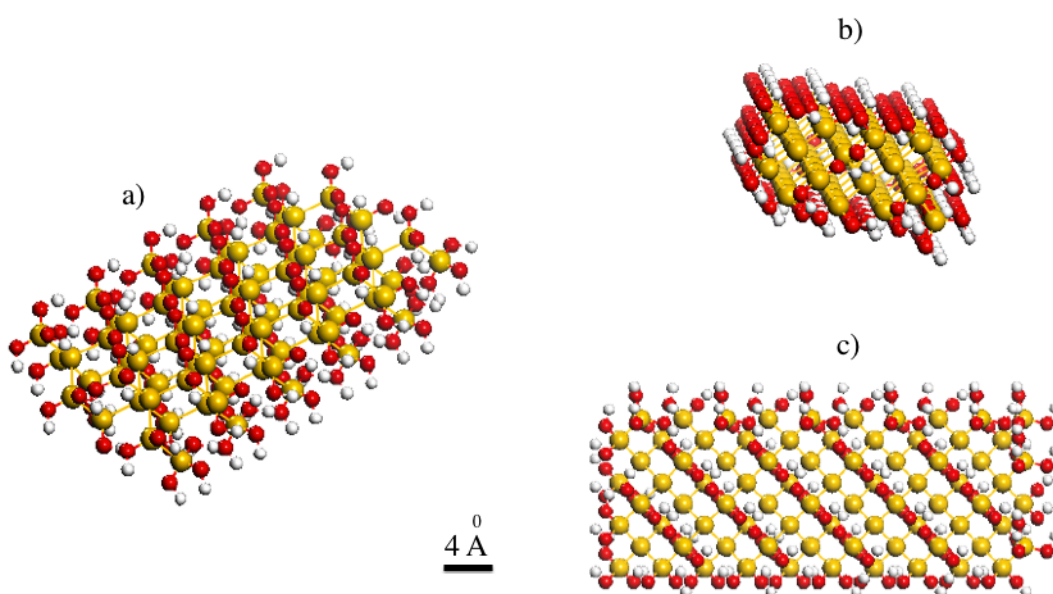


Figure 2.9: Rectangular $Si_{80}(OH)_{120}$ a) 3D view of a rectangular shape, b) side view and c) top view.

2.5.4 Ellipsoidal SiNCs

Following the same procedure for building rectangular shapes, ellipsoidal SiNCs are built in which the number of unit cells for the biggest structure in all directions are $A = (2,0,0)$ $B = (0,2,0)$ and $C = (0,0,7)$. Two lengths are fixed which have the sizes of $a = 8.586 \text{ \AA}$, $b = 8.586 \text{ \AA}$ while the third is c (height) changes (see Table 2.3).

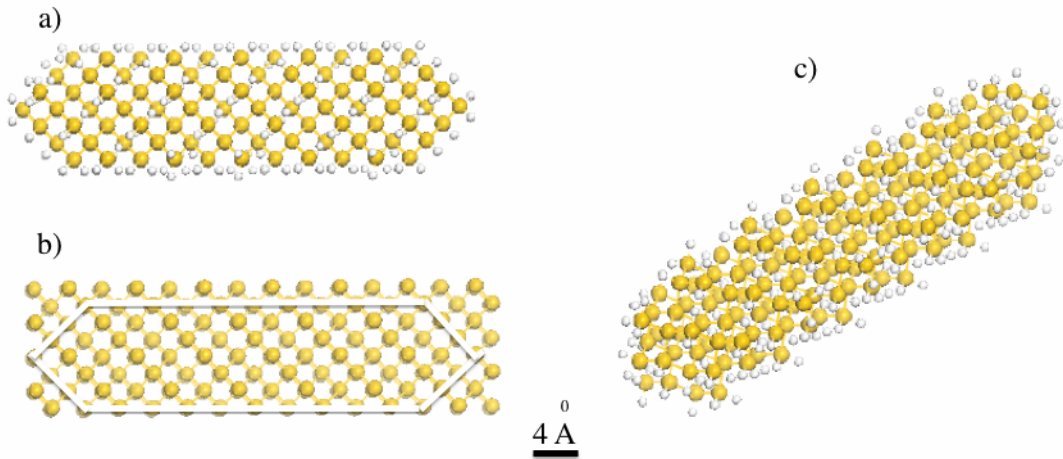


Figure 2.10: Constructing ellipsoidal SiNCs a) cutting an ellipsoidal by removing the outer Si atoms of the shape b) after hydrogen passivation c) 3D view of $Si_{166}H_{172}$ shape

Table 2.3: Difference between all ellipsoidal SiNCs in height.

Structure	Height \AA	total number of atoms
$Si_{50}H_{65}$	10.860	106
$Si_{88}H_{100}$	19.198	188
$Si_{139}H_{146}$	29.988	285
$Si_{166}H_{172}$	35.399	338

2.5.5 Flat Disk SiNCs

Starting from the largest structure where the number of unit cells in all directions are $A = (2,0,0)$, $B = (0,4,0)$ and $C = (0,0,4)$, the number of unit cells is chosen in a way that the number of unit cells is the same in Y and Z-directions to build circular disks i.e., the average of B and C is the diameter which is variable (see Table 2.4). However,

achieving a circular shape is not easy especially for a small number of atoms. As the structure becomes larger, the circular shape becomes more visible.

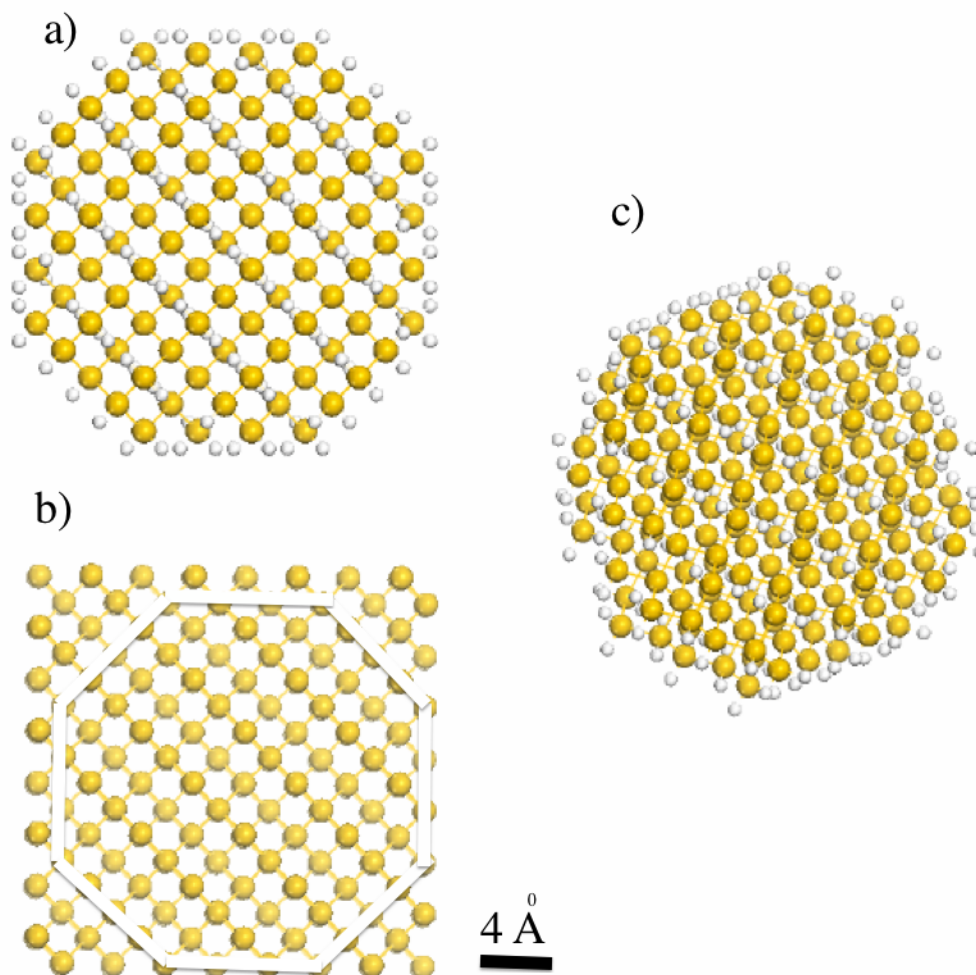


Figure 2.11: Constructing a flat disk a) cutting an ellipsoidal by removing the outer Si atoms of the shape b) after hydrogen passivation c) 3D view of $Si_{186}H_{156}$ shape.

Table 2.4: Difference between all flat shapes of SiNCs in diameter.

Structure	Diameter \AA	total number of atoms
$Si_{30}H_{38}$	8.8625	68
$Si_{80}H_{82}$	12.513	142
$Si_{125}H_{118}$	16.33	243
$Si_{186}H_{156}$	19.198	342

2.5.6 Computational Method

All constructed SiNCs were modeled using VAMP, which is a semi-empirical method built in to Materials Studio [72]. VAMP has two types of Hamiltonians that can be employed: neglect of diatomic differential overlap (NDDO) or Zerners intermediate neglect of differential overlap (ZINDO). The NDDO Hamiltonian is well-suited for performing geometry optimization and calculating properties such as heat of formation while ZINDO is typically used for spectroscopy calculations. NDDO has several modified versions of it including MNDO, AM1, PM3 and *AM1**. These Hamiltonians have been developed successively to cover or correct some errors such as heat of formation and hydrogen bonding (see section 2.2). VAMP offers the possibility of modeling a structure up to 400 atoms or larger for more powerful hardware and software [72]. However, validation is necessary before one should employ VAMP in an unknown structure such as SiNCs. Thus, some of the NDDO Hamiltonians were employed on the well-known organic molecule benzene (Figure 2.12) to predict its ground and excited state properties.

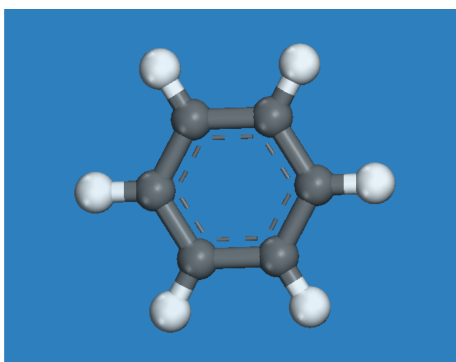


Figure 2.12: Benzene molecule, C_6H_6

2.5.7 VAMP Tests on Benzene

Ground State

AM1, PM3 and *AM1** were employed to predict bond lengths and heat of formation. Optimization with *AM1** gave almost the same result as AM1 since *AM1** is a modified version of AM1 with s, p, and d orbitals. Table 2.5 shows an example of the calculated properties of a benzene molecule. PM3 performed well in predicting the heat of formation compared to AM1. On the other hand, AM1 performed well in predicting the bond length C-C.

Table 2.5: Experimental and theoretical data of benzene molecule.

Method or data	AM1	PM3	PM3. Ref [76]	Ref [77]	Ref.[78]
Heat of formation Kcal/mol	22.050	23.482	23	24±0.2	-
C-C in A^0	1.395036	1.39110	-	-	1.397± 0.001
C-H in A^0	1.09965	1.0947	-	-	1.084 ± 0.006
HOMO in (eV)	- 9.653	- 9.751	- 9.24	-	-
LUMO in (eV)	- 0.555	- 0.396	- 0.40	-	-

Excited State

Excited state properties were investigated by employing single energy calculations using AM1 Hamiltonian with one of the configuration interaction methods built in to VAMP. CI methods vary according to correlation schemes that can be applied as mentioned in section 2.3. These correlation methods were employed extensively in benzene to gain some confidence in these methods before employing them in SiNCs. Before performing the energy calculation, one must specify the number of orbitals to be used. The number of orbitals defines the occupied and unoccupied orbitals that can be used when constructing the electronic wave function. This number can vary according to the method applied. Both FCI and CISD have a limited number of orbitals that can be used and this number cannot exceed 8 and 11 for FCI and CISD, respectively in the VAMP program model [72]. In the CIS method the maximum number depends on the size of the molecule: the maximum number of orbitals can be estimated according to the following:

$$\text{Max\#of orbitals} = \text{\#of occupied orbitals} + \text{\#of unoccupied orbitals} \quad (2.20)$$

The influence of the number of orbitals has been investigated in the literature using some of the CI methods. According to Grimme (1992), who studied the ground and excited state of some organic molecules e.g., perylene [79], using an appropriate number of orbitals can be critical for predicting experimental excited state energies. Similar investigation of the influence of total orbital number has been performed by Beck and Grummt for studying first-order hyperpolarizabilities using VAMP/AM1 and PM3 for some organic molecules[80]. These considerations were taken in account

along with factors such as the number of orbitals that can be applied to a particular CI method within VAMP, and the time of calculation and agreement with experimental data. The number of orbitals and calculation time were found to be correlated and were dependent on the method employed. FCI and CISD start to become costly when the number of orbitals approaches 8 and 11 for FCI and CISD, respectively. The cost of these calculations approached 64 hours with almost no enhancement of the results. On the other hand, for CIS increasing the number of orbitals did not lead to an increase of the calculation time by a large factor. The benzene molecule is known to have two main absorption bands along with a third band or some other experimental three bands (Table 2.6) [81,82].

Table 2.6: Optical absorption bands of benzene from experiment.

Absorption Bands	Ref[82]	Ref. [81]
1 st Max absorption	189.5 nm	185 nm
2 nd Max absorption	-	120 nm
3 rd Max absorption	210 nm	215 nm

To investigate the influence of the number of orbitals in calculating the optical properties of benzene both AM1 and PM3 are employed along with the CI methods. The best result obtained for both AM1 and PM3 in spite of excitation energies, wavelength and oscillator strength are for 6 full, for 8 CISD and 8 CIS orbitals for AM1 and 10 orbitals for PM3. Table 2.7 summarizes the obtained value for excitation energies using the above mentioned orbital numbers.

Table 2.7: Excitation energies of benzene calculated by AM1 and PM3 that correspond to the major absorption bands.

	AM1/ 6 full	AM1/ 8 CISD	AM1/ 8 CIS	experiment[83]
Energies (eV)	6.044	6.44	6.26	6.83-6.93
Energies (eV)	11.82	10.89	10.28	-
Energies (eV)	-	-	-	6.09
	PM3/ 6 full	PM3/ 8 CISD	PM3/ 10 CIS	experiment [83]
Energies (eV)	6.027	6.41	6.25	6.83-6.93
Energies (eV)	11.92	10.32	9.76	-
Energies (eV)	-	-	-	6.09

Figure 2.13 shows the calculated UV-vis spectra of benzene using the same number of orbitals as in Table 2.7. The UV-vis spectra in Figure 2.13 represents the best agreement with experimental data in regard to oscillator strength and absorption peaks.

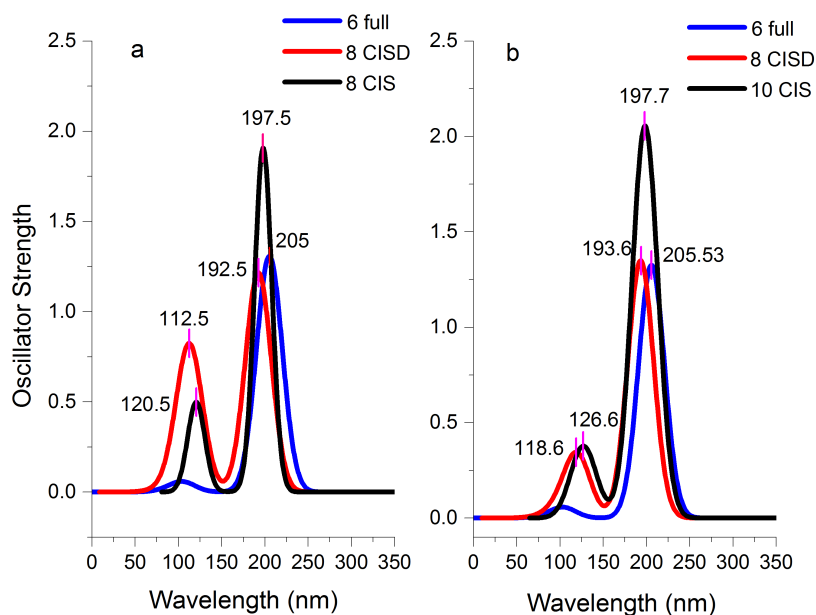


Figure 2.13: Calculated UV-vis spectra of benzene with a) AM1 and b) PM3)

The results indicate that the performance of the CI methods with AM1, PM3 are satisfactory in reproducing the experimental data.

2.6 Results and Discussion

Sixteen SiNCs of different shapes were modeled to study their electronic and optical properties. All the modeling was performed using the AM1 Hamiltonian.

2.6.1 Geometry Optimization

The first set of modeling was performed on cubic SiNCs by doing a geometry optimization then energy calculations. To find the minimum energy of cubic SiNCs, geometry optimization was performed using some criteria as recommended in the literature e.g., RMS force and gradient norm (Gnorm) [67]. To obtain a minimum,

the RMS force and gradient norm should be less than their threshold values before optimization was assigned before running the optimization calculation. The achieved convergence of these values is shown in table 2.8 and table 2.9.

Table 2.8: Convergence criteria for $Si_{16}H_{32}$ for various trials.

Quality	Before optimization	Before optimization	After optimization	After optimization
RMS force	Gnorm	RMS force	Gnorm	RMS force
Coarse	1	1	0.0768	0.922
Medium	0.2	0.4	0.032	0.396
Fine	0.1	0.1	0.0065	0.079
Customized	0.01	0.01	0.0007	0.009

Table 2.9: Convergence criteria for $Si_{32}H_{54}$ for various trial.

Quality	Before optimization	Before optimization	After optimization	After optimization
RMS force	Gnorm	RMS force	Gnorm	RMS force
Coarse	1	1	0.06055	0.972
Medium	0.2	0.4	0.0245	0.39
Fine	0.1	0.1	0.0059	0.0958
Customized	0.01	0.01	0.000602	0.00966

In both structures, the achieved Gnorm is about 0.009 kcal/mol/Å which is below the recommended value of 0.05 kcal/mol/Å [84–86]. Optimized cubic SiNC structures were extremely distorted, in particular the smallest ones. The distortions are more clearly seen in the outer most bonds between Si-H. Figure 2.14 and Figure 2.15 show pictures of $Si_{32}H_{54}$ and $Si_{64}H_{84}$ before and after geometry optimization.

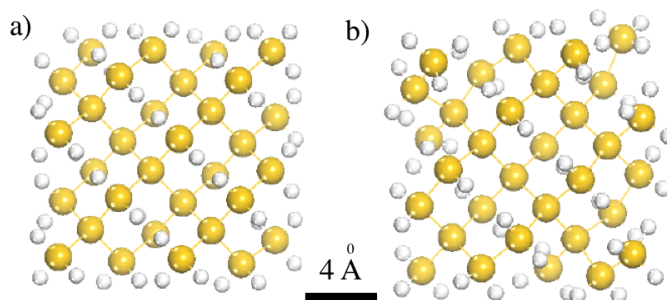


Figure 2.14: Cubic $\text{Si}_{32}\text{H}_{54}$ a) constructed shape and b) optimized.

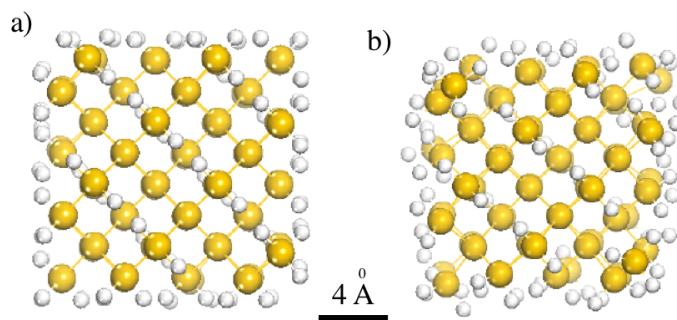


Figure 2.15: Cubic $\text{Si}_{64}\text{H}_{84}$ a) constructed shape b) after optimization

Cartesian coordinates for $\text{Si}_{35}\text{H}_{36}$ and $\text{Si}_{87}\text{H}_{76}$ were also imported from the literature and plotted in Materials studio [74]. The imported SiNCs have T_d symmetry and the number of hydrogen that terminates the SiNCs is either one or two hydrogen atoms. After optimizing these structure by AM1, no distortion was observed (see Figure 2.16). The input values of the bond length for imported structures are close to the experimental values of 2.35 Å and 1.46 Å, for Si-Si and Si-H, respectively [87]. By comparing the average values of all the structures in table 2.10, it seen that the imported structures have bond length very close to the experimental data whereas the constructed cubic SiNC with an average bond length close to experimental values is $\text{Si}_{64}\text{H}_{84}$.

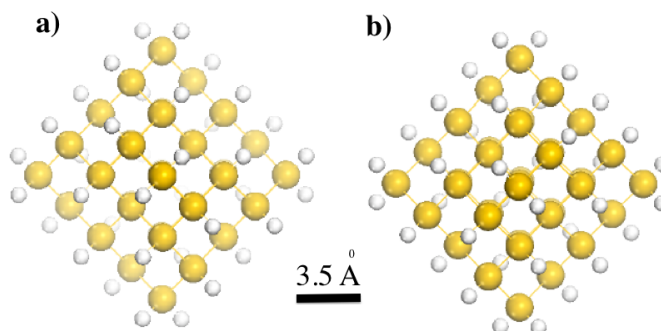


Figure 2.16: $\text{Si}_{35}\text{H}_{36}$ with average diameter of 1.704 nm a) before and b) after optimization [74].

Table 2.10: Difference between cubic SiNCs and imported structures in bond length.

Structure	Si-Si bond	$\text{Si}_{32}\text{H}_{54}$	$\text{Si}_{64}\text{H}_{84}$	$\text{Si}_{35}\text{H}_{36}$	$\text{Si}_{87}\text{H}_{76}$
Before optimization	Largest	3.999	3.897	4.528	4.539
	Smallest	2.338	2.338	2.351	2.350
	Average	2.923	2.762	2.595	2.436
After optimization	Largest	3.995	3.997	4.539	4.476
	Smallest	2.337	2.338	2.334	2.337
	Average	2.952	2.784	2.551	2.428

2.6.2 HOMO-LUMO Gap

The behaviour of the calculated HOMO-LUMO gap is shown in Table 2.11. The gap decreases as the size of nanocrystals increases.

Table 2.11: Electronic properties of SiNCs and imported structures using AM1.

Structure	HOMO (eV)	LUMO (eV)	gap (eV)
$\text{Si}_{16}\text{H}_{32}$	-9.723	-1.539	8.184
$\text{Si}_{32}\text{H}_{54}$	-9.409	-1.755	7.654
$\text{Si}_{35}\text{H}_{36}$	-9.515	-1.816	7.699
$\text{Si}_{64}\text{H}_{84}$	-9.091	-1.959	7.132
$\text{Si}_{87}\text{H}_{76}$	-9.176	-2.114	7.062
$\text{Si}_{216}\text{H}_{198}$	-8.792	-2.161	6.631

2.6.3 Modeling Different Shapes

Investigation into the influence confinement and shape of nanoparticles has been studied in both experimental and theoretical research. Understanding the influences of shape on properties is important for utilizing Si particles for optoelectronic devices. Particle shapes including disks, spheres, ellipsoids, and rods, have been synthesized. In some case the obtained shape is because of the strain imposed by SiO and blocking the growth in one direction [88]. Some theoretical investigations have also been conducted to understand the influence of the degree of confinement, shape, and coupling between Si particles. It has been demonstrated that Si spherical clusters have the widest gap, then nanowire, and followed by the Si slab [89]. For coupling between particles of ellipsoidal shapes, it has been shown that coupling is reduced for non-spherical particles because the ground state wave function is located at the center of the particle. Here, a variety of SiNCs shapes that differ in sizes are studied in order to understand the behavior of the HOMO, LUMO, HOMO-LUMO gaps and their optical properties.

For rectangular SiNCs, the model structures show almost the same symmetry, C_1 except for $\text{Si}_{40}\text{H}_{74}$ which shows C_s symmetry (see Table 2.12). Also, these structures show a consistent increase in the HOMO and a decrease in LUMO as the size of rectangular SiNCs increases. Thus, the HOMO-LUMO gap decreases with increasing the SiNC size following the quantum confinement model observed in low dimensions. The highest value assigned to the HOMO-LUMO gap is for $\text{Si}_{40}\text{H}_{74}$.

Table 2.12: HOMO-LUMO gap of rectangular SiNCs.

	$\text{Si}_{40}\text{H}_{74}$	$\text{Si}_{80}\text{H}_{120}$	$\text{Si}_{120}\text{H}_{166}$	$\text{Si}_{160}\text{H}_{212}$
Symmetry	C_s	C_1	C_1	C_1
HOMO (eV)	-9.735	-9.18	-8.999	-8.925
LUMO (eV)	-1.516	-1.732	-1.778	-1.79
HOMO-LUMO gap (eV)	8.219	7.448	7.221	7.135

For ellipsoidal SiNCs, the symmetry of our model structures were all C_1 except in the smallest one, $\text{Si}_{50}\text{H}_{65}$, being D_2 . Here, the decrease in HOMO is not as significant with increasing the size compared to rectangular SiNCs. The HOMO-LUMO gap of ellipsoidal $\text{Si}_{50}\text{H}_{56}$ is 0.816 eV lower than rectangular $\text{Si}_{40}\text{H}_{74}$ even though the difference in the number of atoms is just 8. The difference in the HOMO-LUMO gap

could be due to the difference in the number of hydrogen atoms passivated in addition to the particle shape.

Table 2.13: HOMO-LUMO gap of ellipsoidal SiNCs.

	Si ₅₀ H ₅₆	Si ₈₈ H ₁₀₀	Si ₁₃₉ H ₁₄₆	Si ₁₆₆ H ₁₇₂
Symmetry	D ₂	C ₁	C ₁	C ₁
HOMO (eV)	-9.29	-9.034	-9.024	-8.997
LUMO (eV)	-1.887	-1.928	-1.982	-1.976
HOMO-LUMO gap (eV)	7.403	7.106	7.042	7.021

Similar results were obtained for flat disk SiNCs, three of them with C₁ symmetry and the largest with C_{2v} symmetry. Actually, the gap for Si₃₀H₃₈ is similar to the cubic Si₃₂H₅₄ gap with a difference of about 0.02 eV. However, the difference becomes larger when comparing flat disk SiNCs with rectangular SiNCs that have a comparable number of Si atoms. For example, rectangular Si₈₀H₁₂₀ has a gap of 7.448 eV while flat disk Si₈₀H₈₂ has a gap of 7.089 eV. A similar behaviour is observed for other structures that have a comparable number of Si atoms (see Figure 2.17).

For oxidized SiNCs, the HOMO-LUMO gaps still follows the QC model; the HOMO-LUMO gap became smaller as the size of the particle became larger (see Table 2.15). These Oxidized SiNCs have the same shape as rectangular SiNCs with hydrogen passivation, but every hydrogen atom is replaced by a hydroxyl group. The gaps of the oxidized SiNCs drops by more than 1.7 eV for the smallest sized structure and more than 2.5 eV for the largest oxidized shape compared to rectangular SiNCs passivated with hydrogen. The observation of the HOMO-LUMO gap decrease has been observed with other methods such as DFT [21]. For example, a Si₃₅(OH)₃₆ gap dropped by 2 eV while a larger structure Si₆₆(OH)₆₄ dropped by 1.5 eV.

To visualize the difference between these shapes and the difference of passivation treatment in the HOMO-LUMO gaps Figure 2.17 shows clearly the size-dependence of the HOMO-LUMO gap. Rectangular SiNCs, have a larger size gap than the ellipsoidal SiNCs and oxidized SiNCs. The HOMO-LUMO gap for rectangular shapes is always higher even though their sizes are larger than cubic SiNCs. A similar observation is obtained by comparing rectangular with other shapes. The possible explanations of this behaviour could be due to the sharp edge of the rectangular shape, or the surface

passivation differs from the other shapes. For oxidized SiNCs, it is clearly seen that the HOMO-LUMO gap drops by more than 2 eV compared to hydrogen passivation of the same shapes. Additionally, Figure 2.18 shows the difference in energy levels of SiNCs with hydrogen passivation.

Table 2.14: HOMO-LUMO gap of flat disk SiNCs.

	Si ₃₀ H ₃₈	Si ₈₀ H ₈₂	Si ₁₂₅ H ₁₁₈	Si ₁₈₆ H ₁₅₆
Symmetry	C ₁	C ₁	C ₁	C _{2v}
HOMO (eV)	-9.46	-9.085	-8.923	-8.843
LUMO (eV)	-1.786	-1.1.996	-2.043	-2.105
HOMO-LUMO gap (eV)	7.674	7.089	6.88	6.738

Table 2.15: HOMO-LUMO gap of oxidized SiNCs.

	Si ₄₀ (OH) ₇₄	Si ₈₀ (OH) ₁₂₀	Si ₁₂₀ (OH) ₁₆₆	Si ₁₆₀ (OH) ₂₁₂
Symmetry	C ₁	C ₁	C ₁	C _{2v}
HOMO (eV)	-7.195	- 6.642	- 6.328	- 6.102
LUMO (eV)	- 0.683	- 1.01	-1.293	- 1.551
HOMO-LUMO gap (eV)	6.512	5.632	5.035	4.551

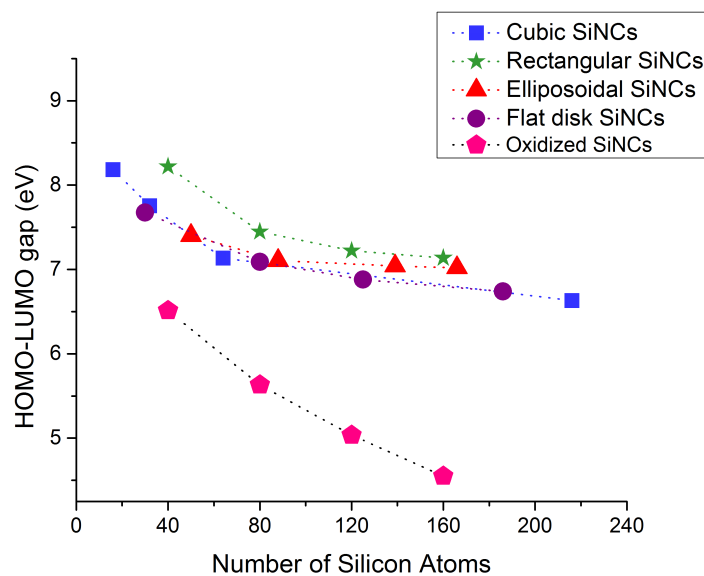


Figure 2.17: Size dependent HOMO-LUMO gaps for all cubic, rectangular, ellipsoidal, and flat disk SiNCs modelled for this work.

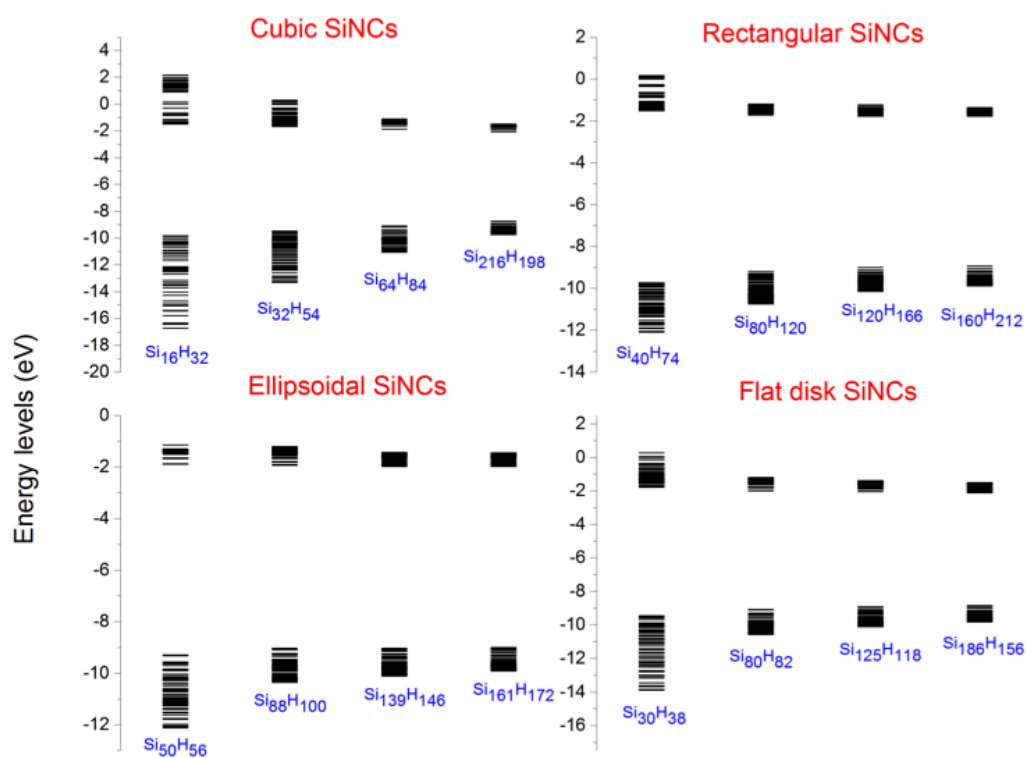


Figure 2.18: Energy levels of SiNCs of different shapes.

2.6.4 Raman Spectroscopy

SiNCs Raman spectra have been calculated for some structures to study their structural properties. Raman spectra were calculated for cubic SiNCs using a single energy calculation AM1 with or without CI methods. Raman spectra of $\text{Si}_{64}\text{H}_{84}$ and $\text{Si}_{216}\text{H}_{84}$ show a strong peak at 454.5 cm^{-1} and 514 cm^{-1} which support the observation of a Raman shift and asymmetric broadening in small Si nanocrystals (See Figure 2.19 and 2.20) [90, 91], compared to bulk silicon.

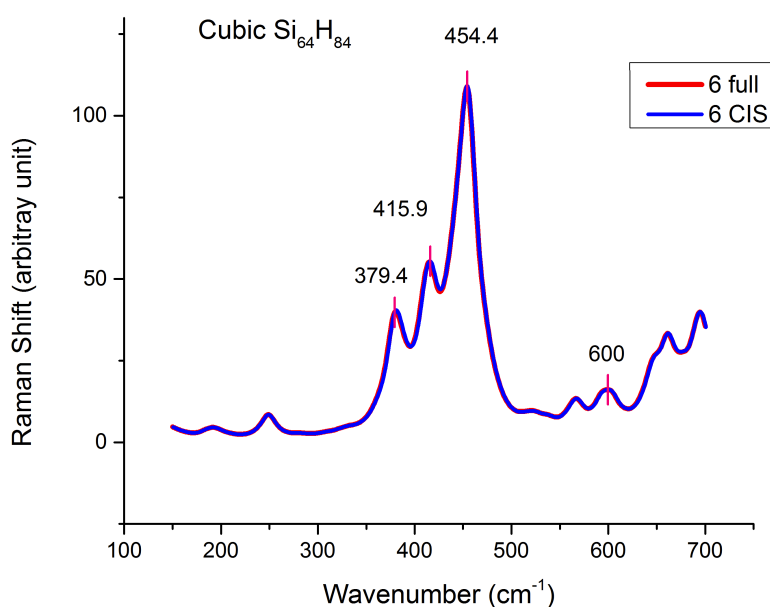


Figure 2.19: Modeled Raman spectra of cubic $\text{Si}_{64}\text{H}_{84}$ with AM1 single energy calculation.

2.7 Discussion

Semi-empirical methods have shown very good performance in predicting ground and excited state properties for organic molecules. Optimizing organic molecules by semi-empirical methods led to finding an equilibrium structure of the molecule under study. When a single energy calculation is performed to study the excited state properties of benzene, the results showed good agreement with the experiment. When SiNCs are modelled using AM1, the HOMO-LUMO gaps increase with decreasing the particle size.

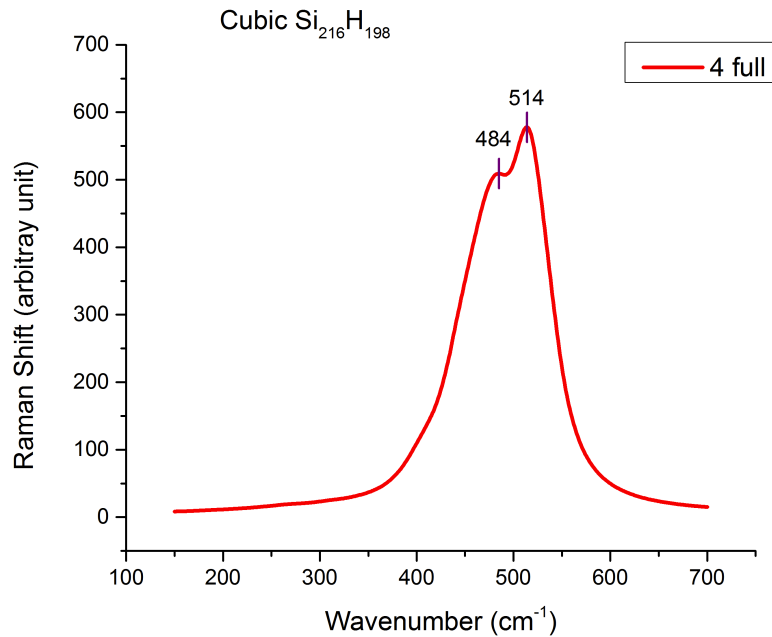


Figure 2.20: Modeled Raman spectra of cubic $\text{Si}_{216}\text{H}_{198}$ with an AM1 single energy calculation.

Observation of the unified curve of HOMO-LUMO gaps with different shapes and sizes agrees with the theoretical study by Wang et al.(1994) for Si particle shapes including sphere, cubic and rectangular passivated with hydrogen of more than 1000 atoms [92]. However, in this investigation the authors used the diameter as an effective way to define the size of the particle in which every particle was treated as a sphere that has the same density and same number of atoms as bulk silicon using the following:

$$d(N) = \left(\frac{3N}{4\pi\rho} \right)^{\frac{1}{3}} = 3.3685N^{\frac{1}{3}} \quad (2.21)$$

There are some theoretical and experimental studies that show that different shapes show different properties and different confinement according to changes in either width or length of shape [93, 94]. One experimental study showed that CdSe quantum rods show a different emission peak shift according to their sizes and the changes in either their widths or lengths.

Additionally, the calculated Raman spectra of cubic SiNCs show that the Raman shift is due to the reduced size of the particle. The results of this chapter indicate that Si particle properties are dependent upon both shape, size, and surface properties. In the next chapter, a wet colloidal grinding method is employed to synthesize Si nanoparticles in solution.

Chapter 3

Experimental Results

3.1 Introduction

Nanoparticles are generally synthesized via two main approaches: bottom-up or top-down[95]. In the bottom-up approach, the synthesis method typically involves a chemical reaction of suitable precursors in which different forms of nanoparticles can be synthesized. For example, for nanoparticles in solution, the synthesis method involves seeding, growth, and capping of the nanoparticles. The main challenge of this method is to control the size distribution to less than 5% [95]. On the other hand, in the top-down approach, the material is usually broken down into small particles via an energy source e.g., ion implantation or mechanical milling. High-energy mill equipment differs in its capacity, milling efficiency, number of vials, natural motion of the vial and the use of a cooling or a heating system [96]. Examples of this equipment are jet, planetary ball, and attritor millings [97]. Jet mills have some advantages over the other high-energy ball mill equipment; for example, no contamination was observed because the collision between particles was forced by high pressure gas and so very good control of the size and distribution of the particles could be achieved. Even though a jet mill is considered good milling equipment, it has some disadvantages such as very high losses of the raw material and being a very expensive system to control the size of particles. Planetary ball and attritor milling lead to size reduction via the collision between balls and particles, and the milling can be performed with dry or wet media. In planetary and attritor milling, there is no loss of the raw material and the equipment is not costly compared to the jet mill. However, the main disadvantage of them is the possibility of contamination [97]. In general, high-energy mill equipment

can be utilized for two types of milling: mechanical alloying or mechanical milling[96]. In the former, a mixture powder of two materials is milled to form an alloy and to reduce the size of the particles. In the latter, an alloy powder or any powder is milled to reduce the size of the particles. Mechanical milling has been performed with wet or dry media for materials such as silicon carbide (SiC), barium titanate (BaTiO₃), lead titanate (PbTiO₃), alumina (Al₂O₃), and Si [97–100]. In our investigation, we perform wet colloidal grinding for silicon powder using a planetary ball mill RETSCH PM200 since the ball mill has a range of speeds from low to high without losing its high impact between the ball and particles.

3.2 Planetary Ball Milling

The planetary ball mill PM200 consists of two-jar stations mounted on a support disc that rotates in opposite directions (see Figure 3.1) [98]. The difference of the rotational direction causes superimposition of the centrifugal forces that originate from the rotation of the jars and the disc. The superimposition of centrifugal forces causes the beads to move at a very high speed in the same direction of the jar wall rotation but at a lower speed. As a result of the difference in speed between the beads and the jar wall, there is an increase in the collision and the frictional effects between the beads and the sample as well. When the rotational speed is further increased, the Coriolis force displaces the beads from the jar wall into the opposite side of the wall, which highly impacts the sample because the beads can move freely inside the jar and act against the sample, which produces high impact energy. As the result of these forces, the sample is milled to a fine degree of size reduction.

Many parameters influence the efficiency of grinding (see Figure 3.2) [101]. Some researchers claim that the initial size of the raw material is not critical since the particle size can be reduced to sub-micron after few minutes of grinding i.e., the decrease of particle sizes takes the form of exponential decay [98]. This means the grinding time is more important than the initial size of the particles, and further decreases in the particle size can be achieved via a longer grinding time, but at a slow rate. For other parameters such as the balls to powder weight ratio and extent of filling, these values vary in the literature. Balls to powder weight ratio values is as high as 1:1, 10:1, 20:1 or low as 200:1[98,101]. Additionally, the speed of the mill has a high impact on the material to be milled since higher speed means higher impact and

collision forces. However, an increase in the speed of rotation may result in an increase of the temperature. Contamination is possible from the material of the vial, balls and the atmosphere. A study for SiC milled for (0.5, 2, 4 and 6 hours, speed 300 rpm, IPA) in a stainless steel jar using zirconia balls stabilized with ceria shown that the produced product was contaminated with ZrO_2 and the percentage of contamination increased linearly with time [97]. Another study, showed an increase in the time of milling did not result in contamination but instead led to a decreased particle size as well as an increase in the stability of the colloidal solution e.g., $BaTiO_3$ milled up to 20 h.[98]. Therefore, choosing the optimal parameters is highly dependent on the materials being milled.

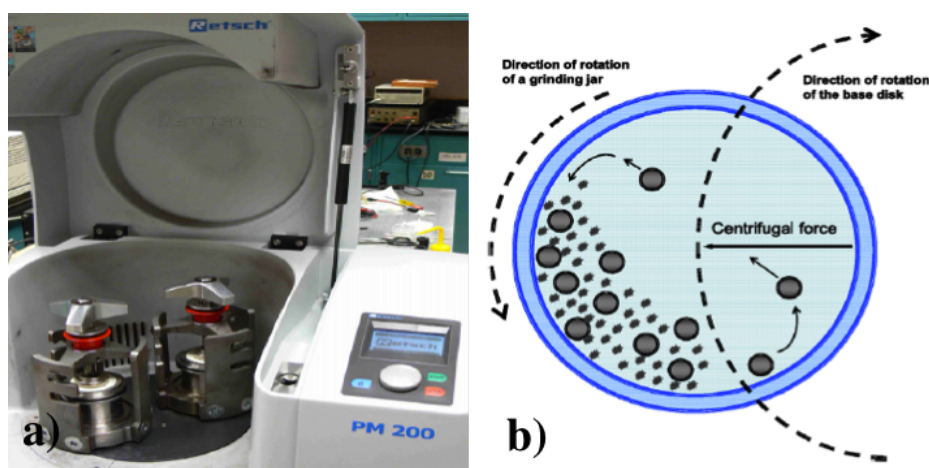


Figure 3.1: a) Planetary ball mill RETSCH PM200 and b) Motion of grinding spheres inside the vial. After [98].

3.3 Colloidal Grinding

3.3.1 Experimental Details

Colloidal silicon particles were prepared via wet grinding using the planetary ball mill PM 200 manufactured by Retsch and available at the Earth and Ocean Sciences Department at the University of Victoria.

Silicon powder 99.999% purity consisting of 10-50 μm particles was purchased from Alfa Aesar. The grinding media or solvent was isopropyl alcohol (IPA). The 50 mL grinding vessel and 2 mm diameter beads were made of ZrO_2 . The jar was filled with beads, Si powder and, finally, IPA. Then the vessel was sealed with its lid

Table 3.1: Material data and grinding parameters for all prepared trials.

Trial number	1	4	7	8	9	10	11
Si powder (g)	4.4823	4.4824	4.4814	4.4826	4.4883	4.4843	4.4813
IPA (ml)	8	8	8	8	8	8	1 6
Beads (g)	89.6749	89.6749	88.7662	88.7662	89.6749	88.7662	89.6749
Speed (rpm)	500	500	250	250	400	500	500
Time (h)	0.5	1.5	1	1.5	15	8	4
Volume (ml)	130	190	150	146	200	200	200

and tightly covered with parafilm to prevent spilling. The percentage of filling and weight ratios of beads to silicon powder were chosen to be approximately 50% and 20:1 as those were typical values in the literature[98]. Table 3.1 lists grinding trial parameters used.

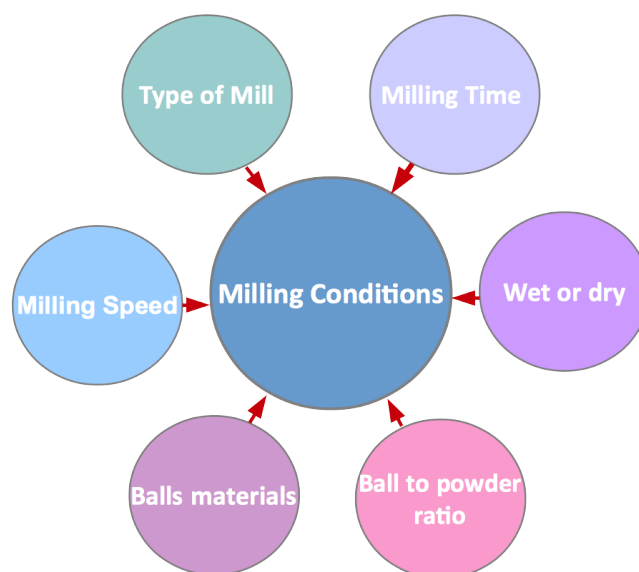


Figure 3.2: Milling conditions, reproduced from ref [101].

Initially the grinding trial was set for a short time, then grinding time was gradu-

ally increased; for the speed, three sets of speed were chosen: low (250 rpm), medium (400 rpm) and high (500 rpm). After grinding was finished, the grinding jar was kept clamped in the grinding machine for a period of time which depended on the time of grinding for that trial since a higher speed and long grinding time may result in increased temperature and also in pressure accumulation from evaporation of the liquid. The colloidal particles were extracted from the jar by using circular mesh with smaller openings than the size of beads. After extraction, the colloidal solution was transferred into small vials with their own lids for easy processing and also covered with parafilm to avoid evaporation. Figure 3.3 is a simple illustration of the extraction process.

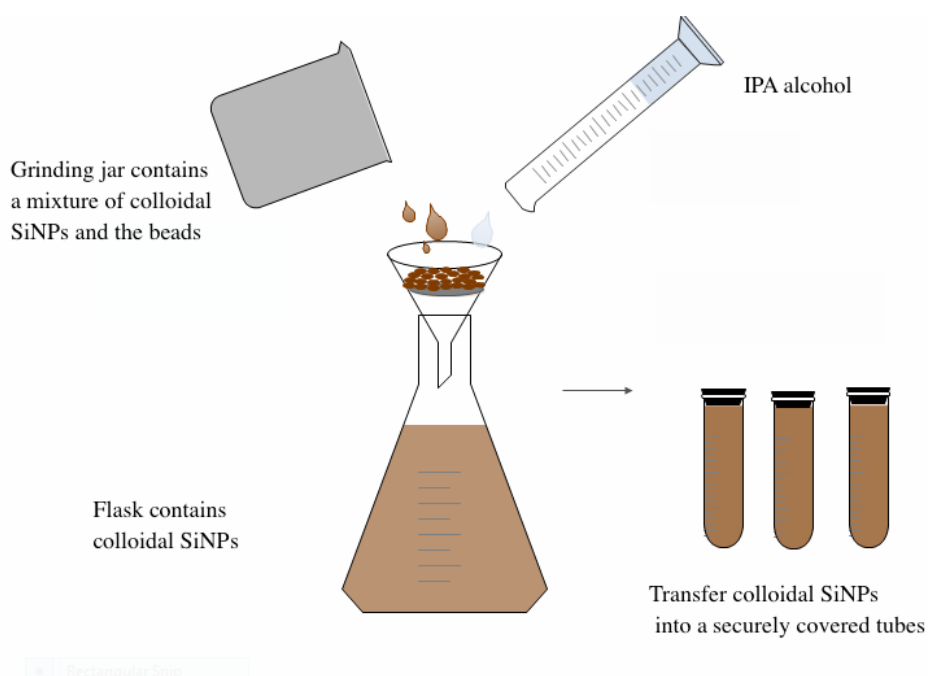


Figure 3.3: Extraction process of colloidal particles

3.3.2 Purification

Most synthesis methods for nanoparticles (NPs) have the problem of polydispersity i.e., particles of different sizes and shapes[95]. In order to utilize these particles in a particular application a uniform size and shape distribution is desirable. To narrow the size distribution of NPs, nanoscale separation or purification techniques are necessary [102]. Centrifugation is a very effective separation technique that has been widely utilized in colloidal science and molecular biology. Centrifugal techniques

can be used to separate particles less than $1\ \mu\text{m}$ and for less than $0.1\ \mu\text{m}$ higher rotational speed is required. According to Stokes' Law, the smaller the particle, the higher speed required [102,103].

$$v_t = \frac{\omega^2 r (\rho_p - \rho_l) d_p^2}{18\eta} \quad (3.1)$$

$$t_t = \frac{\ln\left(\frac{r_{max}}{r_{min}}\right)}{v_t} \quad (3.2)$$

Where v_t is the terminal velocity or sedimentation rate, ω is the angular velocity of the rotor, ρ_p and ρ_l are the density of the particles and solution, respectively. d_p is the diameter of particle assuming that the particle has a spherical shape, η is the viscosity of the solution, r_{max} and r_{min} are the maximum and minimum rotor radii, respectively, and t_t is the required time for sedimentation for particles with a defined diameter.

In order to obtain efficient separation, there should be a variation between the particle and the liquid densities. If there is no difference between them, no separation occurs. Here, our colloidal solution satisfies Stokes' Law because there is a difference between the Si particle and IPA density and the viscosity is not high. As a result, sedimentation is possible. We applied a variation of speeds and times from low to high (see Table 3.2).

Table 3.2: Centrifugation parameters.

Name	Speed (rpm) & time (min)	Name	Speed (rpm) & time (min)
X-1	3000 & 50	Z-A	1000 & 7
Y-2	3000 & 12	Z-B	1000 & 30
X-3	7000 & 8	Z-C	3000 & 300
Y-4	7000 & 55	Z-D	3000 & 3
Y-5	10000 & 25	Z-E	7000 & 8
Y-6	10000 & 99	Z-F	7000 & 0.5

Where : X refers to (trial 1, trial 4, trial 7, trial 8), Y refers to (trial 4 , trial 8 ,

trial 9 , trial 10 , trial 11) and Z refers to (trial 4, trial 8).

To apply these parameters, we used an Eppendorf 5415D microcentrifuge machine and 1.5 ml centrifugal vials made from polypropylene, which is compatible with IPA. After finishing centrifugation, the supernatant solution was removed using a plastic pipettor and then stored in a new vial, and sealed for later characterization.

Table 3.3: Centrifugation results for trial 4 (grinded for 1.5 hours at 500 rpm) and trial 8 (grinded for 1.5 hours at 250 rpm).

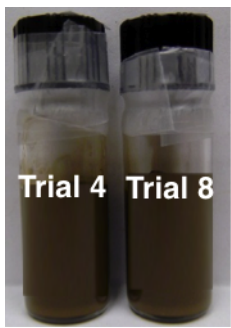
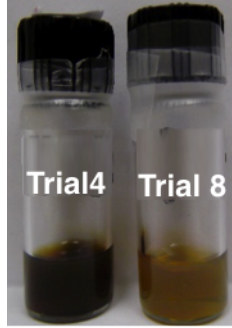
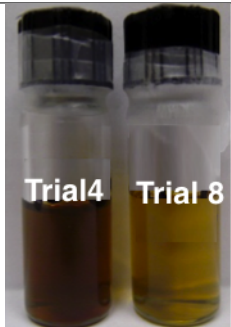
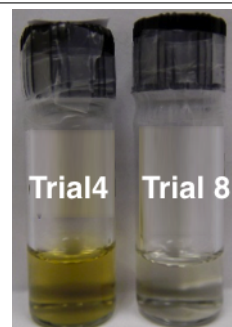
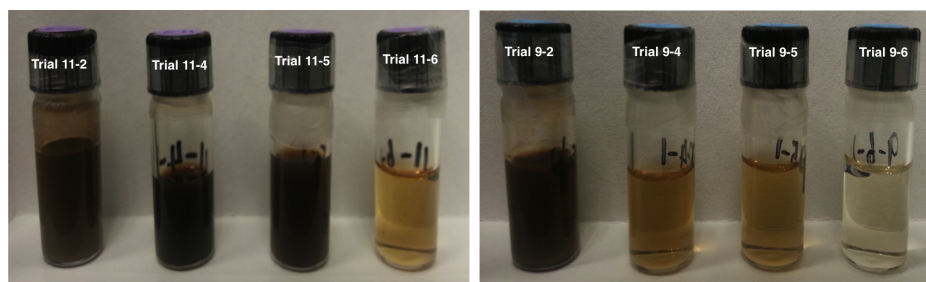
3000 rpm & 3 min	10000 rpm & 26 min
	
3000 rpm & 294 min	10000 rpm & 100 min
	

Table 3.3 shows some results of centrifuged samples. For low speeds and short centrifuge times, both samples retained their dark brown colour (high concentrated solution). After increasing the time, both samples became lighter, with trial 8 more transparent than trial 4. Figure 3.4 shows a comparison between trial 11 and trial 9, for different speeds and times of centrifugation. According to this data, it seems that for every centrifugal speed and grinding trial there is a critical time for transforming the dark brown colloidal suspension to becoming transparent.



(a) Trial 11 : grinded for (3 hours at 500 rpm) (b) Trial 9 : grinded for (15 hours at 400 rpm)

Figure 3.4: Silicon colloidal suspensions after centrifugation for (12 minutes at 3000 rpm, 55 minutes at 7000 rpm, 26 minutes at 10000 rpm, 100 minutes at 10000 rpm) left to right for both figures

3.4 Fabrication of Si Nanoparticle Thin Films

To fabricate Si particle films, drop-coating and layer-by-layer deposition techniques are employed using a mechanical pipette in which the volume of a drop can be adjusted from a minimum of 0.1 μ L up to maximum of 10 μ L.

For depositing Si particle films, three types of substrates are used: microscope cover glass, Si/Au/Al/Co wafers, and interdigitated gold electrode substrate. Each type of substrate is used for different methods of characterization as listed in Table 3.4. Figure 3.5 illustrates the deposition process in the above mentioned substrates. Prior to using these substrates, they were rinsed with acetone, IPA, and deionized water (DI) and then dried with nitrogen N_2 gas. Before any deposition, the colloidal solutions obtained from different trials were sonicated for 3-5 minutes. The volume and number of layers deposited on each film was variable.

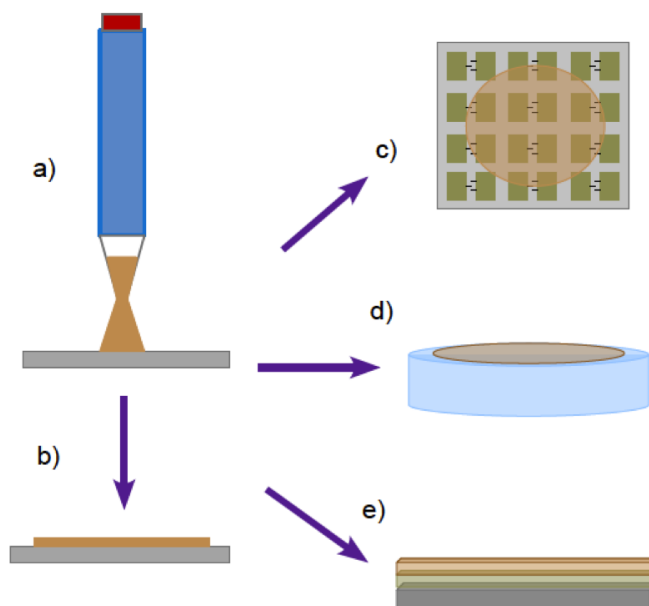


Figure 3.5: Deposition process of Si nanoparticle film by drop-coating and layer by layer deposition using a mechanical pipette a) during deposition, b) after deposition, and type of substrates are: c) deposition on a interdigitated gold electrode array substrate, d) glass substrate and e) Si/Au/Al/Co wafer substrate.

Table 3.4: Types of substrates used for fabrication of thin films.

- Substrate	Method of Characterization
- Circular glass slides	- Optical Microscopy and Raman Spectroscopy
Si/Au/Al/Co Substrates	- Scanning Electron Microscopy
- Interdigitated Gold Electrode Substrates	- <i>I-V</i> Characterization

3.5 Microscopy

Information about the size distribution and morphology of the milled Si particles was obtained using optical microscopy and scanning electron microscopy (SEM).

3.5.1 Optical Microscopy

Figure 3.6 shows two optical images of Si particles milled for 3 hours at 500 rpm and for 15 hours at 400 rpm at 20X objective magnification. Both images show a homogenous film except for some nearly spherical particles. The size of particles for a short grinding time appears larger than that of a long grinding time.

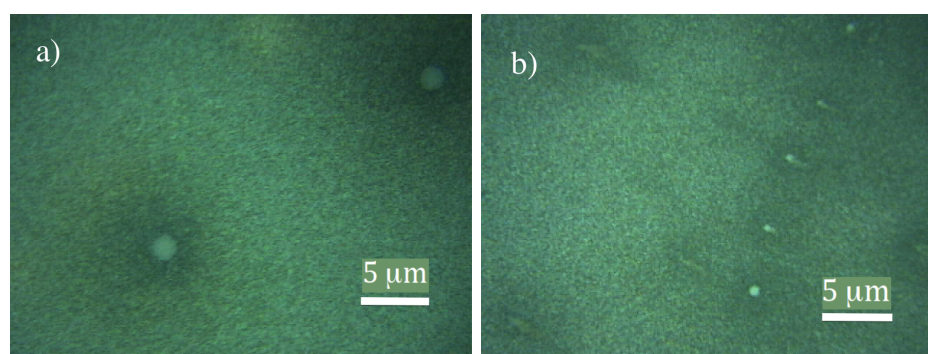


Figure 3.6: Optical images of silicon particles films on glass substrate after centrifugation for 3000 rpm at 12 min a) Trial 11: grinded at (500 rpm & 3h) and b) Trial 9 : grinded at (400 rpm & 15h)

3.5.2 Scanning Electron Microscopy

SEM can give a more precise description of Si particle size and morphology. Several films were prepared for testing the efficiency of grinding and centrifugation parameters. The size and size-distribution were measured using a program by Xiwen Gong assuming that the particle has almost spherical shape.

Figure 3.7 shows two images of Si particles milled for 1 hour and 3 hours at a speed of 300 rpm and 500 rpm, respectively. The images show that the size of the Si particles was reduced from an average of 45 μm starting material to sub-micron in dimension. In Figure 3.7 b, the majority of Si particles have a size less than 100 nm. However, there are still some big particles and some agglomeration of Si particles that can be further reduced by using filtration techniques. Figure 3.8 shows Si particle films prepared for SEM after centrifugation. These films were prepared by depositing 2 μL of colloidal particles on Si/Al/Au/Co substrates for the image of Figure 3.8 b and Figure 3.8 c and using an addition drops colloidal particles for Figure 3.8 a. In

Figure 3.8 a the film consists of irregular shapes of Si particles with mean size of about 200 nm and a minimum of about 20 nm. In Figure 3.8 b the size of the Si particles is reduced with mean and minimum size of 180 nm and 20 nm, respectively. In contrast, in Figure 3.8 c, the sizes and shapes of Si particles are fairly uniform and the mean and minimum of Si particles are 130 nm and 40 nm, respectively, for longer grinding time of 8 hours.

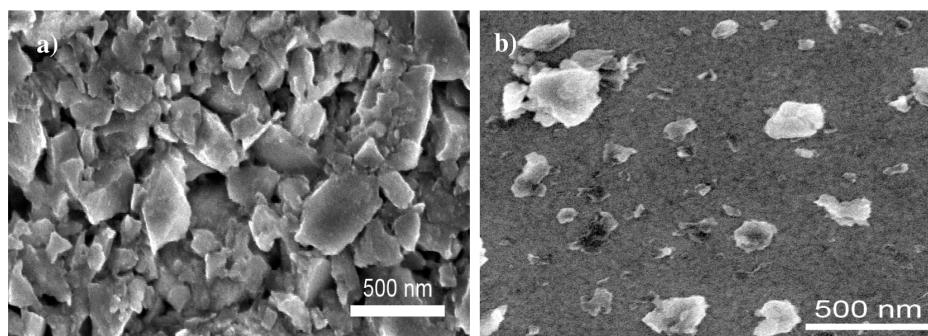


Figure 3.7: SEM images of silicon particles films on glass substrate after grinding a)milled for 1 hour at 300 rpm and b)milled for 3 hours at 500 rpm.

Figure 3.9 and Figure 3.10 show SEM images of Si particles milled for 15 hours at 400 rpm and centrifuged for 12 minutes at 3000 rpm and for 99 minutes at 100000 rpm, respectively. For Figure 3.9 a single layer of Si suspension of about $2\mu\text{L}$ is deposited on Si/Al/Au/Co substrates, and for Figure 3.10 the deposited film consisted of twenty drops of Si suspension using the same volume. The SEM image in Figure 3.9 shows a fairly wide-distribution of Si particle sizes and shapes with a mean size of 170 nm and minimum of 70 nm. In contrast, the SEM image of Figure 3.10 shows a narrower size and shape distribution of Si particles with a mean size of 70 nm and minimum of 20 nm. From all SEM images and average particle sizes plot, we can conclude that a long grinding time is required to produce more smaller sized particles and purification is necessary to narrow the size-distribution.

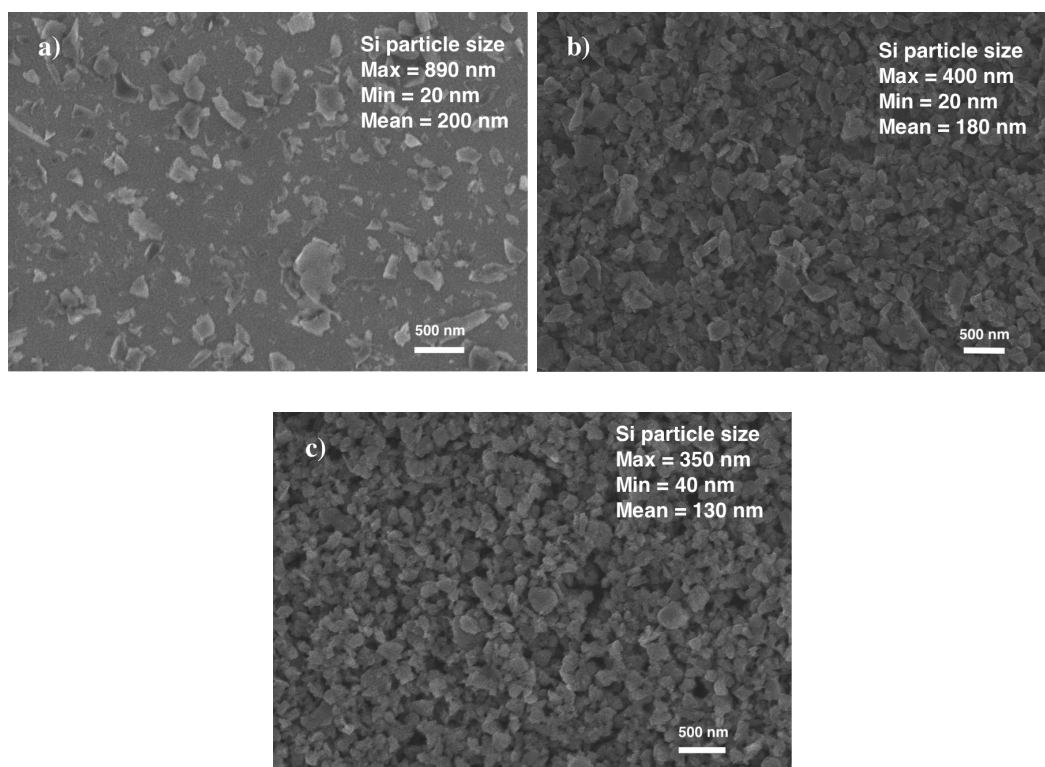


Figure 3.8: SEM images of Si particle films after centrifugation for a) 12 minutes at 3000 rpm (Trial 8) b) 12 minutes at 3000 rpm (Trial 11) and c) 55 minutes at 7000 rpm (Trial 10).

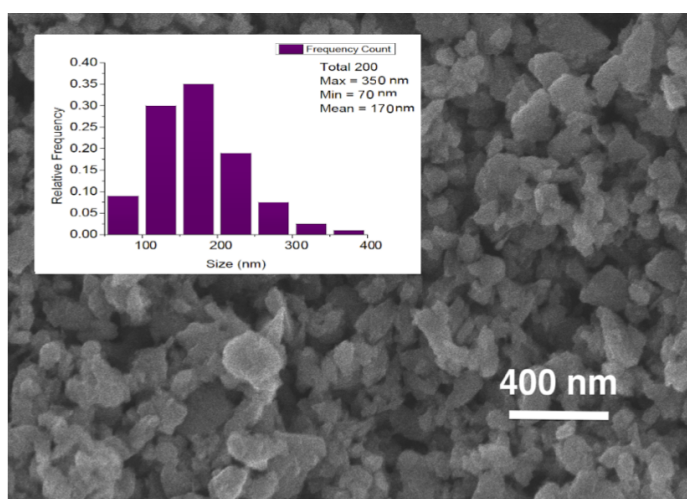


Figure 3.9: SEM image of silicon particles (grinded for 15 hours at 400 rpm) centrifuged for 12 minutes at 3000 rpm. The inset indicates the resulting particle size distribution.

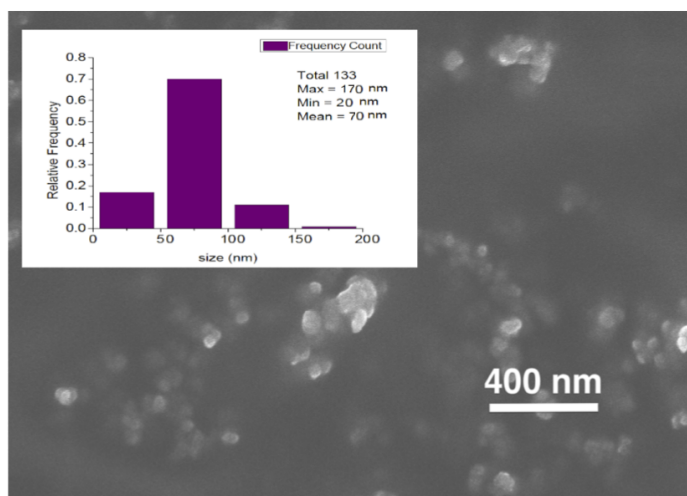


Figure 3.10: SEM images of silicon particles (grinded for 15 hours at 400 rpm) centrifuged for 99 minutes at 10000 rpm. The inset indicates the resulting particle size distribution.

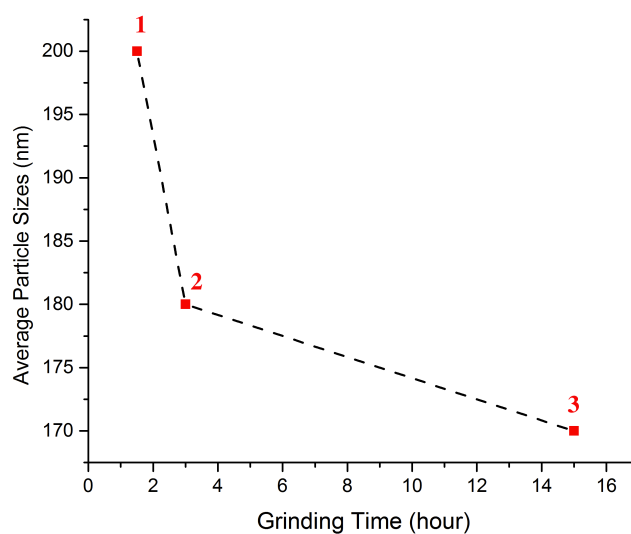


Figure 3.11: Average particle sizes versus grinding time at grinding speed of 1) 250 rpm, 2) 500 rpm and 3) 400 rpm. All centrifuged for 12 minutes at 3000 rpm.

The above SEM images demonstrate decreasing particle size by controlling grinding parameters, and narrowing size distribution via centrifugation.

3.6 Structural Analysis

3.6.1 Raman Spectroscopy

Raman scattering is an analytic tool for identifying materials through the interaction of photons with vibrational modes of matter [104]. When light interacts with the matter, the interaction causes scattering of the light elastically or inelastically. In elastic scattering, the scattered light has the same frequency of the incident photon known as Rayleigh and thus no energy loss occurs. On the other hand, in inelastic scattering, the scattered light has a lower or higher energy than the incident light. When the scattered light loses energy, the scattered light is called Stokes. In contrast, when the scattered light gains energy, the scattered light is called anti-Stokes. These types of interactions can be represented in terms of frequency or energy level (see Figure 3.12). These interaction are usually represented in terms of frequency of the scattered light, and that frequency can be calculated as the following:

$$\tilde{\nu} = \frac{1}{\lambda_0} - \frac{1}{\lambda_\nu} \quad (3.3)$$

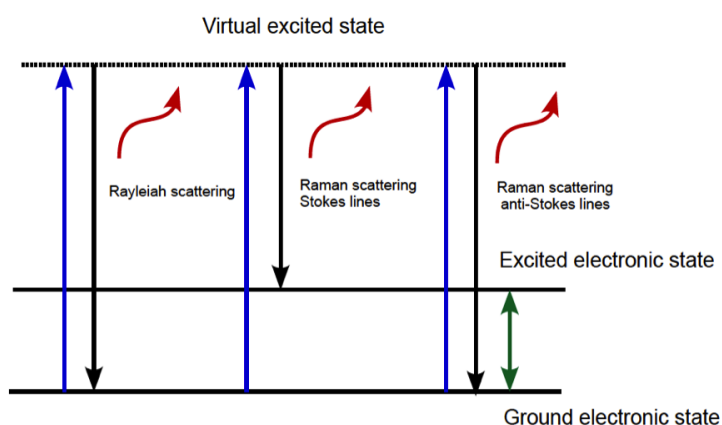


Figure 3.12: Energy level diagram showing three types of interaction of light with matter.

where λ_0 is the wavelength of the incident light, and λ_ν is the wavelength of the scattered light. The frequency of the scattered light is expressed in wavenumber units (cm^{-1}), by conversion.

Rayleigh, Stokes, and anti-Stokes lines differs in intensity. Rayleigh scattering line is six orders of magnitude higher intensity than both Raman scattering lines. Thus, to measure Raman scattering lines, filtration of the Rayleigh lines is necessary. Every material has its own Raman fingerprints. Any changes of material properties such as symmetry or temperature can cause alteration of the Raman peaks.

Raman peak shifts were observed several decades ago for a variety of materials including hydrogenated microcrystalline silicon prepared in hydrogen plasma. These observations showed a correlation between lattice expansion and the finite dimension of the crystallite in the film [105, 106]. The study suggested that surface stress may modify the shape of the microcrystals, which in turn affects the shift of the Raman peak. Raman shifts have also been observed in nanostructures such as silicon nanoparticles [90, 91]. Research by Hessel and his group showed that free standing Si nanoparticles show a Raman redshift while SiNPs embedded in oxide matrix show a blue shift [107]. Raman shifts have also been studied theoretically and various models have been developed to estimate particle size through Raman shift such as Bond polarization and the RWL model [107].

To estimate the shift of the Raman peak of milled Si particle films a Renishaw Raman microscope was used, available in the Physics Department at the University of Victoria (see Figure 3.13). The films were prepared from different concentrations of colloidal Si solutions. To measure Raman scattering, a 633 nm laser was as an excitation source. This laser was focused on the sample through an optical microscope. In all the measurements, the laser was focused on the sample for a very short time to avoid heating of the sample. The exposure time of the laser did not exceeded 10 s and the power level of the laser was 10% of max or less. The back scattered light from the sample is collected using the same optical microscope and sent into a spectrometer. The CCD camera was coupled with a PC interface that allows storing and manipulating Raman data.

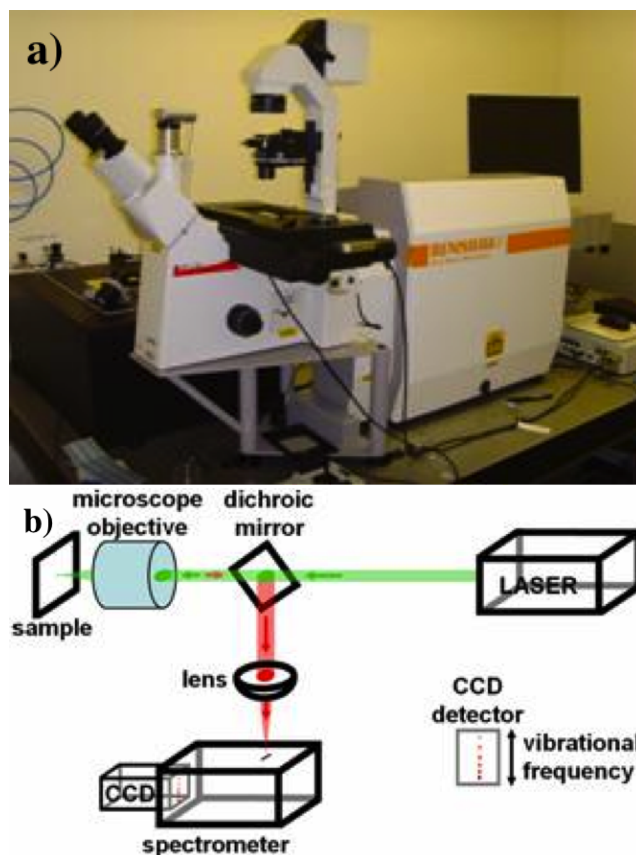


Figure 3.13: a) Renishaw Raman microscope (InVia) b) A simple diagram of the components of a Renishaw Raman system. After [108].

Raman measurements were conducted for films consisting of $5 \mu\text{L}$ of colloidal solution deposited on glass substrates. The number of drops deposited on each substrate is increased up to 5 depending on the concentration of the solution. Figure 3.14 shows Raman spectra for Si particle films milled for different milling times. Raman spectra for a calibrated Si crystal shows a sharp peak at 521 cm^{-1} and a full width at a half maximum (FWHM) of 6.32 which corresponds to the scattering of the first-order transverse phonon (TO) of crystalline silicon [105]. The milled Si particles exhibit a Raman red shift and a sharp peak with a broadening toward low frequencies. There was also a difference in FWHM and this width kept changing from a-e. The values of FWHM were 22, 19, 40 and 7, for (a-e). Additional peaks were often seen with extended broadening from $400\text{-}500 \text{ cm}^{-1}$. For peaks around $(445\text{-}459) \text{ cm}^{-1}$, silicon dioxide (SiO_2) could be the cause[91]. Figure 3.15 shows different Raman spectra for two of the films. These shifts may be due to quantum confinement effects for smaller

milled particles. In general, the Raman shift also could be due to surface stress.

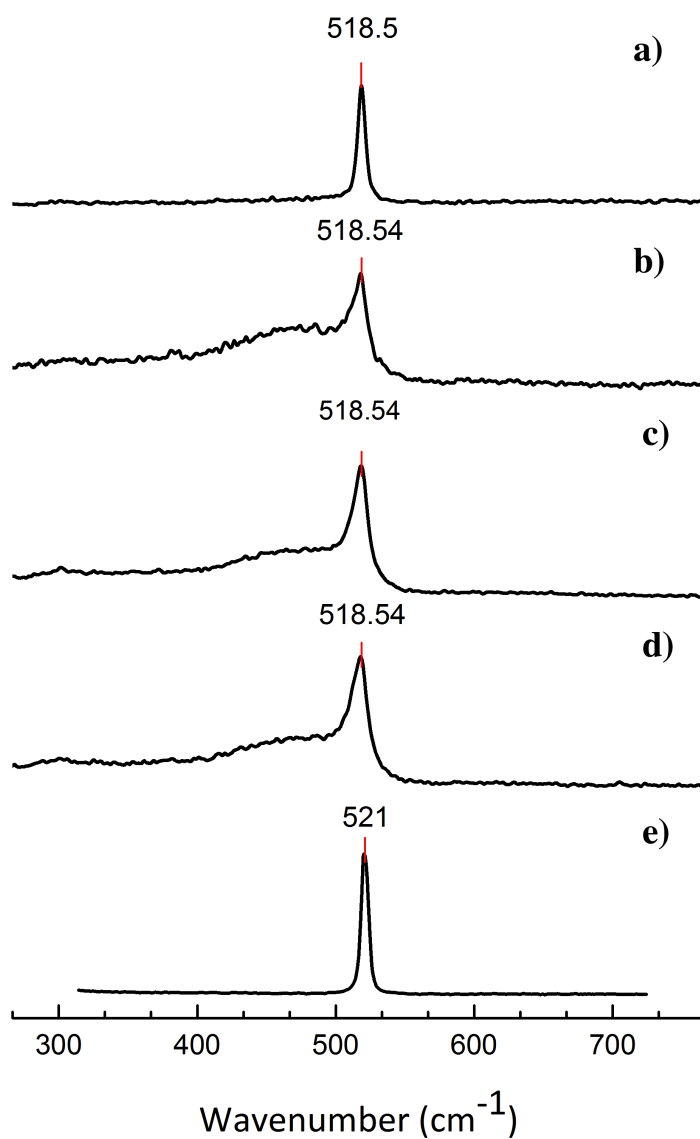


Figure 3.14: Raman spectra of Si particle films on a glass slide substrate a) trial 9, b) trial 10, c) trial 11, d) trial 4. All were centrifuged for 12 minutes at 3000 rpm and e) c-Si.

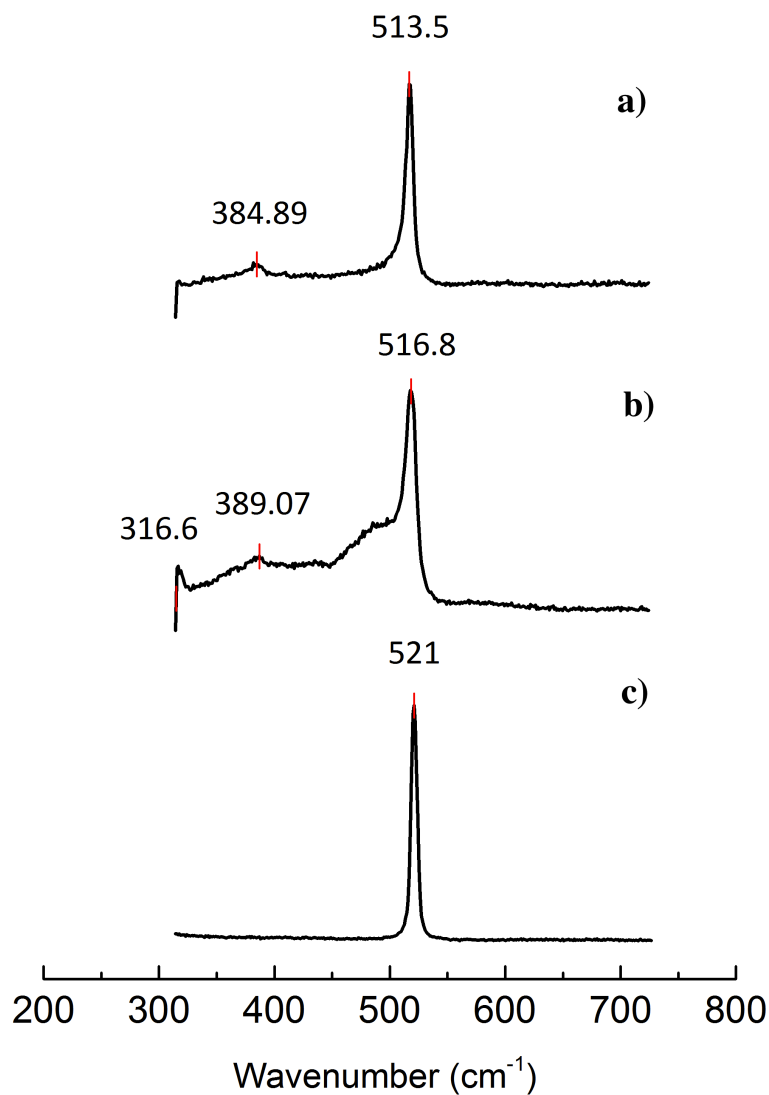


Figure 3.15: Raman spectra of Si particle films on a glass slide substrate for a) trial 11, and b) trial 9 centrifuged both centrifuged for 12 minutes at 3000 rpm and c) c-Si.

3.6.2 Energy Dispersive Spectroscopy

Similar to Raman spectroscopy energy dispersive X-ray spectroscopy (EDS) is a non-destructive analytic tool capable of providing chemical information about the elemental composition of the material being mapped [109]. Figure 3.16 provides an SEM

image of Si particle films on a Si/Au/Al/Co substrate and the elemental mapping. The elemental mapping shows that the film consists mainly of Si and Au and some oxygen (O) distributed over the film. The highest concentration is associated with Si particles weight percentage of 63.65. For other elements, the weight percentage are 22.59, 8.31, and 6.45, for Au, Ti, and O, respectively. The presence of O is most likely due to oxidation of Si film. More precise information about the quantity of each element can be obtained from EDS spectra in Figure 3.17. The data shows that the highest count is for silicon than gold.

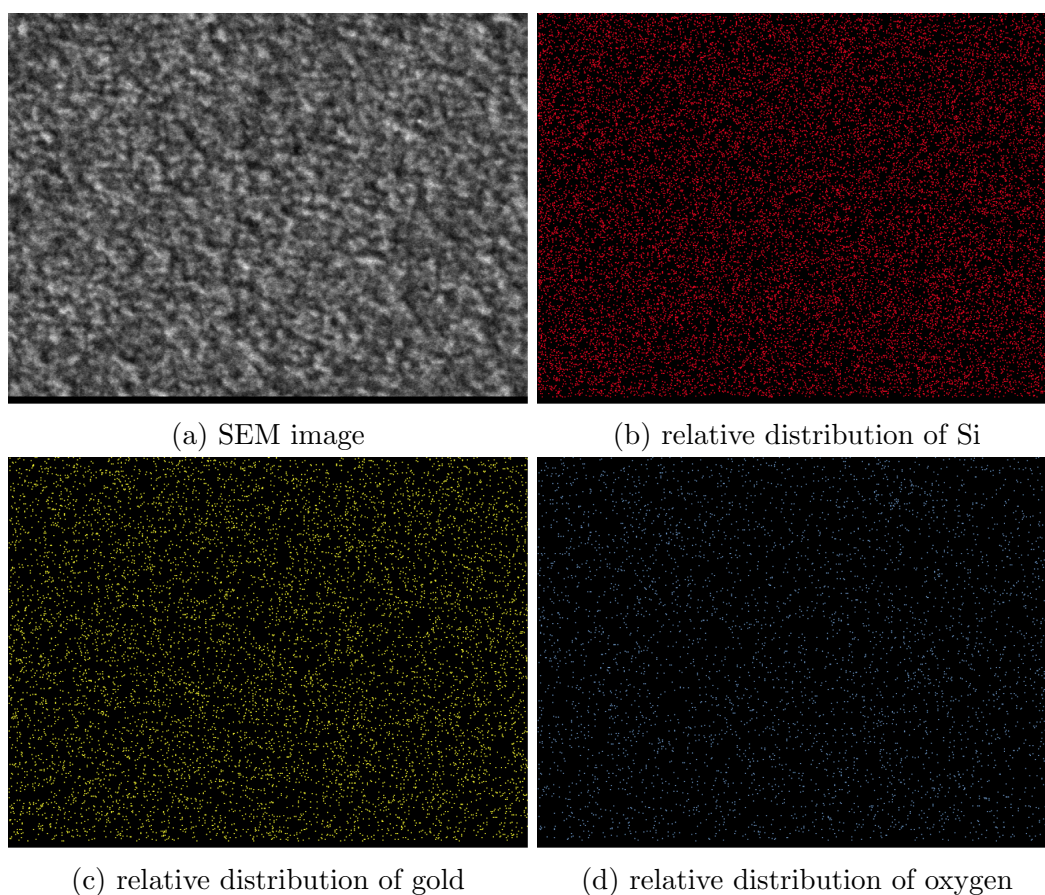


Figure 3.16: EDS spectroscopy mapping images of Si particle film.

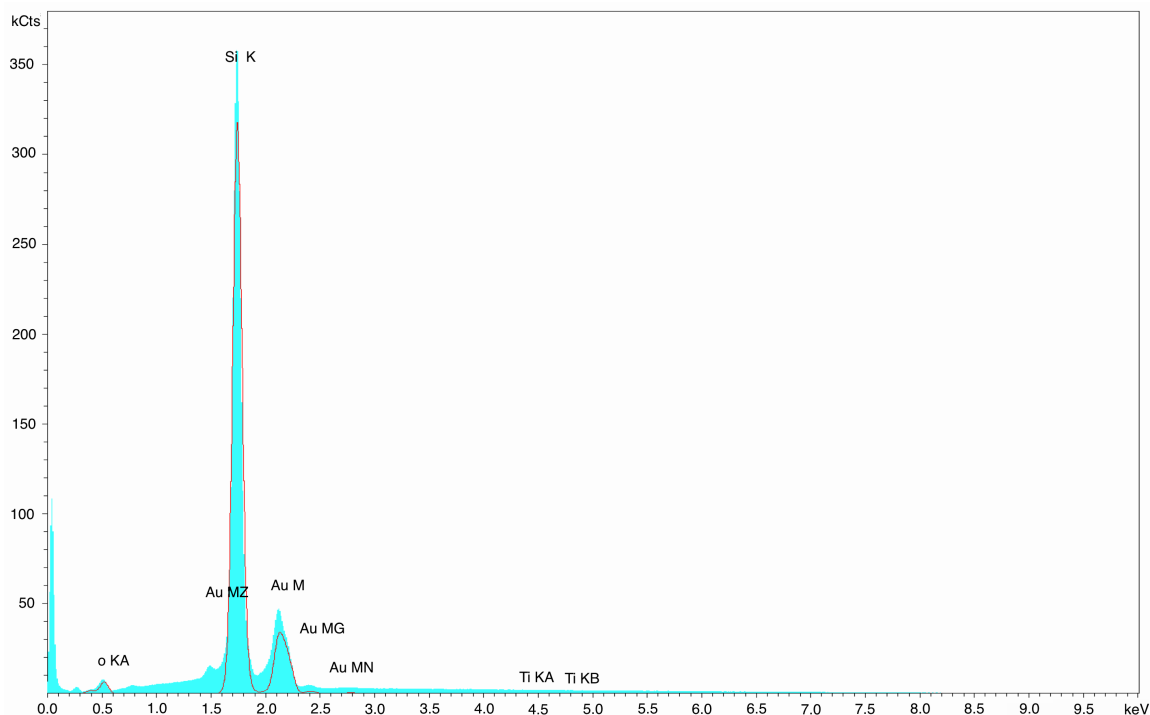


Figure 3.17: EDS spectrum of Si particle film on glass slide substrate.

3.7 Electrical Characterization

Room temperature current-voltage I - V characteristic of gold(Au) /semiconductor Si particle film/Au was measured using a two-terminal configuration with a microprobe station (Keithley 4200). Table 3.5 lists the sample parameters.

The substrate for I - V characterization is a silicon wafer coated with silicon dioxide and patterned with an array of interdigitated gold electrodes. Si particle films are made by depositing the colloidal solution using drop-coating and layer-by-layer techniques. Figure 3.18 b shows a cross-section of one electrode and its dimension after deposition of Si particle film.

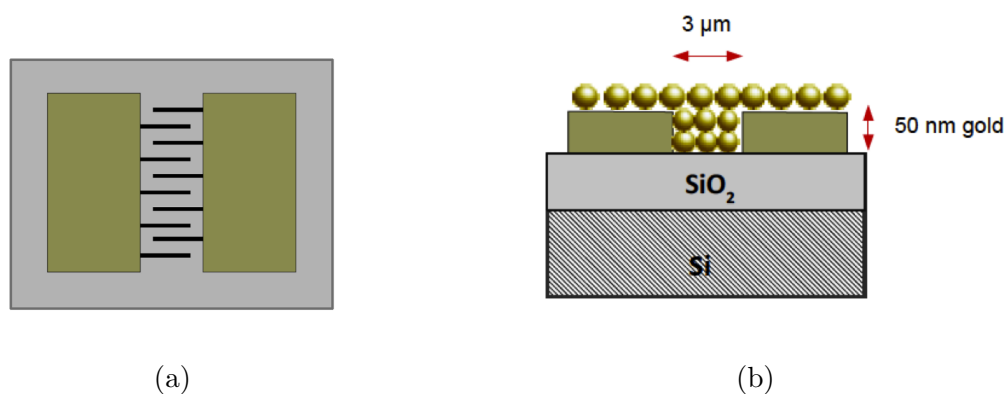


Figure 3.18: a) Top view schematic of interdigitated electrodes without any particle film and b) a cross-section of the electrodes after deposition.

Table 3.5: Names of the samples and their parameters used for I - V characterization

Names	Grinding parameters	Centrifuged parameters
sample A	1.5 hours at 500 rpm	30 minutes at 1000 rpm
sample B	0.5 hour at 500 rpm	13 minutes at 3000 rpm
sample C	0.5 rpm at 500 rpm	55 minutes at 7000 rpm
sample D	15 hours at 400 rpm	55 minutes at 7000 rpm

3.7.1 Short-Time Grinding

The first set of I - V characterization was performed for Si particle films milled for 0.5 hour and 1.5 hours at 500 rpm (see Table 3.5). The films were prepared by depositing a single drop of (0.3-0.5) μL of colloidal Si particles on an interdigitated substrate. The I - V characteristics showed low current of about (10^{-12} A), indicating that these films are highly resistive or may have some residuals from the solvent blocking current flow. Later, annealing of these films was performed in argon for 90 minutes at 250°C to enhance the electrical contact between the electrodes and the Si nanoparticles. After applying large biases, the I - V curves of some films changed.

Figure 3.19 shows I - V characteristic of Au/Si particle film/Au at three different applied biases. When the applied voltage is (-1,1) V, very low current resulted. As

the voltage increased, diode-like behaviour was obtained, and the current increased in the forward direction by three orders of magnitude after increasing the voltage to 3V.

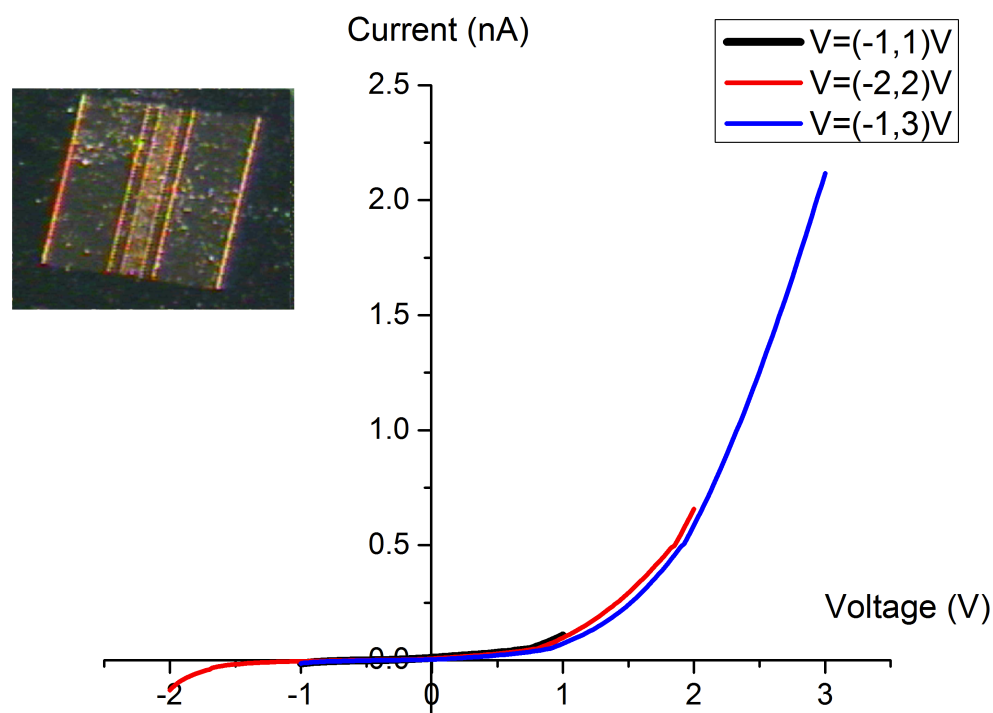


Figure 3.19: I - V characteristic of Au/Si particle film/Au annealed for 90 minutes at 250 °C in argon, samples A. The inset shows a magnified optical image of one electrode in the interdigitated gold substrate.

3.7.2 Long-Time Grinding

I - V measurements were performed on Si particle films milled for longer times after having two drops of Si particles. An annealing of these films was performed in an oven for 1 hour at 70 °C in air to dry the film. Similar to the shorter grinding times, the I - V curve displayed a low current of about 10^{-12} A. Figures 3.20-3.22 show I - V characteristics four drops of Si particles scanned at different locations on the substrate. Figure 3.20 shows nonlinear behavior with a low current, Figure 3.21 shows a non-

linear and non-ohmic behavior, and Figure 3.22 shows a diode-like behavior after increasing the voltage.

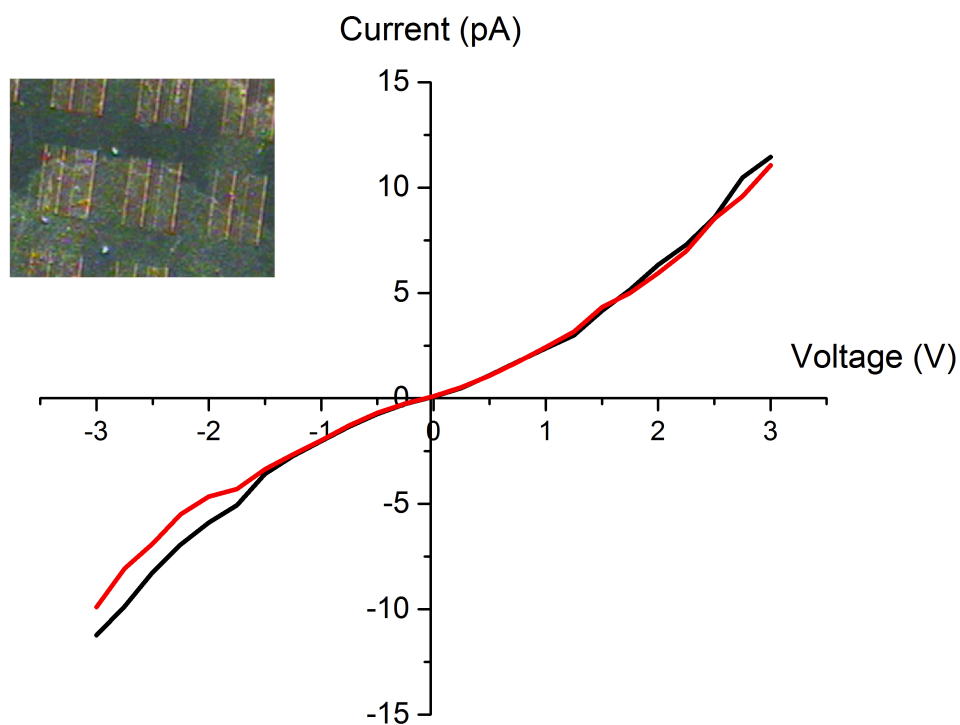


Figure 3.20: I - V characteristic of Si particle films annealed for 1 hour at 70°C in air (sample D) for two successive measurements. The inset shows an optical image of Si particle film on an interdigitated substrate.

3.8 Discussion

Our colloidal grinded as-produced Si nanoparticles had a wide-distribution of shapes and sizes. To narrow the distribution of the particles, a purification technique employed that is centrifugation in which the parameters were varied to efficiently separate the particles. By varying the time and speed, a threshold time for every rotation speed was obtained. Milling and centrifugation methods decreased the initial Si powder size from from $45\ \mu\text{m}$ to below $100\ \text{nm}$. Further purification of the colloidal

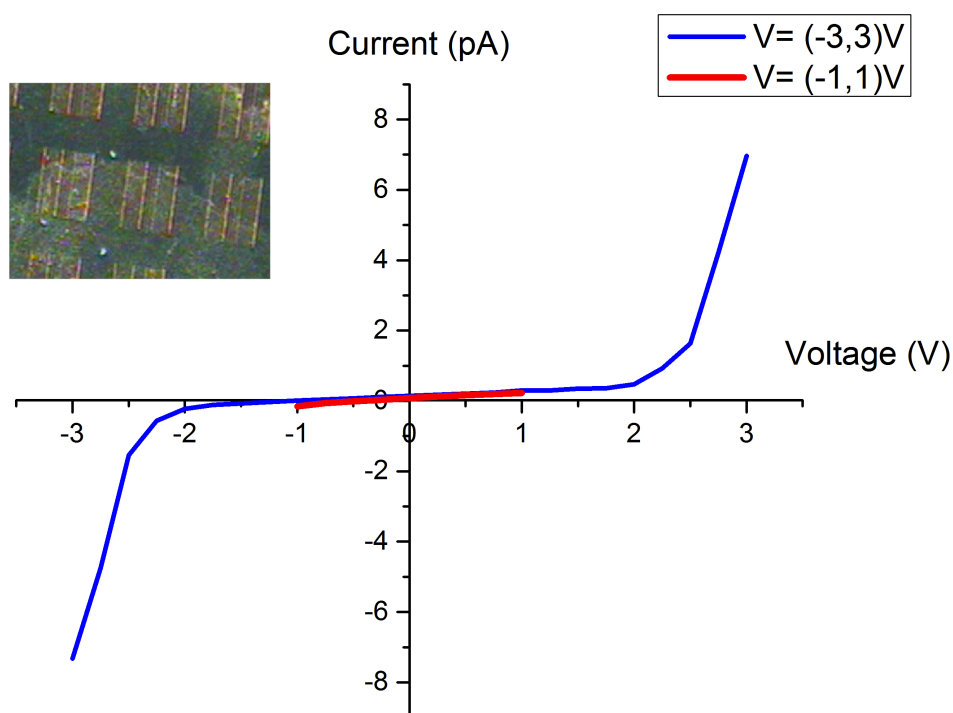


Figure 3.21: I - V characteristic of Si particle films annealed for 1 hour at 70°C in air (sample D) for three successive measurements. The inset shows an optical image of Si particle film on interdigitated substrate.

particles led to a narrow size-distribution and more uniform shapes; as shown by SEM imaging.

Structural and compositional analysis data showed that the milled particles also contained oxygen. Raman spectroscopy analysis showed that all milled Si nanoparticles showed Raman peak shift at 518.5 cm^{-1} with a broadening toward the low frequency. However, with performing another scanned in some samples such as trial 9 and trial 11 Raman peak shift at 516.8 cm^{-1} and 513.5 cm^{-1} were found for trial 11 and trial 9 respectively. It could be possible that the Raman shift is due to the stress that employed during grinding similar to the observation of the same peak shift in microcrystalline silicon. However, the appearances of lower Raman peak shift may indicate that these films consist of small sizes of Si nanoparticles. These results of

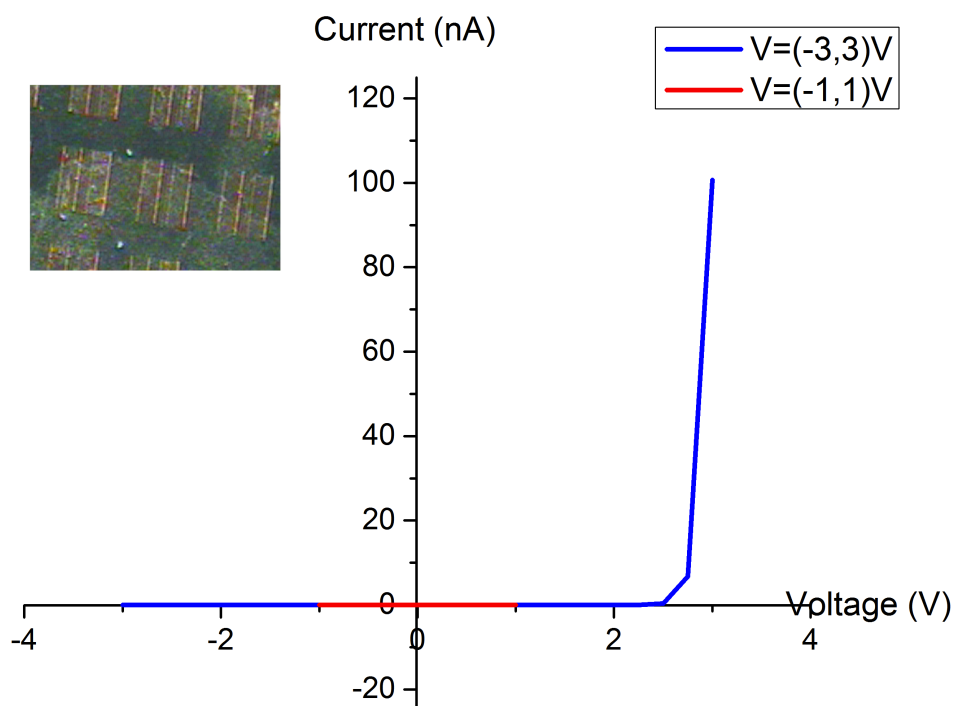


Figure 3.22: I - V characteristic of Au/Si particle film/Au annealed for 1 hour at 70°C in air (sample D). The inset shows an optical image of Si particle film on an interdigitated substrate.

Raman peak shift agree very well with the modeled cubic SiNCs. The calculated Raman spectrum of $\text{Si}_{64}\text{H}_{84}$ and $\text{Si}_{216}\text{H}_{198}$ showed peaks shift at 454 cm^{-1} and at 514 cm^{-1} . In fact, the Raman peak shift for cubic $\text{Si}_{216}\text{H}_{198}$ is very close to the value of Raman peak shift of trial 9 at 513.5 cm^{-1} .

In our study, a variety of I - V characteristics were found. Annealed films for 90 minutes at 250°C in Argon atmosphere showed an ohmic behaviour at low biase, which agrees with Ge NC films deposited on gold electrodes where the spacing between electrodes is $100\text{ }\mu\text{m}$ [110]. However, at a higher applied voltage, the Si particle film showed Schottky diode behaviour with a higher forward current in range of nA. The irregular distribution of Si particles are seen in the SEM images, and, thus, may result in a variation of the electrical film properties. The transport of charge carriers

in the films becomes complicated because of the multiple possible current paths. Long grinding time films also showed a variation of I - V characteristics. In general, all I - V curves showed nearly linear behaviour at low bias and further increase up to 2.8 V resulted in a symmetric non-linear curve in both forward and reverse bias or in some cases a Schottky diode barrier-like behaviour.

3.9 Conclusion

Colloidal grinding method is a straightforward route to synthesis of nanoparticles without the complexity of wet-chemistry approaches. In this method, sub-micron particles were achieved after one hour of grinding at 300 rpm. Further control of grinding parameters, e.g. grinding speed and time have led to an efficient size reduction below 100 nm. Centrifugation of the colloidal solution allowed the size-distribution of Si particles to be narrowed and leads to more uniform shapes. Raman and DES spectroscopy showed that the milled particles consisted mainly of c-Si with some broadening indicating the presence of some amorphous silicon and silicon dioxide. The I - V characteristic of Si particle films were highly resistive for low biases; however, after annealing, and increasing the thickness and applied biases current was found to increase, in some case substantially.

Chapter 4

Conclusion and Future Work

4.1 Summary

The thesis is divided into parts:

In the first part of the thesis, a quantum mechanical approach has been used based on a semi-empirical method (VAMP). The semi-empirical Hamiltonians that have been employed to investigate silicon particles are AM1 and PM3. Prior to investigation of Si particles by the semi-empirical methods a validation test was performed in a known molecular system, i.e., benzene. Both AM1 and PM3 methods showed a very good description of ground state properties. Further investigation was also performed in benzene to study its excited state properties using configuration interaction methods such as full, CISD, and CIS. All configuration interaction methods gave a reasonable agreement to the experimental data of UV-vis spectra of benzene. Investigation of Si particles properties was then performed using AM1 and configuration interaction methods. To study the ground and excited properties of Si particles, different shapes and sizes have been modeled including cubic, rectangular, ellipsoidal and flat disk particle shapes. SiNCs passivated with hydrogen or oxygen, all the modeled SiNCs showed size-dependence HOMO-LUMO gap i.e the gap decrease as the size of the SiNCs increase. However Zahra Albu, revised 3rd draft, April 29, 2014r, SiNCs with hydrogen passivation followed one unified curve except SiNCs with oxygen pas-

sivation. Raman spectra calculations were also performed for some cubic shaped Si particles. The results showed a shift of Raman peaks as observed in Si nano particles experimentally.

In the second part of the thesis, a colloidal grinding approach was employed to Si particles in solution using a planetary ball mill (PM200). Colloidal grinding was performed by varying grinding speed and time parameters between (300-500) rpm and (0.5-15) hours. After grinding, the colloidal particles were extracted from the beads and centrifuged at speed of (1000-10000) rpm from a few seconds up to 5 hours. The Si particle films were deposited onto different substrates using drop coating and layer by layer deposition for different characterization purposes. SEM and optical images showed a very good size reduction is achieved after 30 minutes of grinding then further increase in grinding time and speed and control of centrifugation conditions led to a narrow size distribution (below 100 nm) and more uniform morphology. Raman and EDS spectroscopy showed that the Si particle film are mainly crystalline silicon with some oxygen. $I-V$ characterization showed that the Si particle films display Schottky diode or linear behaviour with low currents, which maybe due to distribution of the particles inside the film and/or their surface properties.

4.2 Future Work

Future work should focus on understanding both the modeling and experimental research, and the related device applications. Also, the future work on the should link between experimental and modeling research even though using quantum mechanics methods impose certain limitation such as the size of the modeled structures. In fact, the modeled structures have sizes much smaller than what we obtained in experiment. To obtain, a link between the modelled SiNCs with milled Si nanoparticles, other properties could measured such as optical properties or Raman spectrum. For example, measuring the optical absorption of the milled particle and compare it with the HOMO-LUMO gap of modelled SiNCs. Also, it would possible to modeled a small film consist of different sizes and/or shapes and then calculated Raman spectrum to compare it with the measured Raman spectrum.

4.2.1 Modeling

A better understanding of the geometrical optimization method is necessary for accurately predicting the properties of Si particles. It is reasonable to model Si particles covered with an oxide shell, with some defects (dangling bonds), or strains. In addition to obtaining a proper structure, it is important to understand the influence of the number of orbitals in calculating the excited state properties of the Si NPs.

4.2.2 Experiment

SEM images of the milled Si nanoparticles showed that all trials milled for long grinding time at high speed have small particles less than 20 nm. It maybe useful to performed more statistical analysis using SEM of all the milled Si nanoparticle with the same centrifugation parameters to obtain a clear view about the grinding conditions.

Grinding Parameters

To understand or to find optimal grinding parameters for achieving size reduction, a proper understanding of the influence of the various parameters for grinding efficiency is necessary. These parameters have been studied in the literature and include the influence of bead to powder ratio, bead sizes, and grinding in an isolated atmosphere. To optimize the Si particle film properties and to utilize them in optoelectronic devices, a proper investigation of the other parameters that influence the film is needed.

Filtration

In this project, to narrow the size-distribution of the colloidal suspension, a centrifugation method was used. This method was effective in narrowing the particle size. To narrow the size distribution further, other filtration methods can be used such as membrane-based or nanomembrane filters [111].

Solvent Choice

Wet grinding of Si powder was performed using IPA. For efficient centrifugation according to Stokes Law, the viscosity of the solvent should be as low as possible choose. It is possible to choose another solvent with lower viscosity, e.g. ethanol. Additionally, the solvent choice can play an important role in obtaining a random or ordered particle film via controlled particle flocculation or slow solvent evaporation [110,112]. For example, a periodic structure of Ge NPs was obtained after applying a variety of solvents. Also, the solvent choice can be used for doping and stability of deposited film. Ligands are usually used to provide particle solubility, define particle morphology as well as doping. Some literature showed that the choice of solvent may replace the need for using ligands via hypervalent interaction using Lewis based theory [113].

Oxide removal

The milled Si particles contained oxygen. This may be one reason for the low current obtained in I - V characteristics. To remove the oxide layer hydrofluoric acid (HF) etching is widely used [114].

Bridging Molecules

The produced Si particle films are randomly distributed. In the literature, it is demonstrated that using a bridge molecule can help ensure the smoothness of the film, enhancement of the conductivity, and an increase of light absorption as well[55]. This concept has been used with PbS QDs, where the bridging molecule was ethanedithiol [55].

Device structure

In this thesis, colloidal Si particles have been used to fabricate a simple device structure consisting of two terminals, in which metal-Si particle film junctions form by depositing Si particles in pre-pattern interdigitated gold electrode arrays. More complex designs can be fabricated by incorporating the Si particle film with another semiconductor material such as bulk inorganic or organic semiconductors in order to improve the performance. Many research conducted toward new combinations of semiconductor materials allow efficient absorption of radiation using organic hetero-junction blends with NC, quantum dot junctions, or bulk heterojunction structures.

A simple illustration of these possible structures is shown in Figure 4.1 using the Si nanoparticles as studied in this work.

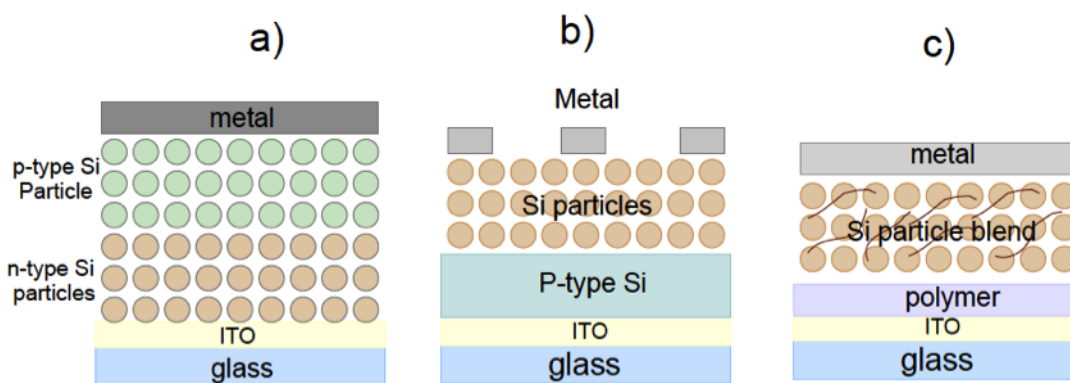


Figure 4.1: Heterojunction solar cell based on colloidal Si particle film. a) quantum dot junction, b) bulk heterojunction, c) heterojunction blend.

Bibliography

- [1] J. D. Cressler, *Silicon Earth: Introduction to the microelectronics and nanotechnology revolution*. Cambridge: Cambridge University Press, 2009.
- [2] S. R. Wenham, M. A. Green, M. E. Watt, and R. Corkish, *Applied Photovoltaics*. GB: Earthscan, 2007.
- [3] J. L. Gray, “The physics of the solar cell,” in *Handbook of photovoltaic science and engineering* (A. Luque and S. Hegedus, eds.), John Wiley & Sons, 2003.
- [4] C. Schüller, *Inelastic light scattering of semiconductor nanostructures: fundamentals and recent advances*, vol. 219. Berlin: Springer, 2006.
- [5] A. A. Goetzberger and V. U. Hoffmann, *Photovoltaic solar energy generation*, vol. 112. New York: Springer Berlin Heidelberg, 2005.
- [6] H. Zimmermann, *Integrated silicon optoelectronics*, vol. 148. Berlin: Springer, 2010.
- [7] J. Lutz, H. Schlangenotto, U. Scheuermann, and R. De Doncker, *Semiconductor power devices: physics, characteristics, reliability*. Springer, 2011.
- [8] M. A. Green, *Solar cells: operating principles, technology, and system applications*. Englewood Cliffs, NJ: Prentice-Hall, 1982.
- [9] Z. Yuan, A. Anopchenko, N. Daldosso, R. Guider, D. Navarro-Urrios, A. Pitanti, R. Spano, and L. Pavesi, “Silicon nanocrystals as an enabling material for silicon photonics,” *Proceedings of the IEEE*, vol. 97, no. 7, pp. 1250–1268, 2009.
- [10] A. M. Fox, *Optical properties of solids*, vol. 3. Oxford: Oxford University Press, 2010.

- [11] O. E. Semonin, J. M. Luther, and M. C. Beard, “Quantum dots for next-generation photovoltaics,” *Materials Today*, vol. 15, no. 11, pp. 508–515, 2012.
- [12] L. C. Lew Yan Voon, M. Willatzen, and S. E. Collection, *The k-p method: electronic properties of semiconductors*. New York: Springer Berlin Heidelberg, 2009.
- [13] D. Bimberg and U. Pohl, “Quantum dots: promises and accomplishments,” *Materials Today*, vol. 14, no. 9, pp. 388–397, 2011.
- [14] A. E. Saunders and B. A. Korgel, “Order nanoparticle assemblies,” in *Handbook of nanophysics* (K. D. Sattler, ed.), pp. (20–1)–(20–13), CRC Press, 2011.
- [15] L. L. Araujo and M. C. Ridgway, “Embedded nanoparticles,” in *Handbook of nanophysics* (K. D. Sattler, ed.), pp. (23–1)–(20–15), CRC Press, 2011.
- [16] B. G. Lee, D. Hiller, J. W. Luo, O. E. Semonin, M. C. Beard, M. Zacharias, and P. Stradins, “Strained interface defects in silicon nanocrystals,” *Advanced Functional Materials*, vol. 22, no. 8, pp. 3223–3232, 2012.
- [17] J. H. Warner, A. Hoshino, K. Yamamoto, and R. Tilley, “Water-soluble photoluminescent silicon quantum dots,” *Angewandte Chemie*, vol. 117, no. 29, pp. 4626–4630, 2005.
- [18] J. D. Holmes, K. J. Ziegler, R. C. Doty, L. E. Pell, K. P. Johnston, and B. A. Korgel, “Highly luminescent silicon nanocrystals with discrete optical transitions,” *J. Am. Chem. Soc.*, vol. 123, no. 16, pp. 3743–3748, 2001.
- [19] A. M. Smith and S. Nie, “Silicon nanocrystals,” in *Handbook of nanophysics* (K. D. Sattler, ed.), pp. 190–200, CRC Press, 2011.
- [20] J. Tang, K. W. Kemp, S. Hoogland, K. S. Jeong, H. Liu, L. Levina, M. Furukawa, X. Wang, R. Debnath, D. Cha, *et al.*, “Colloidal-quantum-dot photovoltaics using atomic-ligand passivation,” *Nature Materials*, vol. 10, no. 10, pp. 765–771, 2011.
- [21] Z. Zhou, L. Brus, and R. Friesner, “Electronic structure and luminescence of 1.1- and 1.4-nm silicon nanocrystals: oxide shell versus hydrogen passivation,” *Nano Letters*, vol. 3, no. 2, pp. 163–167, 2003.

- [22] J. E. Murphy, M. C. Beard, and A. J. Nozik, "Time-resolved photoconductivity of PbSe nanocrystal arrays," *The journal of physical chemistry. B*, vol. 110, no. 50, pp. 25455–25461, 2006.
- [23] D. Piazza, M. Carmela., and G. Vitale, *Photovoltaic sources: modeling and emulation*. London: Springer, 2013.
- [24] Philibert, *Solar energy perspectives*. Paris: Organisation for Economic Cooperation and Development (OECD), 2011.
- [25] E. Greenpeace, "Solar generation 6. solar photovoltaic electricity empowering the world," *European Photovoltaic Industry Association*, 2011.
- [26] I. E. Agency, *Technology Roadmap: Nuclear Energy*. Paris: OECD Publishing, 2010.
- [27] J. Tang and E. H. Sargent, "Infrared colloidal quantum dots for photovoltaics: fundamentals and recent progress," *Advanced Materials*, vol. 23, no. 1, pp. 12–29, 2011.
- [28] A. McEvoy, T. Markvart, and L. Castañer.
- [29] M. A. Green, K. Emery, Y. Hishikawa, W. Warta, and E. D. Dunlop, "Solar cell efficiency tables (version 39)," *Progress in Photovoltaics: Research and Applications*, vol. 20, no. 1, pp. 12–20, 2012.
- [30] A. Mette, *New Concepts for Front Side Metallization of Industrial Silicon Solar Cells*. dissertation, Fraunhofer Institute for Solar Energy Systems, 2007.
- [31] A. Labouret and M. Viloz, *Solar photovoltaic energy*, vol. 9. Stevenage: Institution of Engineering and Technology, 2010.
- [32] E. Co-operation and Development, *Technology Roadmap: Solar Photovoltaic Energy*. OECD Publishing, 2010.
- [33] A. Shah, P. Torres, R. Tscharnner, N. Wyrsh, and H. Keppner, "Photovoltaic technology: The case for thin-film solar cells," *Science*, vol. 285, no. 5428, pp. 692–698, 1999.
- [34] Vysakh, "Thin film solar cell [online]," Available: <http://www.circuitstoday.com/thin-film-solar-cell>. Accessed: Dec.10, 2013.

- [35] J. N. Burghartz, *Ultra-thin chip technology and applications*. New York: Springer New York, 2011.
- [36] H. Keppner, J. Meier, P. Torres, D. Fischer, and A. Shah, "Microcrystalline silicon and micromorph tandem solar cells," *Applied Physics A Materials Science & Processing*, vol. 69, no. 2, pp. 169–177, 1999.
- [37] A. Shah, J. Meier, E. Vallat-Sauvain, N. Wyrsh, U. Kroll, C. Droz, and U. Graf, "Material and solar cell research in microcrystalline silicon," *Solar Energy Materials and Solar Cells*, vol. 78, no. 1, pp. 469–491, 2003.
- [38] K. Ramanathan, M. A. Contreras, C. L. Perkins, S. Asher, F. S. Hasoon, J. Keane, D. Young, M. Romero, W. Metzger, R. Noufi, *et al.*, "Properties of 19.2% efficiency ZnO/CdS/CuInGaSe₂ thin-film solar cells," *Progress in Photovoltaics: Research and Applications*, vol. 11, no. 4, pp. 225–230, 2003.
- [39] "Thin film tandem solar cell [online]," Available: <http://large.stanford.edu/courses/2010/ph240/peters2/html>. Accessed: Dec. 12, 2013.
- [40] M. A. Green, *Third generation photovoltaics: advanced solar energy conversion*. Springer, 2003.
- [41] J. Meier, H. Keppner, S. Dubail, U. Kroll, P. Torres, P. Pernet, Y. Ziegler, J. Selvan, J. Cuperus, D. Fischer, *et al.*, "Microcrystalline single-junction and micromorph tandem thin film silicon solar cells," in *MRS Proceedings*, vol. 507, Cambridge Univ Press, 1998.
- [42] J. Yang, A. Banerjee, and S. Guha, "Triple-junction amorphous silicon alloy solar cell with 14.6% initial and 13.0% stable conversion efficiencies," *Applied Physics Letters*, vol. 70, no. 22, pp. 2975–2977, 1997.
- [43] H. T. Anders, C. Ute B, G. Boschlooa, S. Licheng, K. Lars, P. Henrik, and E. A. Gibsone, "Dye-sensitized photoelectrochemical cells," in *Practical handbook of photovoltaics: fundamentals and applications* (M. T. McEvoy, A. J and L. Castaner, eds.), Academic Press, 2012.
- [44] S. Yoo, B. Domercq, and B. Kippelen, "Efficient thin-film organic solar cells based on pentacene/C₆₀ heterojunctions," *Applied Physics Letters*, vol. 85, no. 22, pp. 5427–5429, 2004.

- [45] A. Luque, A. Martí, and A. J. Nozik, “Solar cells based on quantum dots: Multiple exciton generation and intermediate bands,” *MRS Bulletin*, vol. 32, no. 3, 2007.
- [46] K. Shinoda, S. Yanagisawa, K. Sato, and K. Hirakuri, “Stability of nanocrystalline silicon particles in solution,” *Journal of Crystal Growth*, vol. 288, no. 1, pp. 84–86, 2006.
- [47] A. Nozik, M. Beard, J. Luther, M. Law, R. Ellingson, and J. Johnson, “Semiconductor quantum dots and quantum dot arrays and applications of multiple exciton generation to third-generation photovoltaic solar cells,” *Chemical reviews*, vol. 110, no. 11, pp. 6873–6890, 2010.
- [48] G. Conibeer, “Third-generation photovoltaics,” *Materials Today*, vol. 10, no. 11, pp. 42–50, 2007.
- [49] T. Sugaya, O. Numakami, R. Oshima, S. Furue, H. Komaki, T. Amano, K. Matsuura, Y. Okano, and S. Niki, “Ultra-high stacks of InGaAs/GaAs quantum dots for high efficiency solar cells,” *Energy & Environmental Science*, vol. 5, no. 3, pp. 6233–6237, 2012.
- [50] G. F. Brown and J. Wu, “Third generation photovoltaics,” *Laser & Photonics Reviews*, vol. 3, no. 4, pp. 394–405, 2009.
- [51] E. Sargent, “Colloidal quantum dot solar cells,” *Nature Photonics*, vol. 6, no. 3, pp. 133–135, 2012.
- [52] C. Y. Liu and U. R. Kortshagen, “A silicon nanocrystal schottky junction solar cell produced from colloidal silicon nanocrystals,” *Nanoscale Research Letters*, vol. 5, no. 8, pp. 1253–1256, 2010.
- [53] I. Gur, N. A. Fromer, M. L. Geier, and A. P. Alivisatos, “Air-stable all-inorganic nanocrystal solar cells processed from solution,” *Science*, vol. 310, no. 5747, pp. 462–465, 2005.
- [54] J. P. Clifford, K. W. Johnston, L. Levina, and E. H. Sargent, “Schottky barriers to colloidal quantum dot films,” *Applied Physics Letters*, vol. 75, no. 25, pp. 253117–253117–3, 2007.

- [55] E. J. Klem, D. D. MacNeil, P. W. Cyr, L. Levina, and E. H. Sargent, "Efficient solution-processed infrared photovoltaic cells: Planarized all-inorganic bulk heterojunction devices via inter-quantum-dot bridging during growth from solution," *Applied Physics Letters*, vol. 75, no. 18, pp. 183113–183113–3, 2007.
- [56] J. M. Luther, M. Law, M. C. Beard, Q. Song, M. O. Reese, R. J. Ellingson, and A. J. Nozik, "Schottky solar cells based on colloidal nanocrystal films," *Nano letters*, vol. 8, no. 10, pp. 3488–3492, 2008.
- [57] G. I. Koleilat, L. Levina, H. Shukla, S. H. Myrskog, S. Hinds, A. G. Pattantyus-Abraham, and E. H. Sargent, "Efficient, stable infrared photovoltaics based on solution-cast colloidal quantum dots," *ACS nano*, vol. 2, no. 5, pp. 833–840, 2008.
- [58] O. E. Semonin, J. M. Luther, S. Choi, H. Y. Chen, J. Gao, A. J. Nozik, and M. C. Beard, "Peak external photocurrent quantum efficiency exceeding 100% via MEG in a quantum dot solar cell," *Science*, vol. 334, no. 6062, pp. 1530–1533, 2011.
- [59] A. G. Pattantyus-Abraham, I. J. Kramer, A. R. Barkhouse, X. Wang, G. Konstantatos, R. Debnath, L. Levina, I. Raabe, M. K. Nazeeruddin, M. Gratzel, *et al.*, "Depleted-heterojunction colloidal quantum dot solar cells," *ACS nano*, vol. 4, no. 6, pp. 3374–3380, 2010.
- [60] G. H. Carey, K. W. Chou, B. Yan, A. R. Kirmani, A. Amassian, and E. H. Sargent, "Materials processing strategies for colloidal quantum dot solar cells: advances, present-day limitations, and pathways to improvement," *MRS Communications*, pp. 1–8, 2013.
- [61] S. A. McDonald, G. Konstantatos, S. Zhang, P. W. Cyr, E. J. Klem, L. Levina, and E. H. Sargent, "Solution-processed PbS quantum dot infrared photodetectors and photovoltaics," *Nature materials*, vol. 4, no. 2, pp. 138–142, 2005.
- [62] J. Tang, H. Liu, D. Zhitomirsky, S. Hoogland, X. Wang, M. Furukawa, L. Levina, and E. H. Sargent, "Quantum junction solar cells," *Nano letters*, vol. 12, no. 9, pp. 4889–4894, 2012.

- [63] K. Surana, *Towards silicon quantum dot solar cells: comparing morphological properties and conduction phenomena in Si quantum dot single layers and multilayers*. dissertation, Université de Grenoble, 2011.
- [64] S. Huang and G. Conibeer, “Sputter-grown Si quantum dot nanostructures for tandem solar cells,” *Journal of Physics D: Applied Physics*, vol. 46, no. 2, 2013.
- [65] X. Wang, G. I. Koleilat, J. Tang, H. Liu, I. J. Kramer, R. Debnath, L. Brozowski, D. A. R. Barkhouse, L. Levina, S. Hoogland, *et al.*, “colloidal quantum dot solar cells employing a graded recombination layer,” *Nature Photonics*, vol. 5, no. 8, pp. 480–484, 2011.
- [66] F. Jensen, *Introduction to computational chemistry*. Hoboken, NJ: John Wiley & Sons, 2007.
- [67] K. Ramachandran, G. Deepa, and K. Namboori, *Computational chemistry and molecular modeling: principles and applications*. Berlin: Springer, 2008.
- [68] D. Chakraborty, *Configuration Interaction (Singles) Study of Geometric and Electronic Properties of Conducting Polymers*. dissertation, Memorial University, 2000.
- [69] E. Lewars, *Computational chemistry: introduction to the theory and applications of molecular and quantum mechanics*. New York: Springer, 2011.
- [70] A. Cullis and L. Canham, “Visible light emission due to quantum size effects in highly porous crystalline silicon,” 1991.
- [71] D. Jurbergs, E. Rogojina, L. Mangolini, and U. Kortshagen, “Silicon nanocrystals with ensemble quantum yields exceeding 60%,” *Applied physics letters*, vol. 88, no. 23, pp. 233116–233116, 2006.
- [72] *Materials Studio Modeling version 4.0*. Accelrys Software Inc, 2005.
- [73] Q. Zhao, P. A. Graf, W. B. Jones, A. Franceschetti, J. Li, L. W. Wang, and K. Kim, “Shape dependence of band-edge exciton fine structure in CdSe nanocrystals,” *Nano letters*, vol. 7, no. 11, pp. 3274–3280, 2007.

- [74] E. Ramos, B. M. Monroy, J. C. Alonso, L. E. Sansores, R. Salcedo, and A. Martínez, "Theoretical study of the electronic properties of silicon nanocrystals partially passivated with Cl and F," *The Journal of Physical Chemistry C*, vol. 116, no. 6, pp. 3988–3994, 2012.
- [75] A. Martnez, J. C. Alonso, L. E. Sansores, and R. Salcedo, "Electronic structure of silicon nanocrystals passivated with nitrogen and chlorine," *The Journal of Physical Chemistry C*, vol. 114, no. 29, pp. 12427–12431, 2010.
- [76] D. Feller and D. A. Dixon, "Predicting the heats of formation of model hydrocarbons up to benzene," *The Journal of Physical Chemistry A*, vol. 104, no. 13, pp. 3048–3056, 2000.
- [77] N. Matsuzawa and D. A. Dixon, "Semiempirical calculations of the polarizability and second-order hyperpolarizability of fullerenes (C60 and C70), and model aromatic compounds," *The Journal of Physical Chemistry*, vol. 96, no. 15, pp. 6241–6247, 1992.
- [78] B. P. Stoicheff, "High resolution raman spectroscopy of gases: II. rotational spectrs of C6H6 and C6D6, and interunclear distances in the benzene molecules," *Canadian Journal of Physics*, vol. 32, no. 5, pp. 339–346, 1954.
- [79] S. Grimme and H. Loehmannsroeben, "MO theoretical investigation of strained PAH molecules: effects of methyl substituents in ground and excited states," *The Journal of Physical Chemistry*, vol. 96, no. 17, pp. 7005–7009, 1992.
- [80] B. Beck and U. Grummt, "Semiempirical calculations of first-order hyperpolarizabilities: Testing the performance of different methods in comparison to experiment," *The Journal of Physical Chemistry B*, vol. 102, no. 4, pp. 664–670, 1998.
- [81] V. O. Saik and S. Lipsky, "Absorption spectra of some liquids in the VUV," *The Journal of Physical Chemistry A*, vol. 105, no. 44, pp. 10107–10110, 2001.
- [82] T. Inagaki, "Absorption spectra of pure liquid benzene in the ultraviolet region," *The Journal of Chemical Physics*, vol. 57, p. 2526, 1972.
- [83] P. Clark and J. Ragle, "Electronic excited states of benzene and ethylene," *The Journal of Chemical Physics*, vol. 46, no. 11, pp. 4235–4241, 2004.

- [84] A. A. Bliznyuk, H. F. Schaefer III, and I. J. Amster, "Proton affinities of lysine and histidine: a theoretical consideration of the discrepancy between experimental results from the kinetic and bracketing methods," *Journal of the American Chemical Society*, vol. 115, no. 12, pp. 5149–5154, 1993.
- [85] R. Viruela Martín, P. M. Viruela Martín, and E. Ortí Guillen, "Theoretical determination of the geometric and electronic structures of oligorylenes and poli (peri-naphthalene)," vol. 97, no. 11, pp. 8470–8480, 1992.
- [86] S. Bakalova and J. Kaneti, "Semi-empirical AM1 calculation of the solvent effect on the fluorescence spectra of some dihydroquinolinones," *Spectrochimica Acta Part A: Molecular and Biomolecular Spectroscopy*, vol. 56, no. 8, pp. 1443–1452, 2000.
- [87] N. Man Fai and R. Zhang, "Dimensionality dependence of optical properties and quantum confinement effects of hydrogenated silicon nanostructures," *The Journal of Physical Chemistry B*, vol. 110, no. 43, pp. 21528–21535, 2006.
- [88] W. J. Qin, X. B. Yang, Y. W. Lu, J. Sun, S. A. Kulinich, and X. W. Du, "Silicon nanodisks via a chemical route," *Chemistry of Materials*, vol. 20, no. 12, pp. 3892–3896, 2008.
- [89] B. Delley and E. Steigmeier, "Size dependence of band gaps in silicon nanostructures," *Applied physics letters*, vol. 67, no. 16, pp. 2370–2372, 1995.
- [90] C. Yang and S. Li, "Size-dependent raman red shifts of semiconductor nanocrystals," *The Journal of Physical Chemistry B*, vol. 112, no. 45, pp. 14193–14197, 2008.
- [91] T. Shen, C. Koch, T. McCormick, R. Nemanich, J. Huang, J. Huang, *et al.*, "The structure and property characteristics of amorphous/nanocrystalline silicon produced by ball milling," *Journal of materials research*, vol. 10, no. 1, pp. 139–148, 1995.
- [92] L. W. Wang and A. Zunger, "Electronic structure pseudopotential calculations of large (apprx. 1000 atoms) Si quantum dots," *The Journal of Physical Chemistry*, vol. 98, no. 8, pp. 2158–2165, 1994.

- [93] L. S. Li, J. Hu, W. Yang, and A. P. Alivisatos, “Band gap variation of size- and shape-controlled colloidal CdSe quantum rods,” *Nano Letters*, vol. 1, no. 7, pp. 349–351, 2001.
- [94] L. F. Kourkoutis, X. Hao, S. Huang, B. Puthen-Veetil, G. Conibeer, M. A. Green, and I. Perez-Wurfl, “Three-dimensional imaging for precise structural control of Si quantum dot networks for all-Si solar cells,” *Nanoscale*, vol. 5, pp. 7499–7504, 2013.
- [95] C. Rao, R. Nagesa, P. J. Thomas, and G. Kulkarni, *Nanocrystals: synthesis, properties and applications*, vol. 95. Springer, 2007.
- [96] C. Suryanarayana, “Mechanical alloying and milling,” *Progress in materials science*, vol. 46, no. 1, pp. 1–184, 2001.
- [97] M. A. P. dos Santos and C. A. Costa, “Comminution of silicon carbide powder in a planetary mill,” *Powder technology*, vol. 169, no. 2, pp. 84–88, 2006.
- [98] H. Atkuri, G. Cook, D. Evans, C. Cheon, A. Glushchenko, V. Reshetnyak, Y. Reznikov, J. West, and K. Zhang, “Preparation of ferroelectric nanoparticles for their use in liquid crystalline colloids,” *Journal of Optics A: Pure and Applied Optics*, vol. 11, no. 2, pp. 1–6, 2009.
- [99] Y. Garbovskiy and A. Glushchenko, “Optical/ferroelectric characterization of $BaTiO_3$ and $PbTiO_3$ colloidal nanoparticles and their applications in hybrid materials technologies,” *Applied Optics*, vol. 52, no. 22, pp. E34–E39, 2013.
- [100] H. Shin, S. Lee, H. Suk Jung, and J.-B. Kim, “Effect of ball size and powder loading on the milling efficiency of a laboratory-scale wet ball mill,” *Ceramics International*, 2013.
- [101] P. Balaz, *Mechanochemistry in Nanoscience and Minerals Engineering*. Berlin, Heidelberg: Springer, 2008.
- [102] F. Zhang, Q. Jin, and S.-W. Chan, “Ceria nanoparticles: size, size distribution, and shape,” *Journal of applied physics*, vol. 95, no. 8, pp. 4319–4326, 2004.
- [103] H. G. Merkus, *Particle size measurements: fundamentals, practice, quality*, vol. 17. Springer, 2009.

- [104] M. S. Amer, *Raman spectroscopy, fullerenes and nanotechnology*. Royal Society of Chemistry, 2010.
- [105] Z. Iqbal and S. Vepřek, “Raman scattering from hydrogenated microcrystalline and amorphous silicon,” *Journal of Physics C: Solid State Physics*, vol. 15, no. 2, p. 377, 1982.
- [106] F. A. Sarott, Z. Iqbal, and S. Vepřek, “Effect of substrate bias on the properties of microcrystalline silicon films deposited in a glow discharge,” *Solid State Communications*, vol. 42, no. 6, pp. 465–468, 1982.
- [107] C. M. Hessel, J. Wei, D. Reid, H. Fujii, M. C. Downer, and B. A. Korgel, “Raman spectroscopy of oxide-embedded and ligand-stabilized silicon nanocrystals,” *The Journal of Physical Chemistry Letters*, vol. 3, no. 9, pp. 1089–1093, 2012.
- [108] A. Davies, “Raman spectroscopy (part 2): Equipment and methods [online],” Available: <http://www.see.ed.ac.uk/cbee/Raman2.html>. Accessed: March.10, 2014.
- [109] R. Gauvin, K. Robertson, P. Horny, A. M. Elwazri, and S. Yue, “Materials characterization using high-resolution scanning-electron microscopy and x-ray microanalysis,” *JOM*, vol. 58, no. 3, pp. 20–26, 2006.
- [110] Z. C. Holman and U. R. Kortshagen, “Solution-processed germanium nanocrystal thin films as materials for low-cost optical and electronic devices,” *Langmuir*, vol. 25, no. 19, pp. 11883–11889, 2009.
- [111] A. Akthakul, A. I. Hochbaum, F. Stellacci, and A. M. Mayes, “Size fractionation of metal nanoparticles by membrane filtration,” *Advanced Materials*, vol. 17, no. 5, pp. 532–535, 2005.
- [112] A. M. Hung, N. A. Konopliv, and J. N. Cha, “Solvent-based assembly of CdSe nanorods in solution,” *Langmuir*, vol. 27, no. 20, pp. 12322–12328, 2011.
- [113] L. M. Wheeler, N. R. Neale, T. Chen, and U. R. Kortshagen, “Hypervalent surface interactions for colloidal stability and doping of silicon nanocrystals,” *Nature communications*, vol. 4, 2013.

- [114] R. Lechner, A. R. Stegner, R. N. Pereira, R. Dietmueller, M. S. Brandt, A. Ebbers, M. Trocha, H. Wiggers, and M. Stutzmann, “Electronic properties of doped silicon nanocrystal films,” *Journal of Applied Physics*, vol. 104, no. 5, p. 053701, 2008.